

ER-5453

N64 13917

CODE-1

CR-55310



RESEARCH ON THE VORTEX MHD POWER GENERATOR

FINAL REPORT

NASA Contract NAS 3-2526

JULY 1963

TRW ELECTROMECHANICAL DIVISION
THOMPSON RAMO WOOLDRIDGE INC.

OTS PRICE

XEROX

MICROFILM

\$

\$

12.00 ph
5.15 mf.

ER-5453

FINAL REPORT

RESEARCH ON THE
VORTEX MHD POWER GENERATOR

Prepared for:
NATIONAL AERONAUTICS AND SPACE ADMINISTRATION

JULY 1963

CONTRACT NO. NAS3-2526

TECHNICAL MANAGER
NASA - LEWIS RESEARCH CENTER
SPACE ELECTRIC POWER OFFICE
HERMAN SCHWARTZ

New Product Research Department
TAPCO Division
Thompson Ramo Wooldridge Inc.
Cleveland, Ohio

NOTICE

This report was prepared as an account of Government sponsored work. Neither the United States, nor the National Aeronautics and Space Administration (NASA), nor any person acting on behalf of NASA:

- A.) Makes any warranty or representation, expressed or implied, with respect to the accuracy, completeness, or usefulness of the information contained in this report, or that the use of any information, apparatus, method, or process disclosed in this report may not infringe privately owned rights; or
- B.) Assumes any liabilities with respect to the use of, or for damages resulting from the use of any information, apparatus, method or process disclosed in this report.

As used above, "person acting on behalf of NASA" includes any employee or contractor of NASA, or employee of such contractor, to the extent that such employee or contractor of NASA, or employee of such contractor prepares, disseminates, or provides access to, any information pursuant to this employment or contract with NASA, or his employment with such contractor.

Requests for copies of this report
should be referred to:

National Aeronautics and Space Administration
Office of Scientific and Technical Information
Washington 25, D. C.
Attention: AFSS-A

FOREWORD

This report was prepared by TAPCO, a division of Thompson Ramo Wooldridge Inc., Cleveland, Ohio, in fulfillment of National Aeronautics and Space Administration Contract NAS3-2526, "Research on the Vortex MHD Power Generator". The work was administered under the direction of Mr. Walter Scott, Chief of the Advanced Technology Program, NASA Headquarters, Washington, D. C. Mr. Herman Schwartz, NASA Lewis Research Center, was the program monitor.

The studies presented began in April 1962, and were concluded in July 1963. The chief contributors and their fields of interest were:

- W. C. Davis: experimental and theoretical magnetohydrodynamics.
- W. F. Wade and E. L. Krasnoff: experimental and analytical study of vortex motion.
- A. F. Bond: computer analysis of vortex generator performance.
- R. J. Coerdts: reliability and materials performance; generator applications analysis.
- R. T. Craig: program management.

This report concludes the work on Contract NAS3-2526.

ABSTRACT

13917 *over*

Experimental and theoretical research on the vortex MHD power generator has been conducted to determine its area of feasible application and practical lower limits of power output. This effort is an extension of the research conducted previously under NASA Contract NAS5-703 wherein the various operating problems had been defined and the advantages of the vortex concept for MHD power generation established.

In the present study emphasis was given to advancing the concepts of turbulent vortex flows, to determining the operating characteristics of an experimental vortex MHD generator, and to improving the analytical methods for predicting generator performance.

The investigation of turbulent vortex flow was supported both analytically and experimentally. Analytical models, based on a pseudo-laminar analysis and in analogy with turbulent boundary layers, were developed for the hydrodynamics of turbulent jet-driven vortex flows with and without centerbodies. The mixing length theory which was developed under the earlier contract for this application was found to be more complicated and unnecessary. Measurements of the flow distributions within a vortex chamber generally confirmed the validity of the analytical models; they also revealed the presence of relatively strong radial flows in the sidewall boundary layers of the low aspect ratio vortex chamber employed.

A dual jet vortex type MHD generator was operated in the laboratory on cesium metal seeded arc-heated argon plasmas. Of the several test attempts, two were aborted because of commercial equipment failures and two were unsuccessful in producing substantial power because of rapid graphite exhaust tube erosion and subsequent generator shorting. The materials problem otherwise was reduced to an acceptable level. Heat transfer and thermal control were established consistent with original estimates.

A computer analysis for determining the performance of the vortex generator was developed. Real gas effects, including external heat transfer and viscous drag on the vortex sidewalls were thereby included in the calculation of overall generator performance.

13917

Finally, the computer analysis was applied to the example of a high temperature combustion plasma operated vortex MHD generator; the generator performance was shown to be very competitive with other types of strongly competing open-cycle power conversion systems.

A. Utkin

TABLE OF CONTENTS

	Page
FOREWORD	1
ABSTRACT	ii
TABLE OF CONTENTS	iv
TABLE OF NOMENCLATURE	v
1.0 INTRODUCTION	1
2.0 STUDY OF TURBULENT VORTEX MOTION	2
2.1 Analysis	2
2.2 Experiment	2
3.0 VORTEX GENERATOR OPERATION	46
3.1 Design of Experimental Generator	46
3.2 Test Facility and Instrumentation	53
3.3 Generating Operating Characteristics and Test Results	58
4.0 INVESTIGATION OF VORTEX GENERATOR SYSTEM RELIABILITY AND MATERIALS LIFETIME	76
4.1 Reliability	76
4.2 Materials Lifetime	80
5.0 GENERATOR MAGNET SYSTEMS	99
6.0 NUMERICAL SIMULATION OF THE VORTEX GENERATOR	109
6.1 Basic Equations and Assumptions	110
6.2 Computer Program	111
6.3 Example of Computed Generator Performance	117
7.0 VORTEX MHD GENERATOR APPLICATIONS AND COMPARISON WITH OTHER SYSTEMS	129
7.1 Applications	129
7.2 Comparison	133
8.0 CONCLUSIONS AND RECOMMENDATIONS	138
9.0 APPENDICES	140
10.0 REFERENCES	150

TABLE OF NOMENCLATURE

B	- magnetic flux density
c_f	- friction factor
C_f	- sidewall friction factor
c_p	- specific heat at constant pressure
c'_p	- specific heat (per unit volume) at constant pressure
c_v	- specific heat at constant volume
e	- electronic charge, base of natural logarithm
E	- eddy viscosity ($E = \rho \epsilon$), electric field gradient, modulus of elasticity
f	- function
F_r	- adjusted failure rate
g	- degeneracy
GF_r	- generic failure rate
ΔG	- free energy change
h	- enthalpy
h^o	- stagnation enthalpy
h	- heat transfer coefficient
k	- Planck's constant
I	- total current, ionization energy
j	- current density
k	- Boltzmann constant, nozzle flow coefficient
k	- thermal conductivity
k_D	- mass transfer coefficient
K	- mixing length parameter (Equation 16 of Section 2), generator load coefficient, equilibrium constant
\underline{K}	- mixing length parameter (Equation 19 of Section 2)

K_A	- reliability application factor
K_{op}	- reliability operating mode factor
l	- mixing length
l_e	- thickness of sidewall electrical insulator
l_t	- thickness of sidewall thermal insulator
L	- depth of vortex cavity
m	- mass loss rate per unit area
m_e	- electron mass
M	- Mach number
\mathcal{M}	- molecular weight
n	- number density
Nu	- Nusselt number
p	- pressure
p^o	- stagnation pressure
P	- electrical power, seed concentration
Pr	- Prandtl number
q	- heat transfer rate
Q	- collision cross section
r, θ, z	- cylindrical coordinate system directions
r	- radius
r_i	- inner radius of vortex cavity annulus
r_o	- outer radius at which the vortex flow is established
r_n	- effective radius to nozzle centerline
r_w	- outer radius of vortex cavity annulus
R	- universal gas constant, radius ratio = r/r_o
\underline{R}	- radius ratio = $(r - R_i)/(1 - R_i)$
R_i	- radius ratio = r/r_i

R_s	- reliability
Re	- Reynolds number
Re_{DN}	- nozzle throat Reynolds number
Re_u	- Reynolds number based on radius and radial velocity
Re_u^*	- Reynolds number based on radius, radial velocity, and eddy viscosity
Re_v	- Reynolds number based on radius and tangential velocity
t	- time
T	- temperature
T^0	- stagnation temperature
T_{aw}	- adiabatic wall temperature
T_{iw}	- wall inside surface temperature
u	- radial component of velocity
u_o	- radial component of velocity at r_o
U_o	- free stream speed
v	- tangential component of velocity
v_o	- recovered jet velocity at r_o
V	- tangential velocity ratio = v/v_o
w	- axial component of velocity
W	- mass flow rate
W_n	- nozzle height at exit
α	- coefficient of thermal expansion
γ	- ratio of specific heats
δ	- electron energy loss factor
ϵ	- degree of ionization, eddy diffusivity
θ	- angular coordinate

λ	- second coefficient of viscosity
μ	- first coefficient of viscosity
μ'	- bulk coefficient of viscosity
ν	- kinematic viscosity, Poisson's ratio
ρ	- mass density
σ	- electrical conductivity, stress
τ	- mean free collision time
ω	- electron cyclotron frequency, angular velocity
χ	- mole fraction
$\omega\tau$	- = $\omega\tau$

Subscripts:

g	- gas phase
s	- solid phase

1.0 INTRODUCTION

The area of light weight and reliable electric power production continues to attract great interest, particularly for space vehicle applications. Thus, the consideration of MHD systems in an effort to obtain improved-performance power conversion capability is quite natural.

A general examination of MHD power conversion and a search for attractive approaches and geometries was conducted by Thompson Ramo Wooldridge. From this search the concept of the vortex MHD power generator was evolved. The early investigation of this concept consisted of an initial phase of theoretical analyses and an experimental investigation of vortex generators utilizing liquid media. This investigation established that the vortex generator concept offered significant improvement in specific power over competitive linear channel MHD technology for several reasons: primary among these reasons are the more efficient utilization of the applied magnetic field and the lowered heat transfer, both of which naturally result from the specific vortex geometry.

The outstanding potential exhibited by the vortex MHD generator in the initial analysis justified that further theoretical and experimental work should be accomplished and NASA awarded TRW a contract (NAS5-703) to conduct this study. The results were a further confirmation of the basic feasibility of the vortex generator concept. The areas which could lead to major performance penalties or which could preclude the ultimate application of vortex MHD generators in the low kilowatt range were investigated. It was determined that none of these areas would contribute a major performance degradation. The degree to which the original theory is applicable was determined and improvements in the theoretical predictions were derived. Furthermore, the basic problem areas were defined and sufficient data accumulated so that it was possible to formulate the present program which logically would advance the vortex generator concept and define its applicability in the field of electric power generation. The results of that program, supported by a NASA contract effort, constitute this final report.

2.0 STUDY OF TURBULENT VORTEX MOTION

2.1 Analysis The objective of this study was to develop a simple analytical model for the hydrodynamics of turbulent jet driven vortex flows. The basic equations are written down in Appendix A and specialized to the case of axisymmetric flow. As an introduction to vortex flows involving an inner porous cylinder, Section 2.1.1 discusses the solution in the case of laminar flow. It is shown here that the controlling parameters consist of a tangential Reynolds number and the ratio of radial to tangential (driving jet) velocity. It is also shown that the inner cylinder friction coefficient has an asymptotic value which depends on the radial to tangential velocity ratio.

In Section 2.1.2, data for the case of four driving jets is analyzed on the basis of a constant eddy viscosity assumption. It is shown that a constant eddy viscosity is a characteristic of the flow in an "outer" region adjacent to the driving jets. In this outer region, it is also shown that the ratio of eddy to molecular viscosity has the form

$$\frac{E}{\mu} = \frac{K^2}{2} Re_v$$

where Re_v is a tangential Reynolds number and K is a function of the radial to tangential velocity ratio. The consequence of this is that tangential velocity profiles in the outer region depend only on this velocity ratio. In particular, it is finally shown that the inner wall friction coefficient depends only on this velocity ratio.

The solution of Section 2.1.2 is discussed in Section 2.1.3 in terms of mixing length concepts. Here it is shown that K is the universal constant of mixing length theory multiplied by a function of the radial to tangential velocity ratio. In Section 2.1.4 the regions adjacent to the inner porous cylinder are discussed. An expression for the profile in a "sublayer" is obtained by neglecting the eddy viscosity in comparison to the molecular viscosity and enforcing the known inner wall friction coefficient. The "transition" region (adjacent to the sublayer) and the "wall" region (adjacent to the outer region) on the other hand, require additional data for useful analyses and correlations.

Finally, the flow equations for a vortex without a porous inner cylinder are discussed in Section 2.1.5. These equations are included primarily because they pertain to the conditions of flow in the experimental vortex chamber and also since they may find application in a generator configuration having no centerbody.

2.1.1 Laminar Vortex Flow with Porous Inner Cylinder As an introduction to jet driven vortex flows with an inner cylinder on which the tangential velocity vanishes, consider the case of laminar flow. It is shown in Appendix A that

$$\frac{dp}{dr} = \rho \frac{(u^2 + v^2)}{r} \quad (1)$$

$$ur = u_0 r_0 \quad (2)$$

$$v = Ar^{-1} + Br^{1 + Re_u} \quad (3)$$

where

(u, v) = velocity components in the (r, θ) - cylindrical coordinate system

p = pressure

ρ = density

$Re_u = u_0 r_0 / \nu$, the (negative) radial Reynolds number

ν = kinematic viscosity

v_0 = recovered driving jet velocity which obtains at $r = r_0$

The recovered jet velocity v_0 can be obtained in view of the known driving jet momentum and a torque balance in the manner of Reference 1. It will be assumed here that v_0 is known. Introducing dimensionless variables

$$V = \frac{v}{v_0}, \quad R = \frac{r}{r_0} \quad (4)$$

the "tangential" velocity is

$$V = \frac{R^{-1} - R_1^{-(2 + Re_u)} R^{(1 + Re_u)}}{1 - R_1^{-(2 + Re_u)}} \quad (5)$$

where the constants A and B have been evaluated so that $V = 1$ at $R = 1$ and $V = 0$ at $R = R_1$, the inner cylinder radius. This velocity profile peaks at

$$R_m = R_i \left[-(1 + Re_u) \right]^{\frac{-1}{2 + Re_u}}$$

For $-Re_u \gg 1$ it is seen that $R_m \approx R_i$. (Note that for $Re_u = -10$, $R_m = 1.316 R_i$; for $Re_u = -100$, $R_m = 1.045 R_i$). The laminar profiles are, therefore, characterized by very large velocity gradients near the inner cylinder which are similar to laminar suction boundary layers. The inner cylinder friction coefficient is

$$c_{f_i} = \frac{\tau_i}{\frac{1}{2} \rho v_o^2} = \frac{2}{Re_v} \left(\frac{dv}{dR} \right)_{R=R_i}$$

or

$$c_{f_i} = \frac{2}{Re_v} \frac{-(2 + Re_u)}{\left[1 - R_i^{-(2 + Re_u)} \right] R_i^2} \quad (6)$$

where $Re_v = \frac{v_o r_o}{\nu}$

For $-Re_u \gg 1$ the asymptotic expression

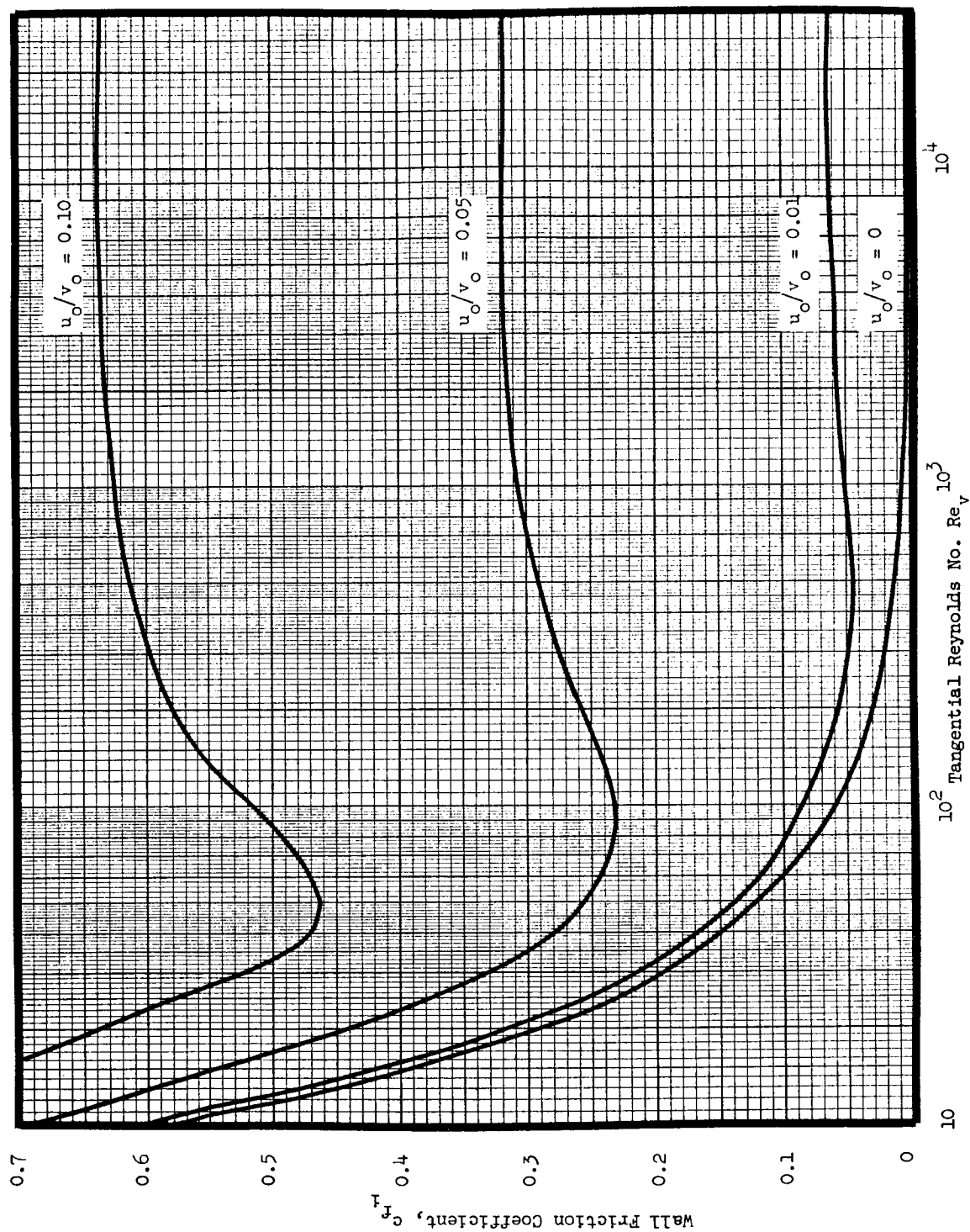
$$c_{f_i} \sim - \frac{Re_u}{R_i^2 Re_v} = - \frac{2}{R_i^2} (u_o/v_o) \quad (7)$$

is applicable. This friction coefficient may be compared to the asymptotic value for a flat plate boundary layer with uniform suction. It is

$$c_{f_{b.l.}} \sim - 2 u_o/U_o$$

where u_o is the wall suction speed and U_o the free stream speed.

A plot of Equation (6) is presented in Figure 2-1 where the effect of the radial to tangential velocity ratio is shown. (The value $R_i = 0.56$ was chosen in generating Figure 2-1. It corresponds to the tests discussed in Reference 2.) The interesting result is that, for velocity ratios of interest $u_o/v_o > 0.01$, the wall friction coefficient is essentially constant for Re_v greater than about 10^3 . Assuming that turbulent flows obtain for $Re_v > 10^3$ this suggests that the turbulent friction coefficients depend only on u_o/v_o . One might also expect the turbulent friction coefficients to be less than the laminar friction coefficients. Consider the dimensionless torque balance relation



Effect of Velocity Ratio, u_o/v_o , on Inner Wall Friction Coefficient, c_{f_i} Figure 2-1

$$R_1^2 c_{f_1} = R^2 c_f - 2(u_o/v_o) RV \quad (8)$$

where

$$c_f = \frac{2}{Re_v} \left(\frac{dV}{dR} - \frac{V}{R} \right) \quad (9)$$

Applying (8) at $R = 1$ where $V = 1$ for either laminar or turbulent flow shows that c_{f_1} will be smaller for turbulent flow than for laminar flow if the opposite is true of $|c_f|$, the shear at $R = 1$. That this is the case is shown in the next section.

2.1.2 Turbulent Vortex Flow with Porous Inner Cylinder The only published tangential velocity data which cover a range of Re_v and u_o/v_o wide enough to permit correlations between theory and experiment are presented in Reference 2. This has been done for the case of four driving jets. The basis of initial analyses of the data was chosen to be a constant eddy viscosity model on the premise that this is a good assumption for the free turbulence region of a vortex chamber. It was expected that the portion of a vortex chamber between the driving jets ($R = 1$) and some radius smaller than the radius at which the maximum velocity occurs would be a constant eddy viscosity region. Accordingly, the basic equation governing the mean tangential flow was taken as (see Appendix A)

$$\frac{Re_u^*}{(1 + \frac{\mu}{E}) R} \left(\frac{dV}{dR} + \frac{V}{R} \right) = \frac{d}{dR} \left(\frac{dV}{dR} + \frac{V}{R} \right) \quad (10)$$

where the effective radial Reynolds number is

$$Re_u^* = \frac{\rho u_o r_o}{E} \quad (10A)$$

and E is the eddy viscosity. The dimensionless tangential velocity V is now the ratio of the mean turbulent value, \bar{v} , to the recovered jet velocity, v_o . Neglecting μ/E as being small compared to one, the solution of (10) which gives $V = 1$ at $R = 1$ is

$$V = CR^{-1} + (1 - C) R^{1 + Re_u^*} \quad (11)$$

This equation was originally used in a form which displayed a velocity V_1 , the extrapolated wall or inner cylinder velocity at $R = R_1$. Introduction of this notion was made in analogy to the work of Reference 3 where the outer region of turbulent boundary layers was studied. Its introduction into (11) merely serves to emphasize that (11) should be valid only in the outer region of a vortex chamber. In terms of R_1 and V_1 , (11) becomes

$$V = \left[1 - R_1^{-(2 + Re_u^*)} \right]^{-1} \left\{ \left[1 - V_1 R_1^{-(1 + Re_u^*)} \right] R^{-1} - (1 - R_1 V_1) R_1^{-(2 + Re_u^*)} R^{1 + Re_u^*} \right\} \quad (12)$$

This expression was matched to the experimental velocity profiles of Reference 2 by requiring that it produce the experimental maximum velocity. That is, $V = V_{\max}$ and $dV/dR = 0$ at $R = R_{\max}$ were used to define two equations for V_1 and Re_u^* . The resulting values of Re_u^* and V_1 were then analyzed and the inner wall friction coefficient was calculated from a torque balance between the inner and outer cylinders. This torque balance requires that

$$R_1^2 c_{f_1} = c_{f_0} - 2(u_o/v_o) \quad (13)$$

where the turbulent outer friction coefficient is

$$c_{f_0} = \frac{2(E/\mu)}{Re_v} \left(\frac{dV}{dR} - \frac{V}{R} \right)_{R=1} \quad (14)$$

Recalling that

$$Re_u^* = \frac{Re_v (u_o/v_o)}{(E/\mu)}$$

or

$$\frac{E}{\mu} = \frac{Re_v (u_o/v_o)}{Re_u^*} \quad (15)$$

shows that the eddy viscosity is known once the effective radial Reynolds number is known. Furthermore, it has been shown in References (4) and (5) that

$$\frac{E}{\mu} = \frac{K^2}{2} Re_v \quad (16)$$

The meaning of this relation is discussed in Section 2.1.3. For the moment, it may be considered an assumption (keeping in mind that K depends on u_o/v_o). Then there is obtained

$$Re_u^* = \frac{2(u_o/v_o)}{K^2} \quad (17)$$

and

$$c_{f_o} = K^2 \left(\frac{dv}{dR} - \frac{v}{R} \right)_{R=1} \quad (18)$$

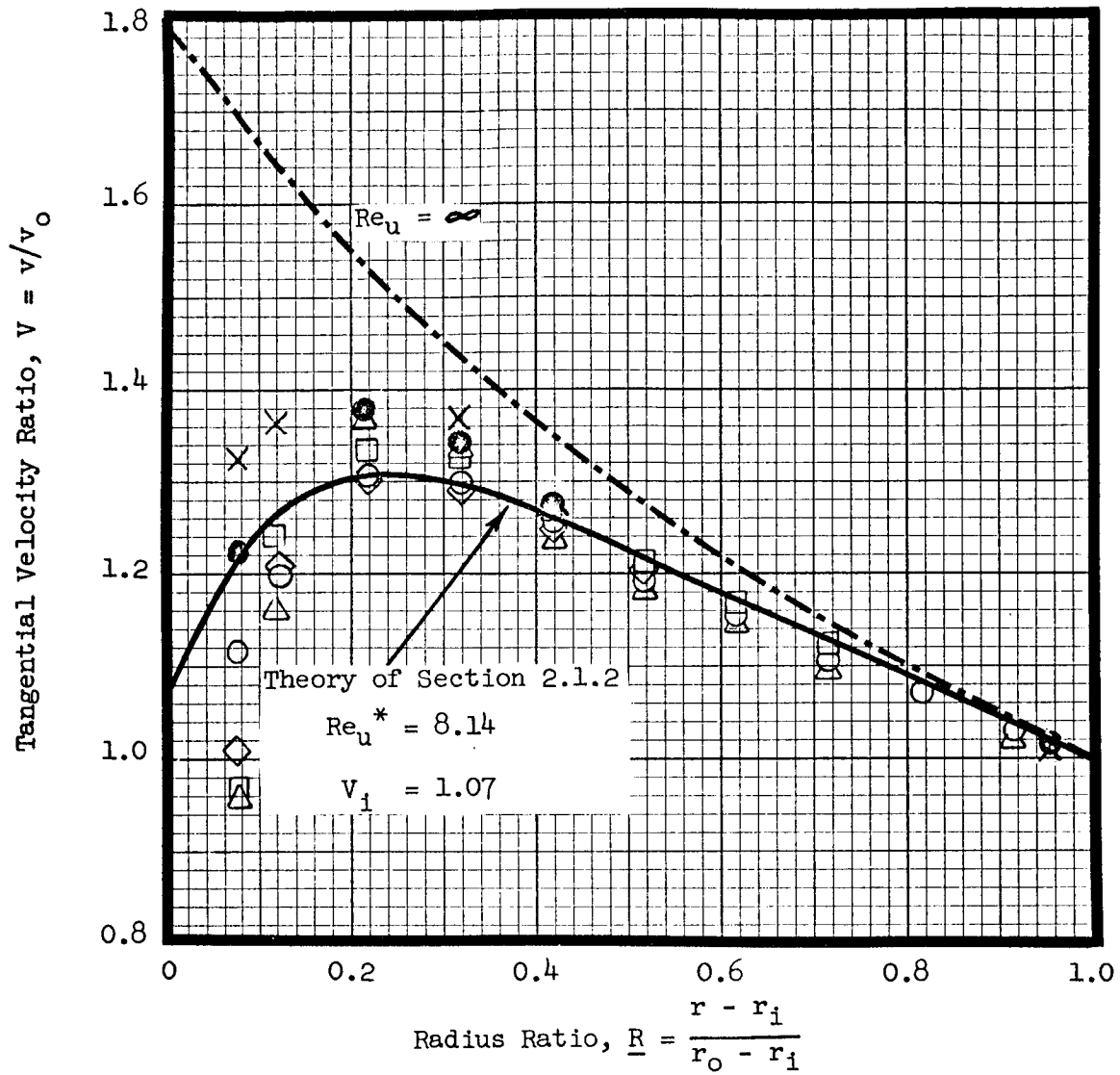
Thus, the outer region of the turbulent velocity profile is seen to be independent of Re_v and, therefore, so is the inner cylinder friction coefficient.

Results of the analysis of the data of Reference 2 according to the procedure outline above are presented in Figures 2-2 through 2-6. It is seen that the constant eddy viscosity model can indeed be employed to represent the outer region of a turbulent vortex chamber flow. The tangential velocity profiles are plotted versus the normalized radius

$$\underline{R} = \frac{R - R_1}{1 - R_1}$$

and it appears that the outer region where E is constant extends in to about $\underline{R} = 0.15$. (This corresponds to about 0.2 inches from the inner cylinder of the vortex chamber of Reference 2). The region $0 < \underline{R} < 0.15$ will be referred to as the inner or wall region as it has the character of the wall region of a turbulent boundary layer. This region is discussed in Section 2.1.4.

The scatter in the variation of the "constant" K with u_o/v_o is associated with the scatter in the data of Reference 2. It is, in particular, caused by the scatter in the estimated value and location of the maximum tangential velocity point. The data available do not really permit a good specification of this point. The reduced scatter in the c_{f_1} , u_o/v_o - curve stems from the insensitivity of c_{f_1} to the effective Reynolds number, Re_u^* , and note that the term



Radial Reynolds Number
Data of Ref. 2 ($u_0/v_0 = -.0575$)

	Re_u	L/r_w
○	-10,300	.29
□	- 8,700	.29
●	- 6,900	.56
△	- 5,800	.29
×	- 3,300	.56
◇	- 3,100	.29

Tangential Velocity Profiles

Figure 2-2

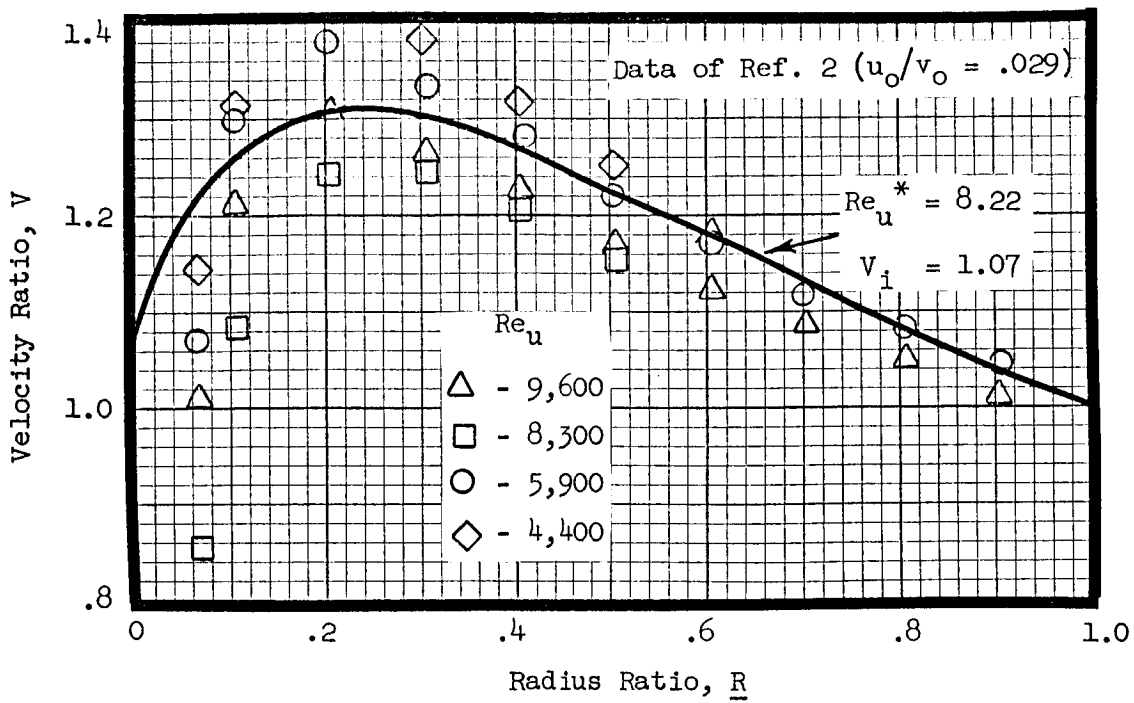


Figure 2-3

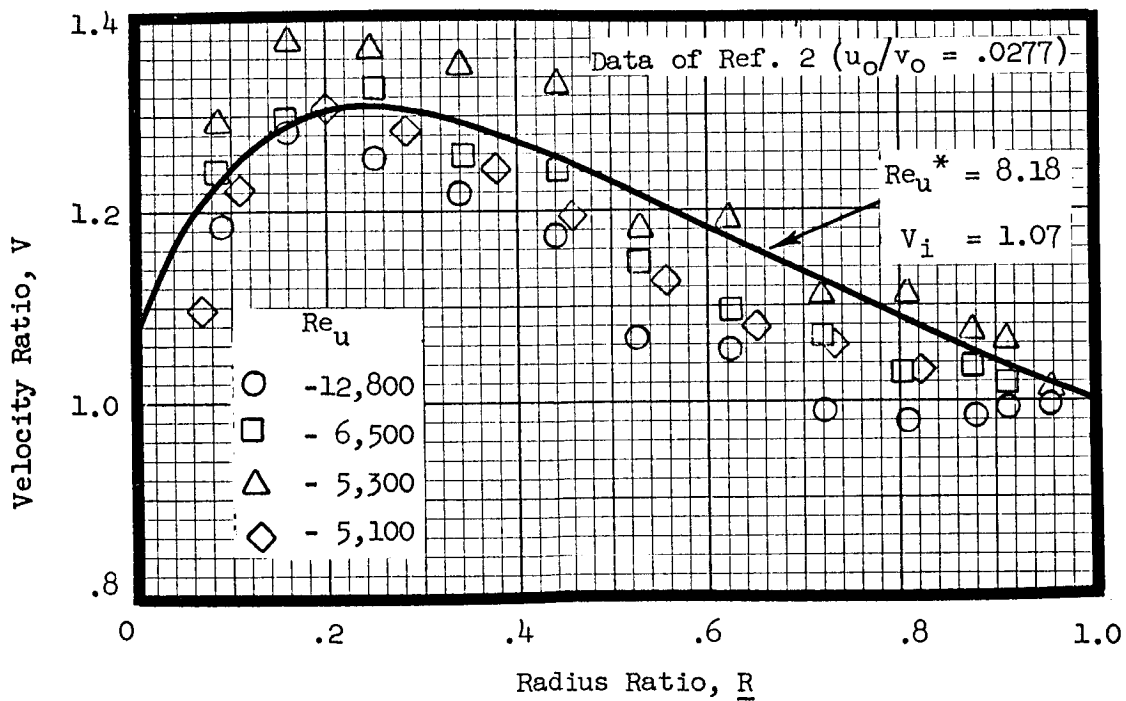
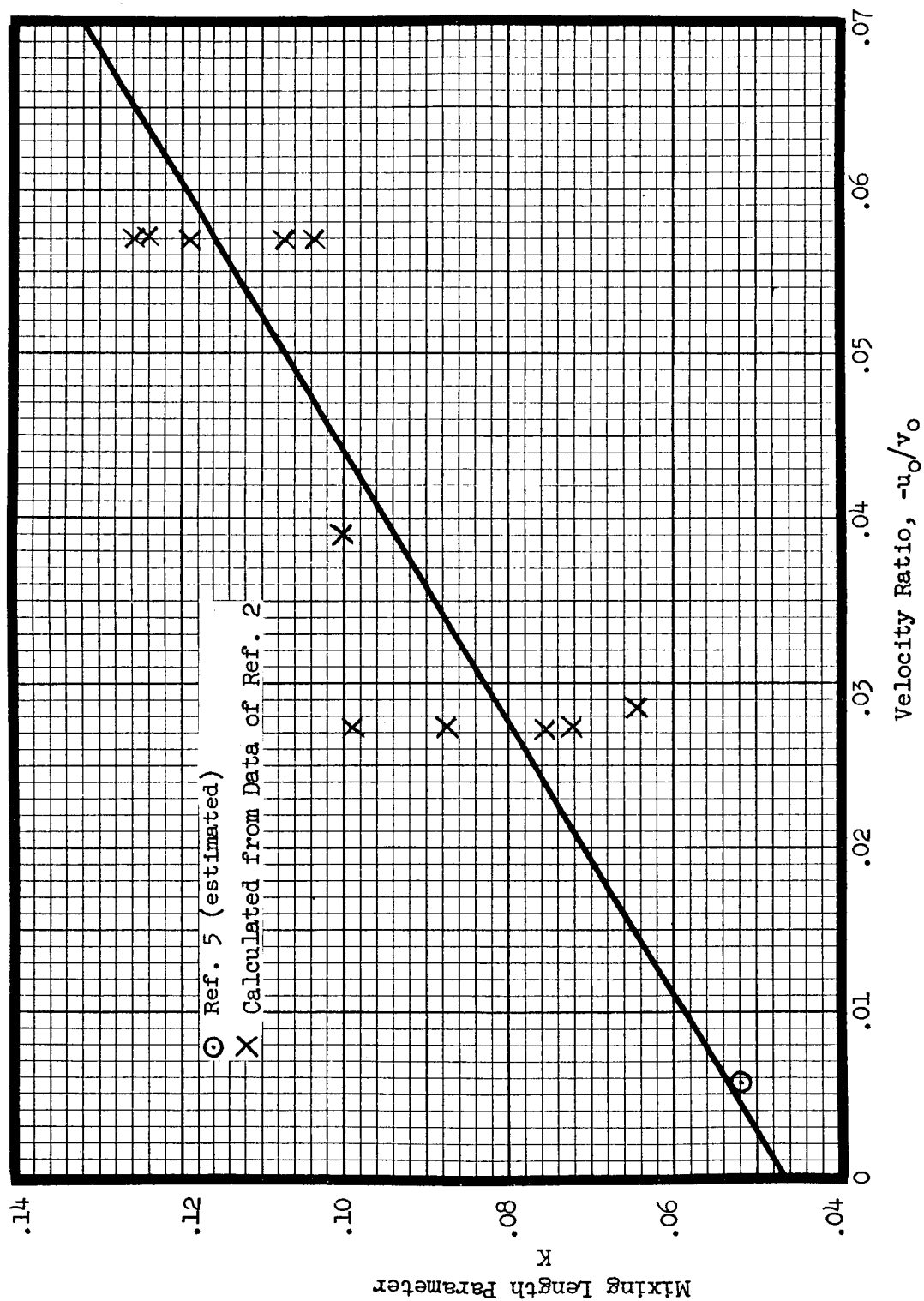
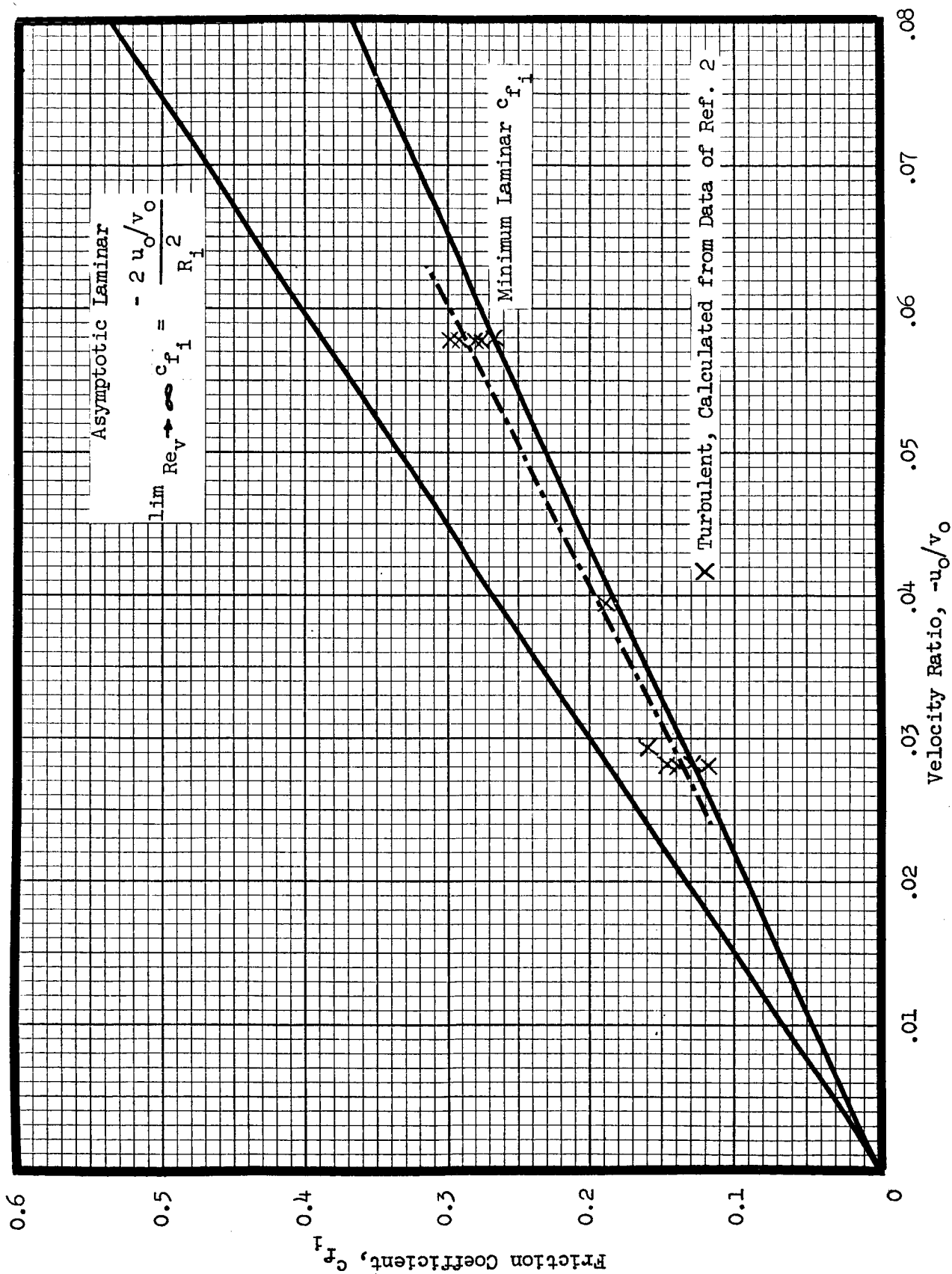


Figure 2-4

Tangential Velocity Profiles



Variation of Mixing Length Parameter with Radial-Tangential Velocity Ratio Figure 2-5



Comparison of Laminar and Turbulent Wall Friction Coefficients Figure 2-6

involving the outer friction coefficient, c_{f0} , is dominated by the term involving the jet momentum, $2 u_0/v_0$ in (13). The value of V_1 of 1.07 used in Figures 2-2, 2-3, 2-4 is the average value of all obtained. No trend to V_1 was observed since it is extremely sensitive to the choice of the maximum velocity point.

2.1.3 Mixing Length Considerations Mixing length concepts have been employed to explain turbulent vortex characteristics in the literature, notably References 2 and 4. Some of the comments in these references may lead to confusion, and it is the purpose of the following section to clarify two particular points.

First consider the remarks in Reference 2 which suggest that the mixing length, ℓ , is independent of u_0/v_0 . According to von Karman's similarity hypothesis the mixing length is

$$\ell = \frac{-K \left(\frac{d\bar{v}}{dr} - \frac{\bar{v}}{r} \right)}{\frac{d}{dr} \left(\frac{d\bar{v}}{dr} - \frac{\bar{v}}{r} \right)}$$

or, in the dimensionless variables \underline{R} , V ,

$$\frac{\ell}{r_0} = \frac{-K (1 - R_1) \left(\frac{dV}{dR} - \frac{V}{A + R} \right)}{\frac{d}{dR} \left(\frac{dV}{dR} - \frac{V}{A + R} \right)} \quad (19)$$

where $A = \frac{R_1}{1 - R_1}$

We have already seen that, in the outer region, $V = V(\underline{R}, R_1, u_0/v_0)$ and \underline{K} , which is related to K of Section 2.1.2, also depends on u_0/v_0 . It may also be noted now that the analytical calculations of tangential velocity profiles carried out in Reference 2 were based on (19) and mixing length variations calculated from experimental tangential velocity profiles. There resulted the necessity for numerically integrating the basic differential equation. This numerical integration is not necessary when the problem is formulated in terms of the eddy viscosity, E , as in the previous section of this report. In Section 2.1.4, it will be shown that the wall region of a vortex chamber can also be specified in closed form.

In Reference 4, the relation [See (16)]

$$\frac{E}{\mu} = \frac{K^2}{2} Re_v$$

was introduced and K was referred to as the universal constant of mixing length theory. While it was suggested that K was not a universal constant at all but depended on the geometry of the flow, we can now show specifically what this dependence is. We have

$$E = \rho l^2 \left(\frac{d\bar{v}}{dr} - \frac{\bar{v}}{r} \right)$$

$$\frac{E}{\mu} = \frac{Re_v \left(\frac{l}{r_o} \right)^2}{1 - R_1} \left(\frac{dV}{dR} - \frac{V}{R + A} \right) \quad (20)$$

Using (19) in (20) there is obtained

$$\frac{E}{\mu} = \left\{ 2(1 - R_1) \frac{\left(\frac{dV}{dR} - \frac{V}{R + A} \right)^3}{\left[\frac{d}{dR} \left(\frac{dV}{dR} - \frac{V}{A + R} \right) \right]^2} \right\} \frac{K^2}{2} Re_v \quad (21)$$

By comparing (21) with (16), it is seen that the relation between \underline{K} of mixing length theory and K is

$$K = \underline{K} \left\{ \frac{2(1 - R_1) \left(\frac{dV}{dR} - \frac{V}{A + R} \right)^3}{\left[\frac{d}{dR} \left(\frac{dV}{dR} - \frac{V}{A + R} \right) \right]^2} \right\}^{1/2} \quad (22)$$

In using (21) to evaluate E/μ , the calculation of Reference 4 evaluated the term in the bracket of (21) and (22) at $R = 1$. But in addition, the calculation was made under the assumption that $-Re_u^* \rightarrow \infty$. In this case only it turns out that the bracketed term is one and $K = \underline{K}$. The specific dependence of the mixing length parameter K on both R_1 and u_o/v_o was thus masked in Reference 4.

In concluding this section, it is noted that constant eddy viscosity in the outer region implies a mixing length which increases with \underline{R} . This can be shown most simply by assuming $Re_u^* \rightarrow \infty$. Then it is found that

$$\frac{\mathcal{L}}{r_o} = \frac{K}{2} (1 - R_i) (A + \underline{R}) = \frac{K}{2} \underline{R}$$

for the outer region. This is in qualitative agreement with the results of Reference 2 for the case of four driving jets.

2.1.4 The Inner Regions of a Turbulent Vortex with Porous Inner Cylinder

In the region between the inner cylinder and the outer region of a vortex chamber, the equation for the tangential velocity is

$$\frac{d}{d\underline{R}} \left[\frac{dV}{d\underline{R}} + \frac{V}{A + \underline{R}} \right] = \frac{Re_v}{(1 + E/\mu)(A + \underline{R})} \left(\frac{dV}{d\underline{R}} + \frac{V}{A + \underline{R}} \right) - \frac{1}{1 + E/\mu} \frac{d(E/\mu)}{d\underline{R}} \left(\frac{dV}{d\underline{R}} - \frac{V}{A + \underline{R}} \right) \quad (23)$$

where E/μ is now a function of \underline{R} . Equation (23) follows from Equations (16) and (16A) of Appendix A for $E = E(\underline{R})$. The reader can also verify that it results from differentiating the torque balance relation

$$(1 + E/\mu)(A + \underline{R})^2 \left(\frac{dV}{d\underline{R}} - \frac{V}{A + \underline{R}} \right) - Re_u(A + \underline{R})V = \text{constant} \quad (24)$$

This torque balance relation can be used, in view of experimental tangential velocity profiles, to determine the function $E = E(\underline{R})$. An analogous task was performed in Reference 2 where, however, the mixing length was introduced into (24) (see Section 2.1.3). It is now suggested that mixing length concepts be avoided and (24) used to analyze experimental results. If this is done, it can be hoped that, in the region adjacent to the outer region of the vortex, the eddy viscosity has the form (see Section 2.1.2)

$$\frac{E}{\mu} = f(\underline{R}) \frac{K^2}{2} Re_v \quad (25)$$

where $f(\underline{R})$ is a universal function. The region referred to is analogous to the wall region of a turbulent boundary layer; and the conjecture, Equation (25), is made in view of the universality of the wall region of a turbulent boundary layer.

In the "sublayer" immediately adjacent to the inner cylinder of a vortex chamber the eddy viscosity may be neglected as being small compared to the molecular viscosity. Then, so long as $d(E/\mu)/d\underline{R}$ is also small (a questionable assumption) the basic equation (23) reduces to

$$\underline{\underline{d}} \left(\underline{\underline{dV}} + \frac{V}{A + \underline{R}} \right) = \frac{Re_u}{A + \underline{R}} \left(\underline{\underline{dV}} + \frac{V}{A + \underline{R}} \right) \quad (26)$$

The general solution is

$$V_s = \frac{C_s}{2 + Re_u} (A + \underline{R})^{1 + Re_u} + \frac{B_s}{A + \underline{R}}$$

Applying the boundary condition that $V_s = 0$ at $\underline{R} = 0$ results in

$$V_s = \frac{C_s}{2 + Re_u} \left\{ (A + \underline{R})^{1 + Re_u} - \frac{A^{2 + Re_u}}{A + \underline{R}} \right\}$$

Now the constant C_s is obtained by introducing next the inner wall friction coefficient which is known (Section 2.1.2). We have

$$c_{f_1} = \frac{2}{Re_v} \left. \frac{dV}{d\underline{R}} \right|_{R=R_1} = \frac{2}{(1 - R_1)Re_v} \left. \frac{dV}{d\underline{R}} \right|_{\underline{R}=0}$$

or

$$V'(0) = (1/2)(1 - R_1) Re_v c_{f_1}$$

Using this, the result for the sublayer profile is found to be

$$V_s = \frac{(1/2)(1 - R_1) Re_v c_{f_1}}{A^{Re_u} (2 + Re_u)} \left\{ (A + \underline{R})^{1 + Re_u} - \frac{A^{2 + Re_u}}{A + \underline{R}} \right\} \quad (27)$$

This holds only for $\underline{R} \ll 1$ and permits the approximation

$$v_s = (1/2)(1 - R_1) Re_v c_{f_1} \underline{R} \quad (28)$$

Recalling that c_{f_1} depends on u_o/v_o , Equation (28) clearly shows also the dependence of the sublayer profile on Re_v . Consider now the assumption that the second term on the right of (23) is small compared to the first; Equation (28) renders this assumption equivalent to

$$\frac{-Re_u}{A} \ll \frac{d(E/\mu)}{d\underline{R}}$$

Using (25) results in

$$\frac{df}{d\underline{R}} < < - \frac{2(u_o/v_o)}{AK^2} \quad (29)$$

Noting that f must be zero at the wall and unity at the beginning of the outer region ($\underline{R} \approx 0.15$) shows that the inequality (29) is not satisfied by the data of Section 2.1.2. As an example consider $u_o/v_o = -0.0575$ for which $K \approx 0.12$ and $A \approx 1.27$. According to (29) then

$$\frac{df}{d\underline{R}} < < 6$$

while, since $f = 1$ at $\underline{R} \approx 0.15$, we must have $df/d\underline{R} = 0(1/0.15) = 0(6.7)$.

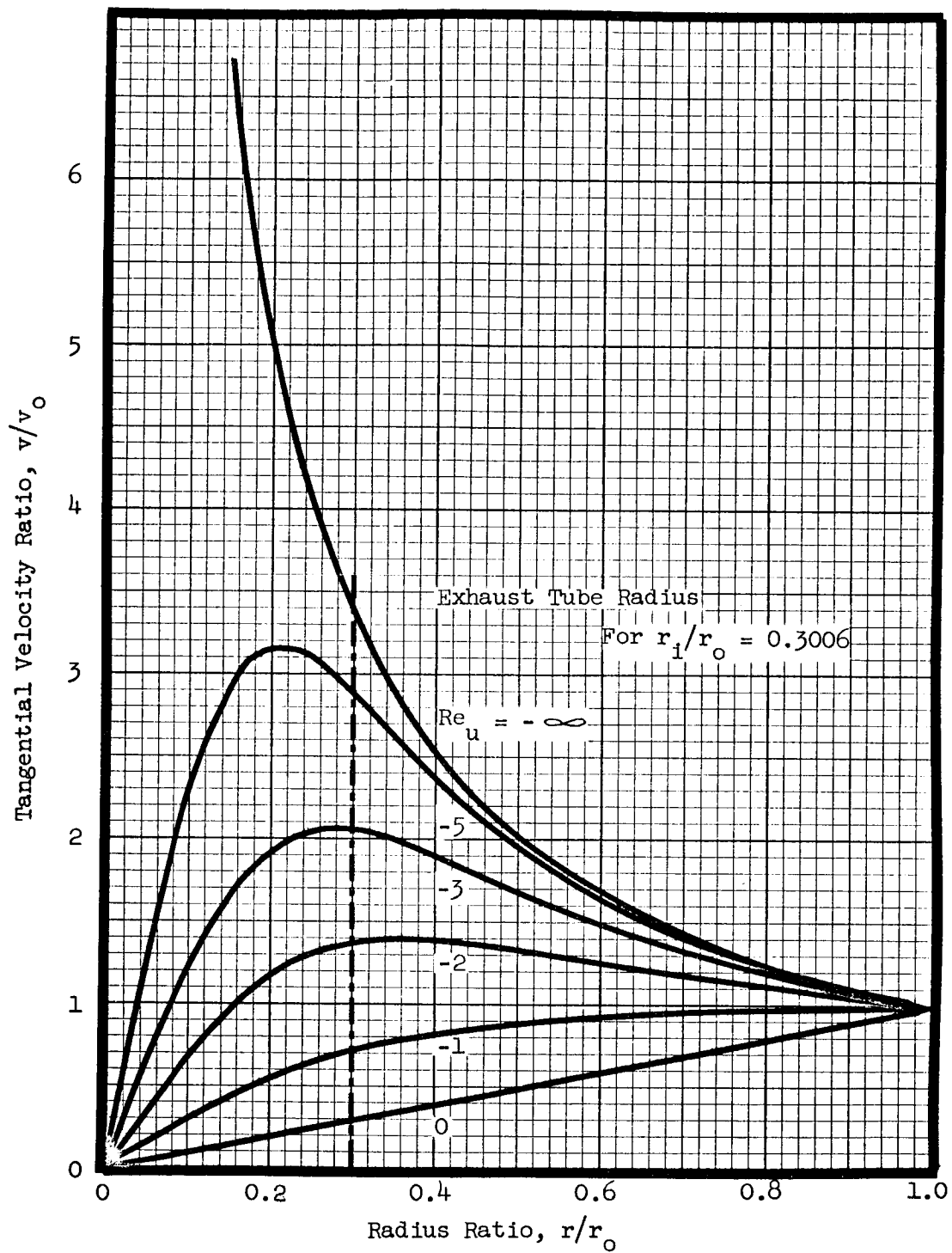
In Reference 6, the second term on the right of (23) was neglected in order to obtain an idea of the velocity profiles in the wall region. Linear variations were assumed for E/μ and the equation was integrated. The results ultimately displayed a velocity gradient discontinuity where the wall region profile intersected the sublayer profile as given by (28). This is consistent with the results of the previous paragraph and suggests that future analyses must be based on (23) in its complete form or on (24). In Appendix B, (24) is integrated and an example of a resulting profile is given.

2.1.5 Flow in a Vortex without Porous Inner Cylinder (Centerbody) The equations of flow in a vortex not containing a centerbody were derived primarily as a means of analyzing the experimental results obtained from the vortex chamber flow measurements. The solution for the tangential velocity is indicated by Equation (10) and (11) of Appendix C and illustrated in Figure 2-7 for the geometric ratio $r_i/r_o = 0.3$ of the experimental device. The tangential momentum equations, as noted in Appendix C, are identical for both compressible and incompressible flows. However, compressibility effects cannot be ignored in the method of determining velocity distributions from radial static pressure distributions. This aspect will be discussed later.

2.2 Experiment The experimental program undertaken in support of the turbulent vortex flow analysis consists of several parts. First, a flow visualization study, described in Section 2.2.1, was performed as a means of improving our physical intuition of the vortex flow processes. Subsequently, more elaborate measurements were conducted in a vortex chamber (Section 2.2.2) wherein tangential velocity distributions were determined. Finally the extent of boundary layer formation on the vortex chamber sidewalls was explored because of the possibility, suggested by the work of Kendall that these boundary layers would have a very significant influence on the performance of low aspect ratio (L/r_o) vortex chambers.

2.2.1 Flow Visualization Study In order to improve our physical intuition of vortex flow processes, and in an effort to explain seeming inconsistencies in the data of Reference 2, a flow visualization study of an incompressible vortex was made. The flow of water in a single-nozzle vortex chamber with centerbody was studied by means of flexible tufts, and by ink injection.

The dimensions of the vortex chamber, which was designed and used for an earlier study, were as follows: outside radius, $r_w = 2$ inches; centerbody radius $r_i = 0.5, 1, \text{ or } 1.5$ inches; centerbody shape, tubular with five 0.030 inch wide circumferential slots; depth, $L = 0.375$ inch; nozzle width = 0.125 inch; nozzle depth = 0.375 inch; nozzle location, outer surface tangent to outer wall of vortex, $r_n = 1.937$ inches. Thus, the pertinent dimensionless geometrical ratios were:



Tangential Velocity Distribution
in a Vortex Chamber without Centerbody Figure 2-7

$$\frac{L}{r_w} = 0.1874$$

$$\frac{r_i}{r_w} = 0.25, 0.5, 0.75$$

$$\frac{r_n}{r_w} = 0.969$$

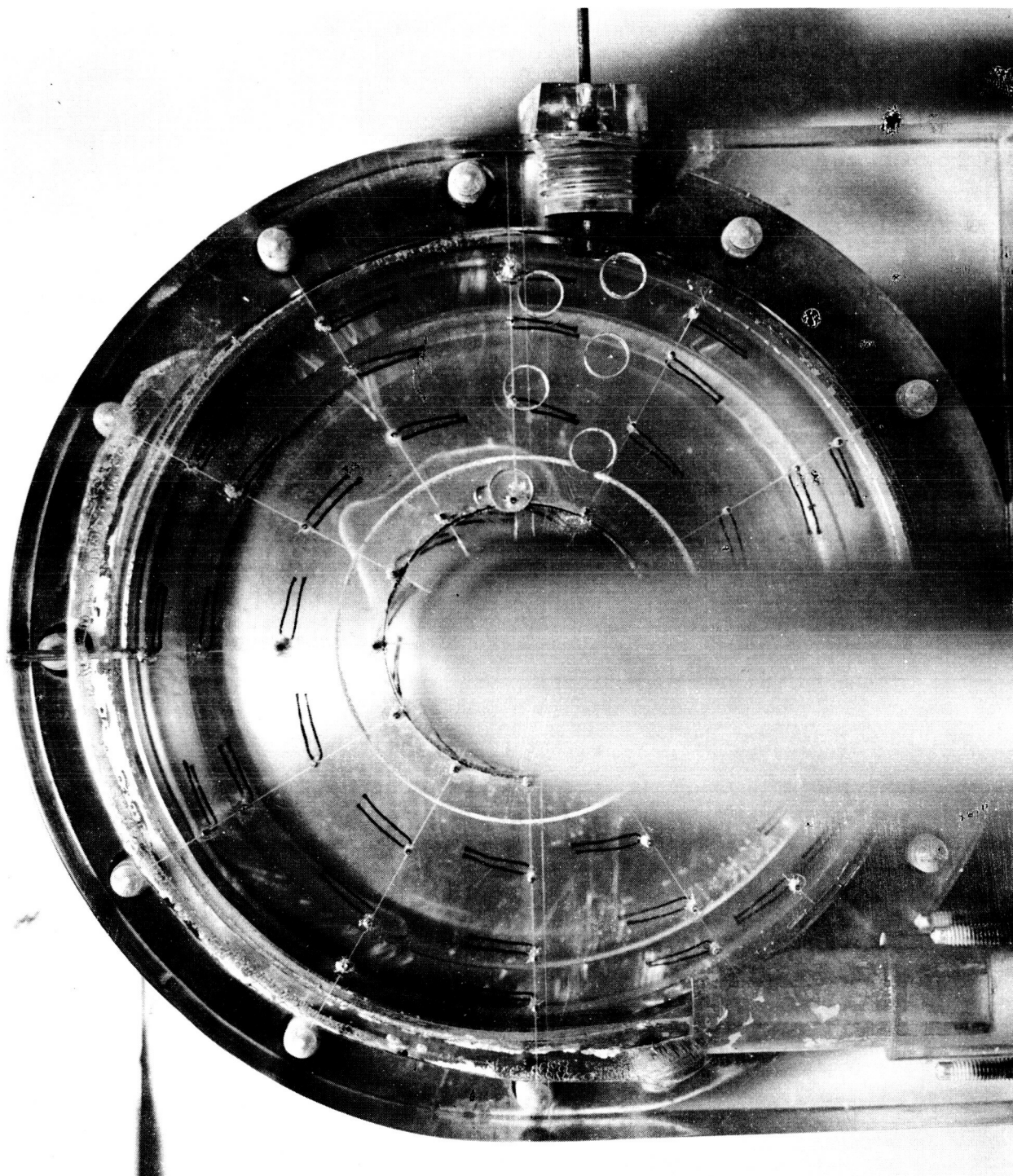
$$\frac{u_o}{v_o} \approx \frac{W_n}{2\pi r_w} = 0.00995$$

For the flow visualization study, the vortex chamber was equipped with fifty needles, each holding a tuft of black thread. All tufts were positioned in the midplane of the chamber.

Photographs of the tufts were taken for each of the three geometries at two turbulent radial Reynolds numbers: $Re_u = u_o r_o / \nu_o \approx -400$ and -3000 . A typical picture is shown in Figure 2-8. In addition, several pictures were taken at near-laminar Reynolds number, estimated to be $Re_u \approx -50$, with ink injection through the outer wall. The pictures were analyzed by measuring the angles assumed by the tufts, and by estimating the mean-flow streamline shapes.

At a given Reynolds number, the effect of the centerbodies was small; the tufts in the three pictures at either turbulent Reynolds number show identical flow directions. This is true of tufts both upstream and downstream of the centerbodies; these centerbodies certainly do not stagnate the tangential flow. There was some difference between the two turbulent flows for a given geometry; the flow at the lower Reynolds number was more radial, thus, the velocity recovery was poorer. All flows showed some azimuthal dependence, which extended all the way in to the centerbody; this azimuthal dependence was strongest near the nozzle, as expected.

The estimated mean flow streamlines show that a given "mean flow particle" will make two to three complete revolutions before reaching the one-inch centerbody, for the low Reynolds number case. At the high Reynolds number, at least one more revolution will result because of the higher tangential velocity recovery.



TUFT STUDY PHOTOGRAPH; FLOW IN AN INCOMPRESSIBLE VORTEX

The near-laminar Reynolds number pictures show clearly that the slip plane between a laminar jet and a laminar vortex is unstable; this region immediately rolls up to form relatively small vortices which decay as the jet decelerates to the main vortex flow velocity. The disturbances which lead to the small vortices probably came from the needles which supported the tufts.

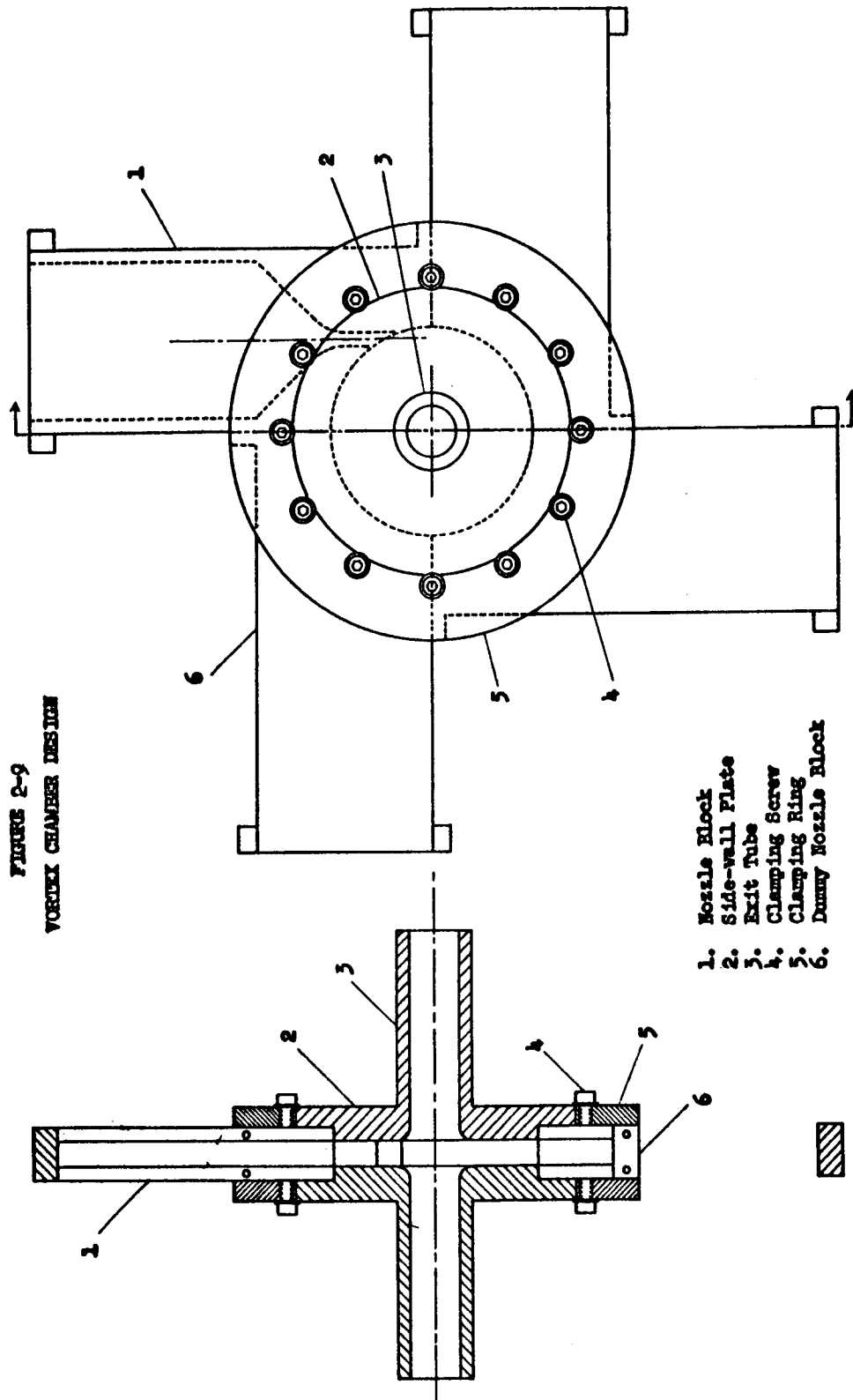
2.2.2 Vortex Chamber Design At the conclusion of the hydrodynamic studies conducted under the preceeding NAS5-703 contract, definite recommendations, Reference 2, were made for the improvement of the existing experimental apparatus. These recommendations were to:

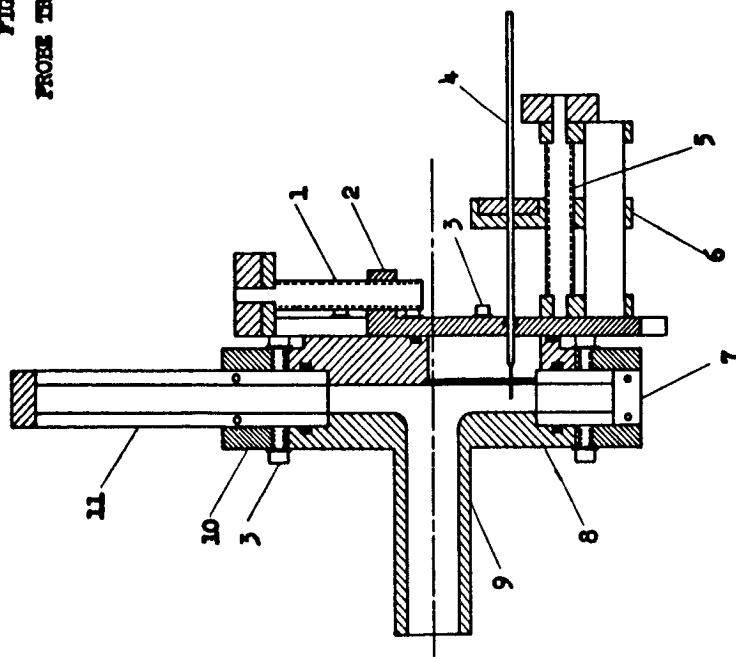
- 1) Measure more accurately the mass flow rate of the air supplied to the vortex,
- 2) Use larger settling chambers upstream of the nozzles, so that the inlet turbulence can be controlled,
- 3) Ascertain the effects of noncircular outer walls and nontangential driving jets,
- 4) Measure the total pressures in the vortex,
- 5) Measure the torques acting on various parts of the vortex chamber.

The first four of these improvements have all been incorporated into the present vortex chamber, and the fifth can be added easily.

The basic compressible vortex chamber model is shown in Figures 2-9 through 2-13. It consists of four nozzle blocks, which are bolted together to form the outer wall of the vortex chamber, and two sidewall plates, which contain the exit tubes and support the centerbody. The number of inlet nozzles can be changed by using one or more dummy nozzle blocks; the size or direction of the nozzles or the depth of the vortex chamber can be changed by using a different set of nozzle blocks. Changes in the exit tubes or centerbody are made by changing the sidewall plates. Thus the geometric design of the model is very flexible. The basic model has the dimensions of the hot-gas generator model, $r_w = 2$ inches, $r_i = 0.75$ inches, $L = 0.5$ inch, nozzle depth = 0.5 inch, nozzle width = 0.25 inch, and $\lambda = r_n / r_w = 0.875$.

The mass flow rate of the incoming air is measured by means of an upstream pressure tap and a throat pressure tap in each nozzle. Thus, the flow rate





1. Radial Traverse Screw
2. Radial Traverse Slider
3. Clamping Screw
4. Probe
5. Axial Traverse Screw
6. Axial Traverse Slider
7. Dummy Nozzle Block
8. Side-wall Plate
9. Exit Tube
10. Clamping Ring
11. Nozzle Block

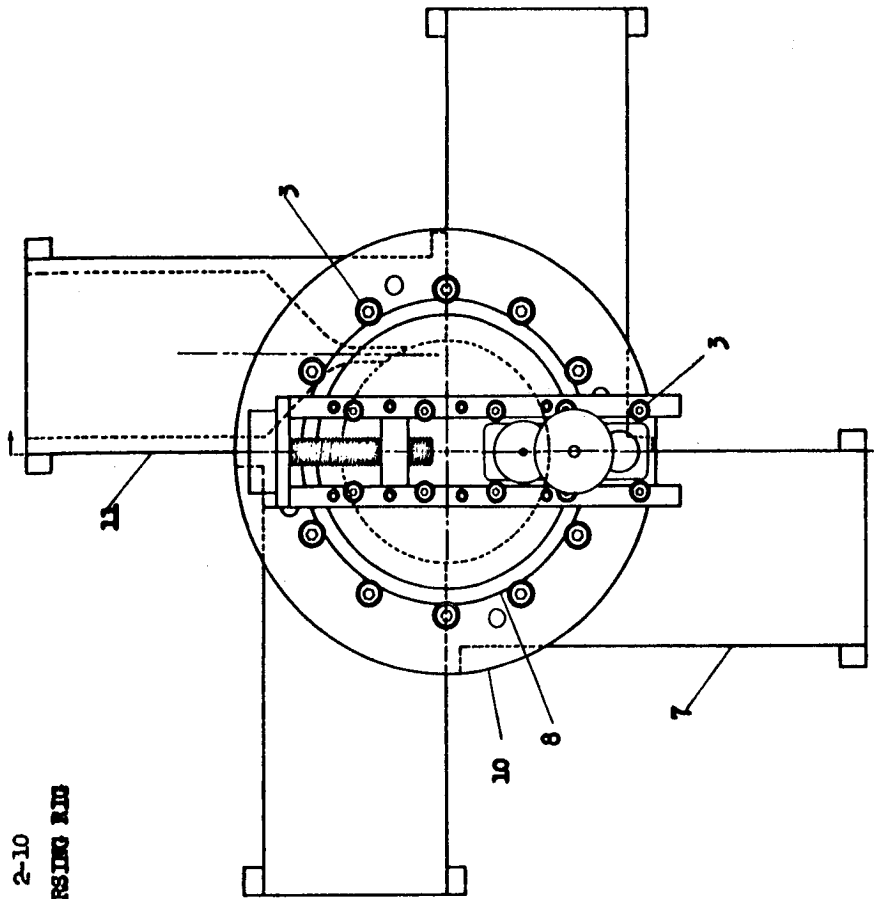
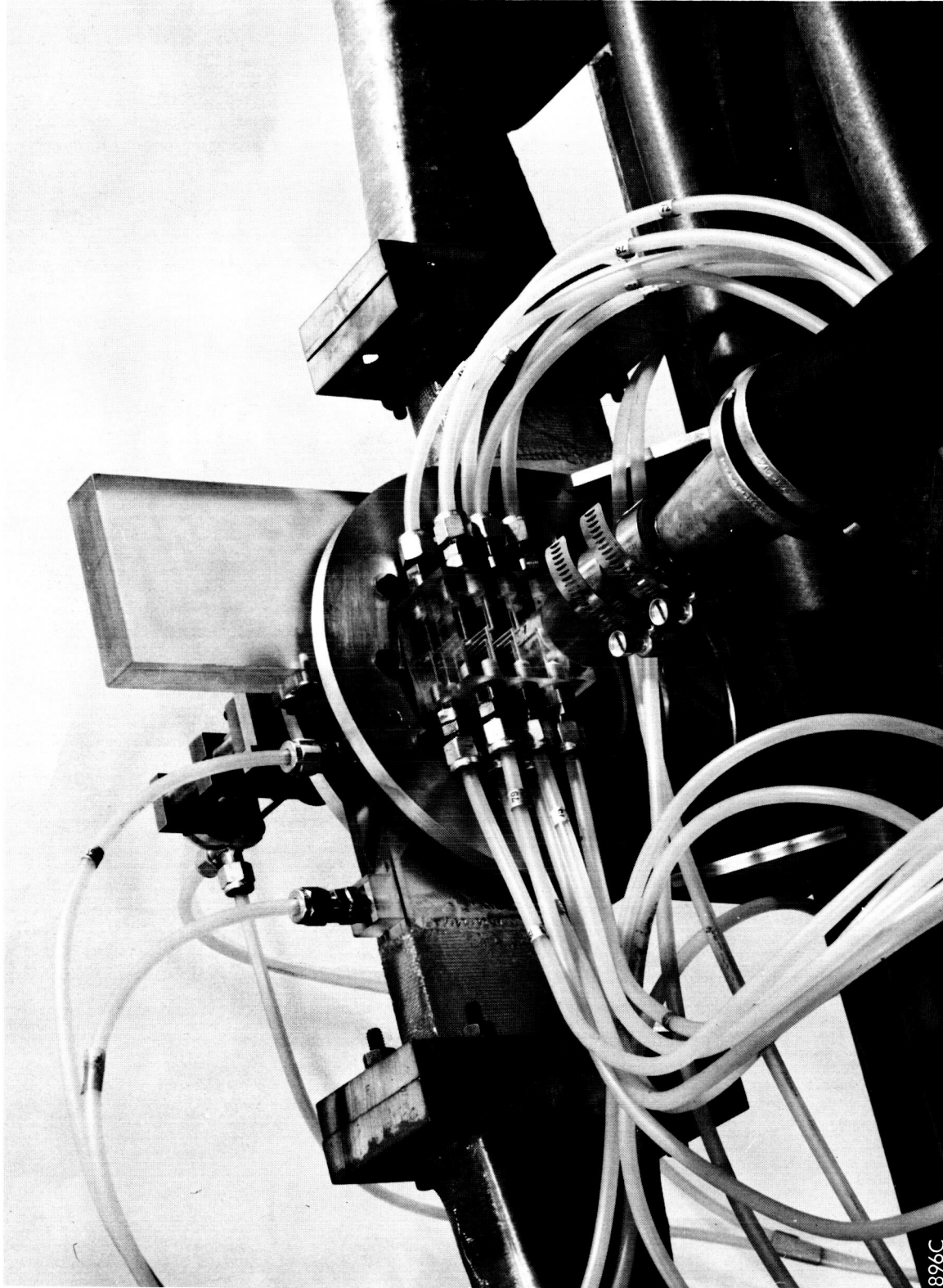


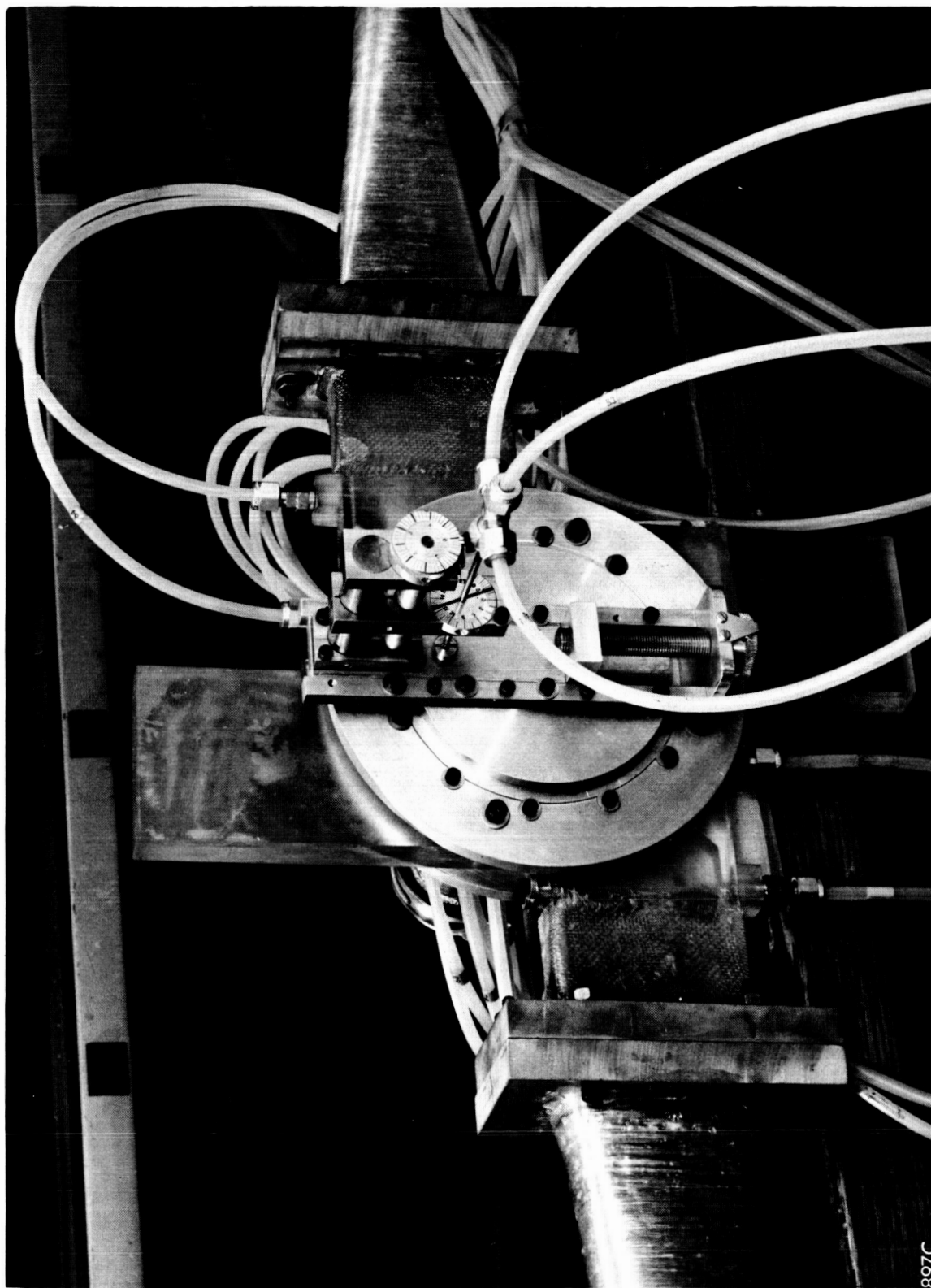
FIGURE 2-10
PROBE TRAVERSING RING



VORTEX CHAMBER, REAR VIEW
REVEALING RADIAL ARRAY OF STATIC PRESSURE TAPS

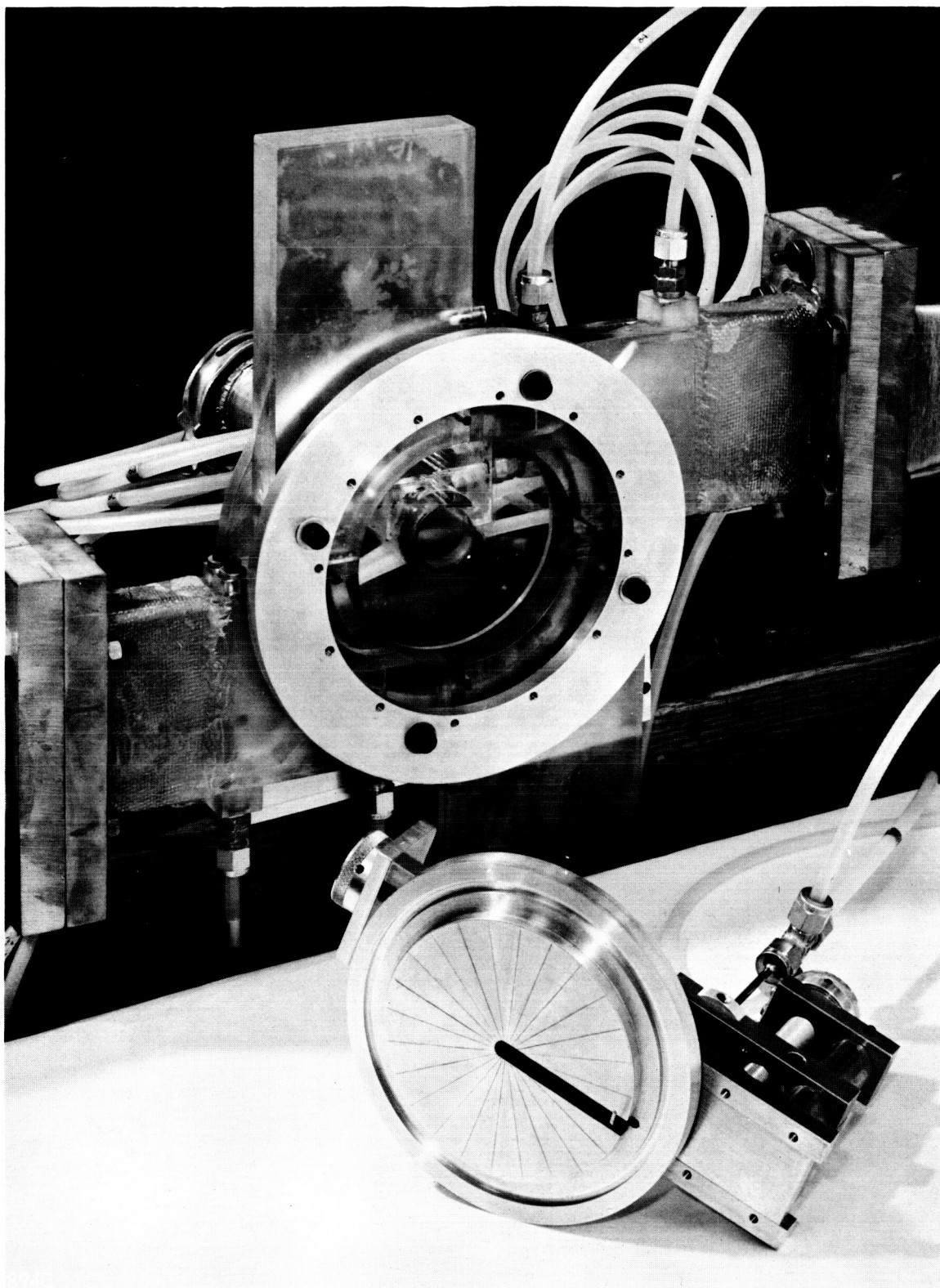
896C

FIGURE 2-11



VORTEX CHAMBER, FRONT VIEW
SHOWING PROBE TRAVERSING MECHANISM

FIGURE 2-12



VORTEX CHAMBER, DISASSEMBLED

FIGURE 2-13

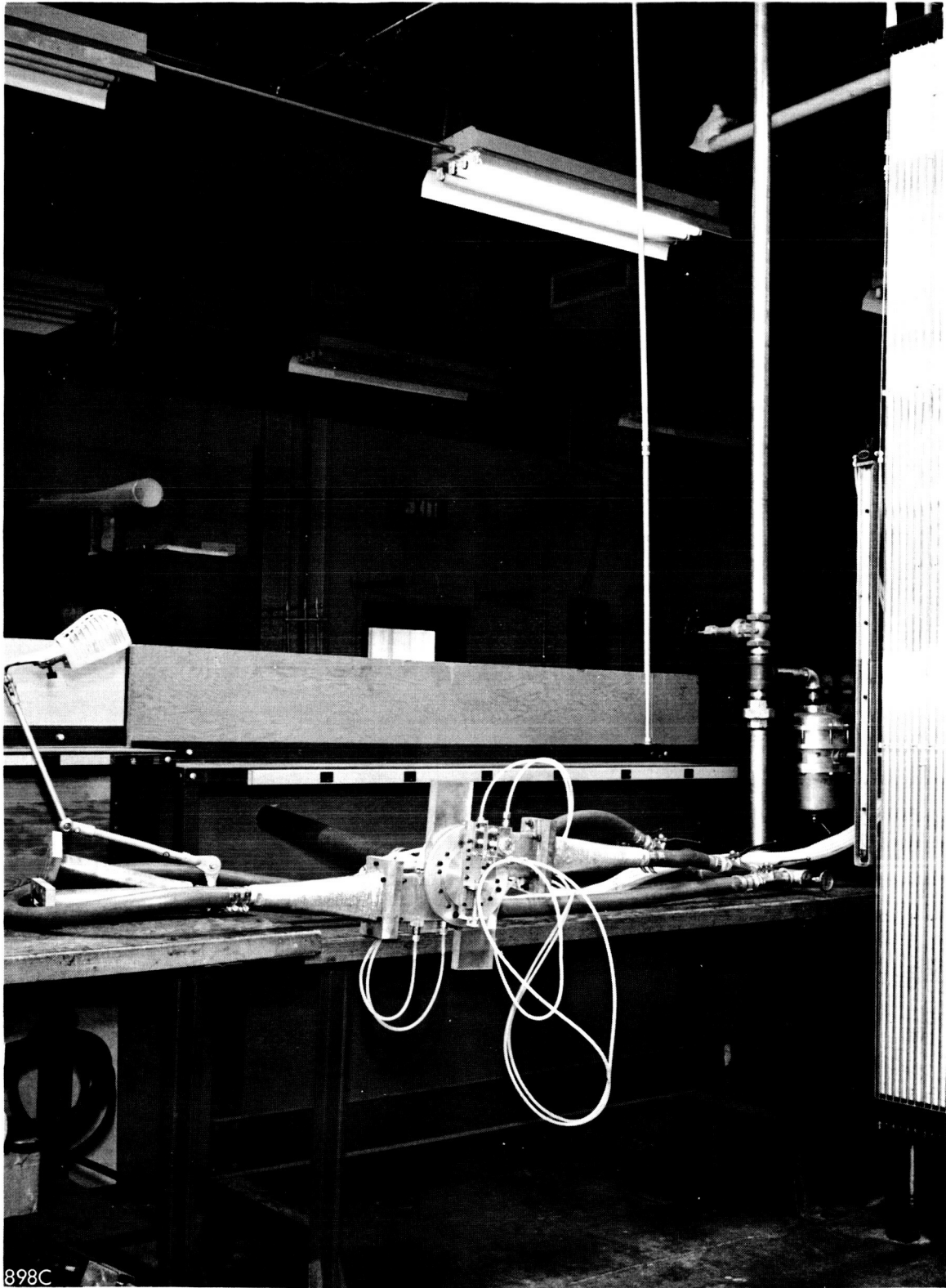
through each nozzle can be independently measured and controlled. The nozzle design is such that the flow entering the vortex chamber is uniform and parallel, and since each nozzle is an independent unit, the incoming turbulence does not depend on the number of nozzles in use.

Figures 2-10 and 2-12 show the traversing rig used with the flow probes. This rig replaces one of the sidewall plates, and allows radial, axial, or tangential probing traverses; a probe can be located at any point in the vortex chamber, and rotated in the plane of the vortex to determine flow direction.

Instrumentation employed in the experiments reported here includes a dial thermometer to measure upstream stagnation temperature, an upstream pressure tap and a throat pressure tap on each of the nozzles to measure nozzle flow rates, twelve static pressure taps spaced 0.125 inch apart on a radial line on one sidewall of the vortex chamber, and a total pressure probe with two side tubes for flow direction indication. Figure 2-14 shows these instruments installed in the vortex chamber (assembled with two inlet nozzles and two dummy nozzles) and the manometer bank employed.

The vortex chamber was pressure and leak tested by gradually increasing the inlet pressure to the nozzles, and checking for air leaks. Leakage was found to be no problem; the combination of circular and linear O-rings used in the model provides a good seal. However, noise was a problem. With a low flow rate through the chamber, the device was essentially silent, but as the flow was increased, a whistle began to develop which eventually changed to a scream, of a high enough intensity to be painful to everyone in the area, even when earplugs were used. The noise was found to come from the downstream end of the vortex chamber exit-tube, the whistle being due to an "organ-pipe" resonance of the exit tube, and the scream to the interaction of turbulent flow noise with the whistle. The scream was eliminated by placing a fine-mesh (105 wires per linear inch), high-porosity (47 per cent open) screen over the exit tube opening, and the whistle was eliminated by extending the exit tube with a long straight pipe or a diffuser and straight pipe. At present, the only noise made by the vortex model is the usual high-frequency flow noise.

In the course of preliminary testing, it was found that poor compressor regulation caused vortex pressure fluctuations of $\pm 1-5$ psi. In order to stabilize



VORTEX CHAMBER FACILITY

FIGURE 2-14

the pressures so that accurate measurements could be made, an air bleed line was installed upstream of the vortex. This line was designed to handle a flow up to the full output of the compressor. Thus, the compressor can be kept running continuously, even when the vortex chamber is being operated with a low through-flow. Tests showed that the chamber pressures were then steady, subject only to slow drift due to compressor warm-up and atmospheric pressure changes.

The first total pressure probe employed was found to have too large a spacing between the two directional tubes, making the probe overly sensitive to the radial pressure gradient in the vortex chamber. By redesigning the probe tip and taking greater pains in construction, the centerline distance between directional tubes was reduced from 0.036 inch to 0.015 inch, which was adequate for the experiments.

The inlet nozzles of the vortex chamber were designed to be used for flow metering; in order to obtain an accurate flow measurement from these nozzles, it was necessary to calibrate them with a standard commercial laminar flowmeter, accurate to $\pm 0.5\%$. Thus was determined the flow coefficient, k , defined as the ratio of the actual mass flow rate to that for an isentropic flow with the same inlet conditions and the same pressure ratio, versus the Reynolds number, Re_{DN} , based on the actual mass flow rate and the hydraulic diameter and fluid viscosity at the nozzle throat. The relation

$$k = 0.27189 + 0.14173 \log_{10} Re_{DN},$$

fits the nozzles within the accuracy of the experiment. This equation can not be expected to hold beyond the range of the experiments,

$$2(10)^4 < Re_{DN} < 1.7(10)^5.$$

2.2.3 Tangential Velocity Distributions The results presented here were obtained using two calibrated nozzles and two dummy nozzle blocks, symmetrically disposed. The choice of two nozzle operation was made on the basis that it best simulated the two jet operation of the hot-gas vortex generator and therefore would be immediately applicable to the analysis of generator performance.

The vortex chamber sidewalls were adjusted so that the radial line of the static pressure taps and that of a probe traverse were perpendicular to the axes of the two nozzles. The centerline of the two nozzles crossed this radial line at a radius ratio, $r_n/r_w = 0.875$. Both nozzles were operated at identical Reynolds number, Re_{DN} .

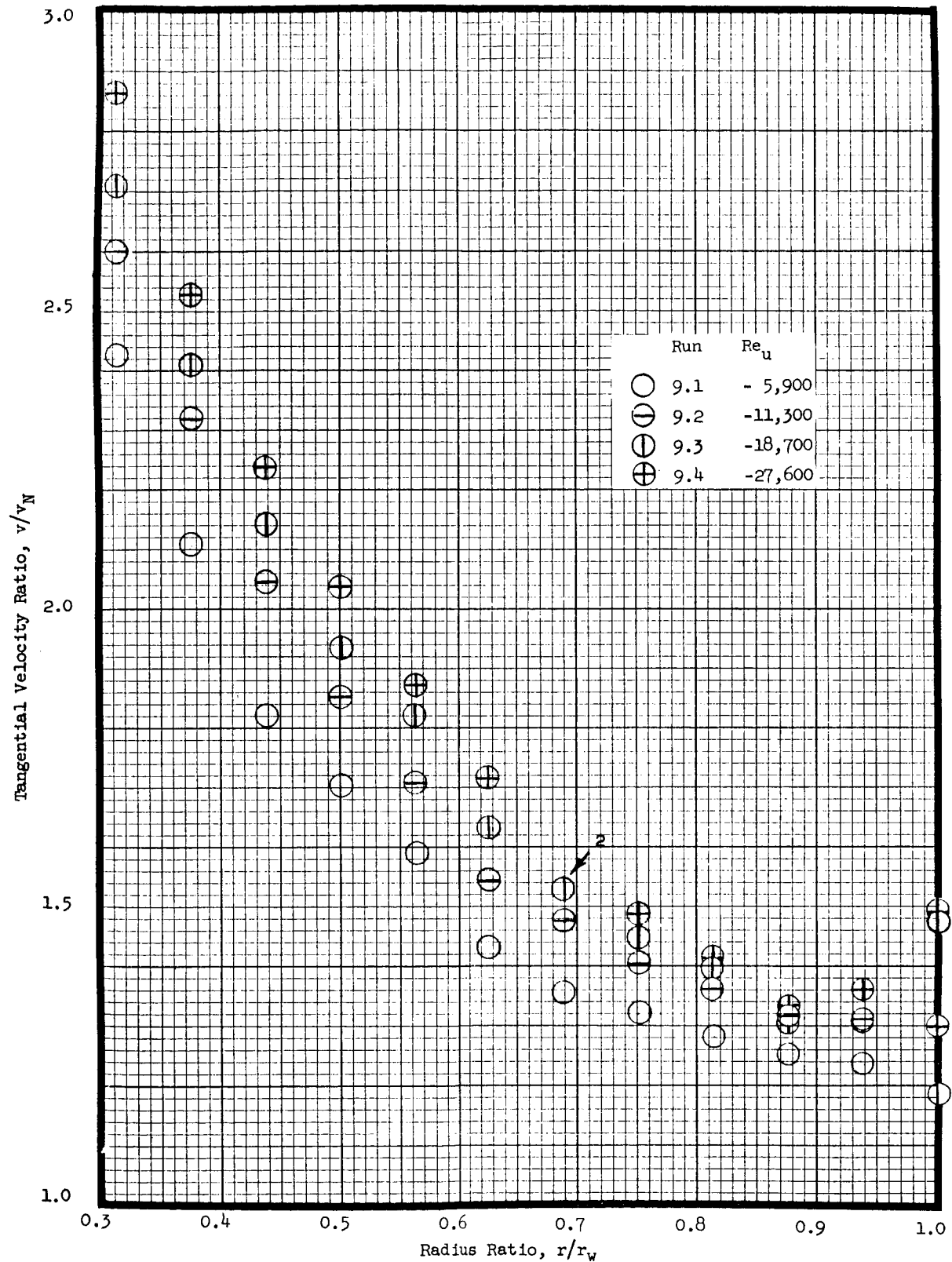
Radial distributions of the tangential velocity were calculated from the radial momentum equation of a one-dimensional, steady, vortex flow, assuming that the effects of viscosity, radial momentum, and compressibility are negligible:

$$\frac{dp}{dr} = \rho \frac{v^2}{r}$$

Pressure gradients were found by graphical differentiation of a smooth curve drawn through the measured static pressures; fluid densities were calculated for an adiabatic compressible vortex from the measured static pressures and upstream stagnation temperature. The resulting nondimensionalized velocity distributions for Run 9 are shown in Figure 2-15. The effect of radial Reynolds number on the distribution is more clearly evident in Figure 2-16 in which the nondimensional velocities are normalized with respect to their values at $r/r_w = 0.875$, the radius ratio of the nozzle centerlines. As expected the dimensionless velocity distribution is a very weak function of the Reynolds number. The apparent slight scatter of the data from a smooth profile is introduced by the graphical differentiation process; scatter was not evident in the measured pressure profiles.

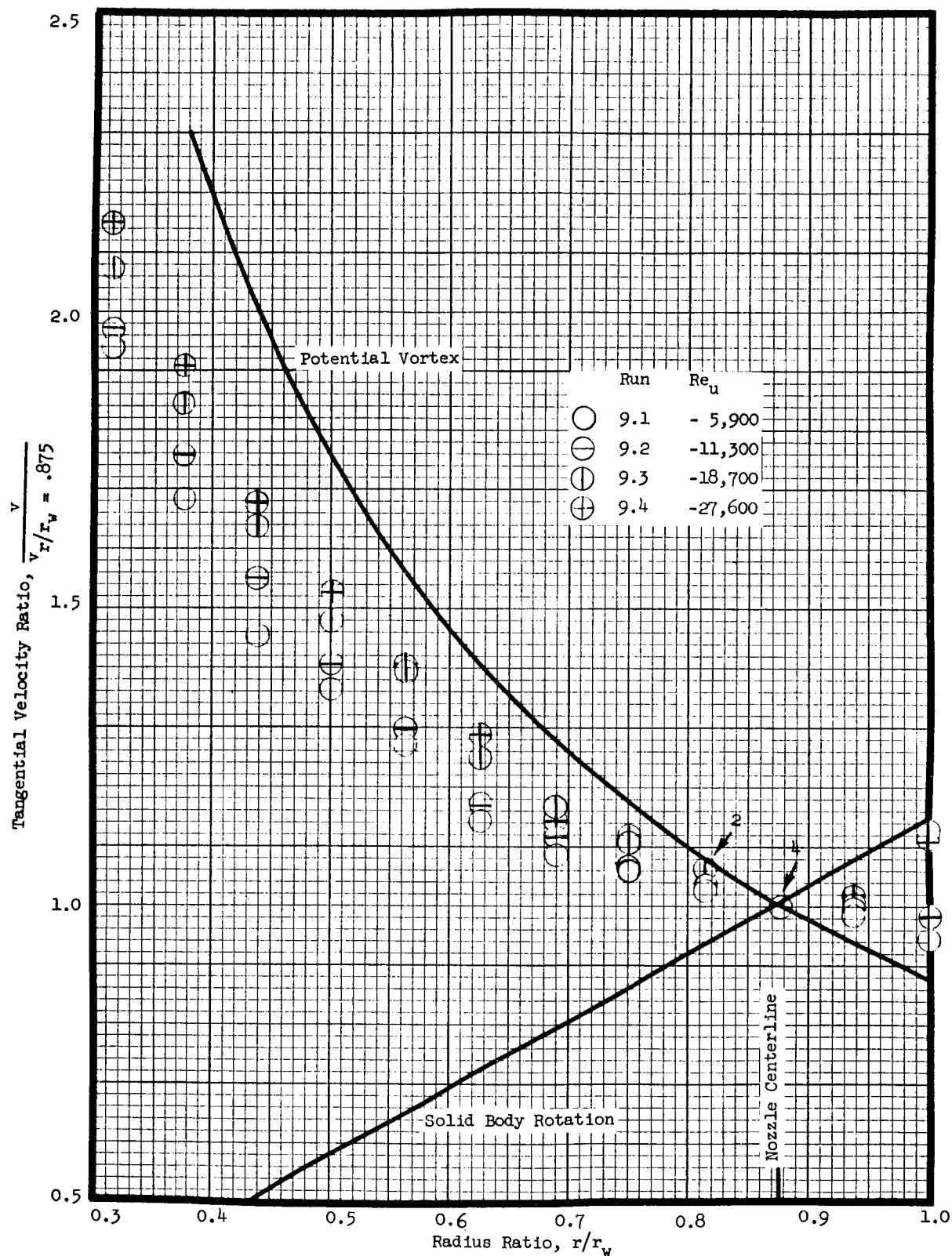
Also shown are curves for solid body rotation and for the potential vortex, each having a velocity ratio of unity at the nozzle centerline. Thus the family of curves represented in Figure 2-16 may be described as similar to a potential vortex between the exhaust tube and the jets issuing from the nozzles; in between the nozzle centerline and the wall all test curves lie between the two theoretical curves.

The velocities calculated from the pressure gradients are all significantly higher than at the nozzle throat. Thus, the indication is that the air continues to accelerate after it leaves the nozzles, due to the nontangential injection into the strong radial pressure gradient.



Vortex Chamber Tangential Velocity Distribution (dp/dr Derived)

Figure 2-15



Vortex Chamber Normalized Tangential Velocity Distribution (dp/dr Derived)

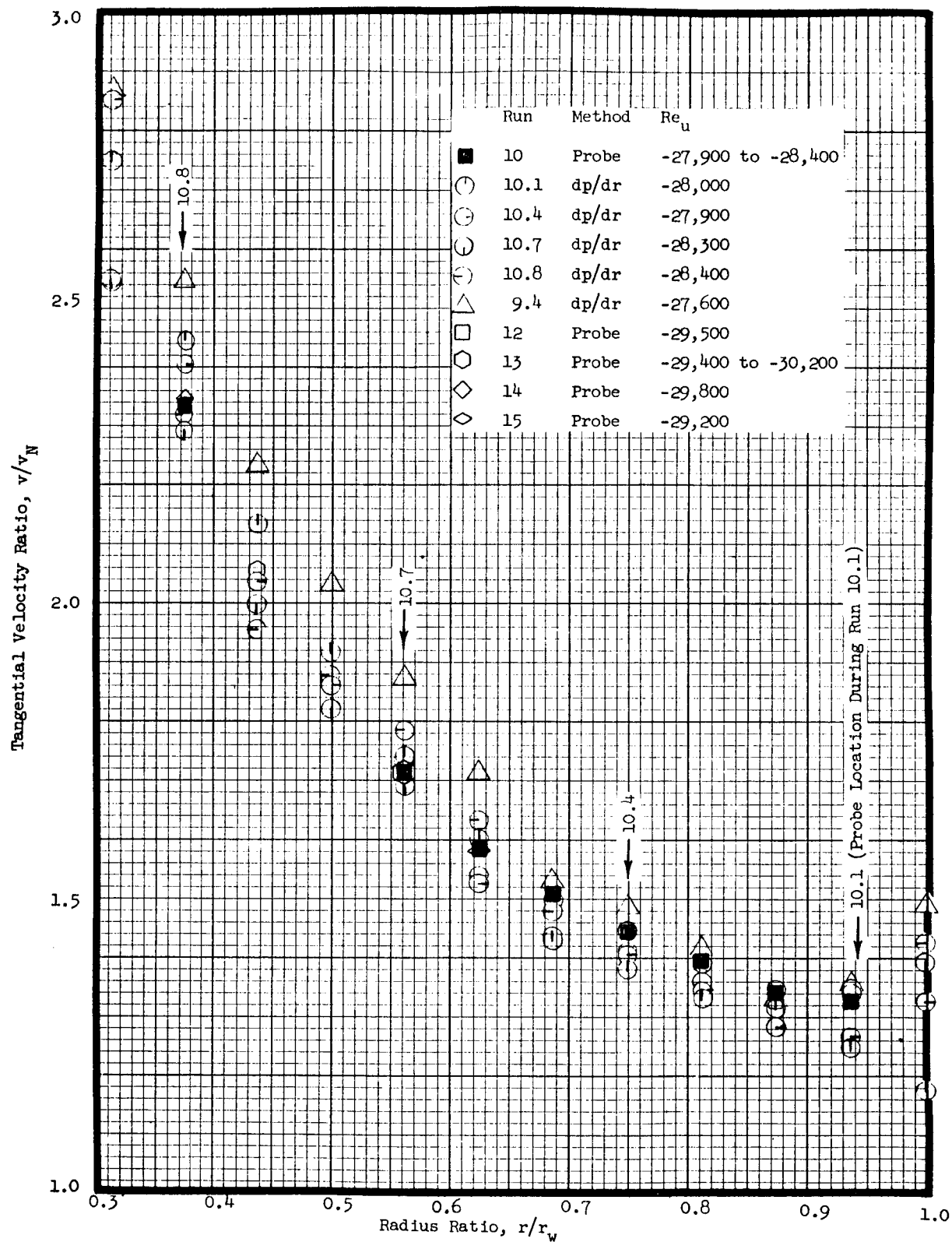
Figure 2-16

A radial probing traverse was made at a radial Reynolds number of - 28,000. The total-pressure probe employed was a Pitot-directional type fabricated from three 18-mil-outside diameter tubes with a 4-mil wall thickness. During the tests the probe was aligned to give a pressure difference in the directional tubes corresponding to the product of the measured static pressure gradient, the spacing of the directional tubes, and the sine of the angle between the probe axis and the chamber radius. The results, Figure 2-17, indicate that the probe itself influenced the flow to a small extent, but the tangential velocity distribution curve as determined with the probe agrees with the velocities determined from the wall static pressures. The comparison of the two velocity-determination methods is demonstrated more clearly in Figure 2-18 where the dp/dr derived velocity is determined at the radius ratio corresponding to particular probe locations. This technique to a large extent eliminates the data scatter of Figure 2-17 caused by probe-induced flow disturbances and thus indicates the validity of the dp/dr -derived velocity distributions. This conclusion is significant from the standpoint that data acquisition is more easily facilitated by the dp/dr method as compared to the probe method.

Values of probe determined velocities from Runs 12 through 15 are also included in Figure 2-17 to indicate the very high degree of reproducibility produced by this method.

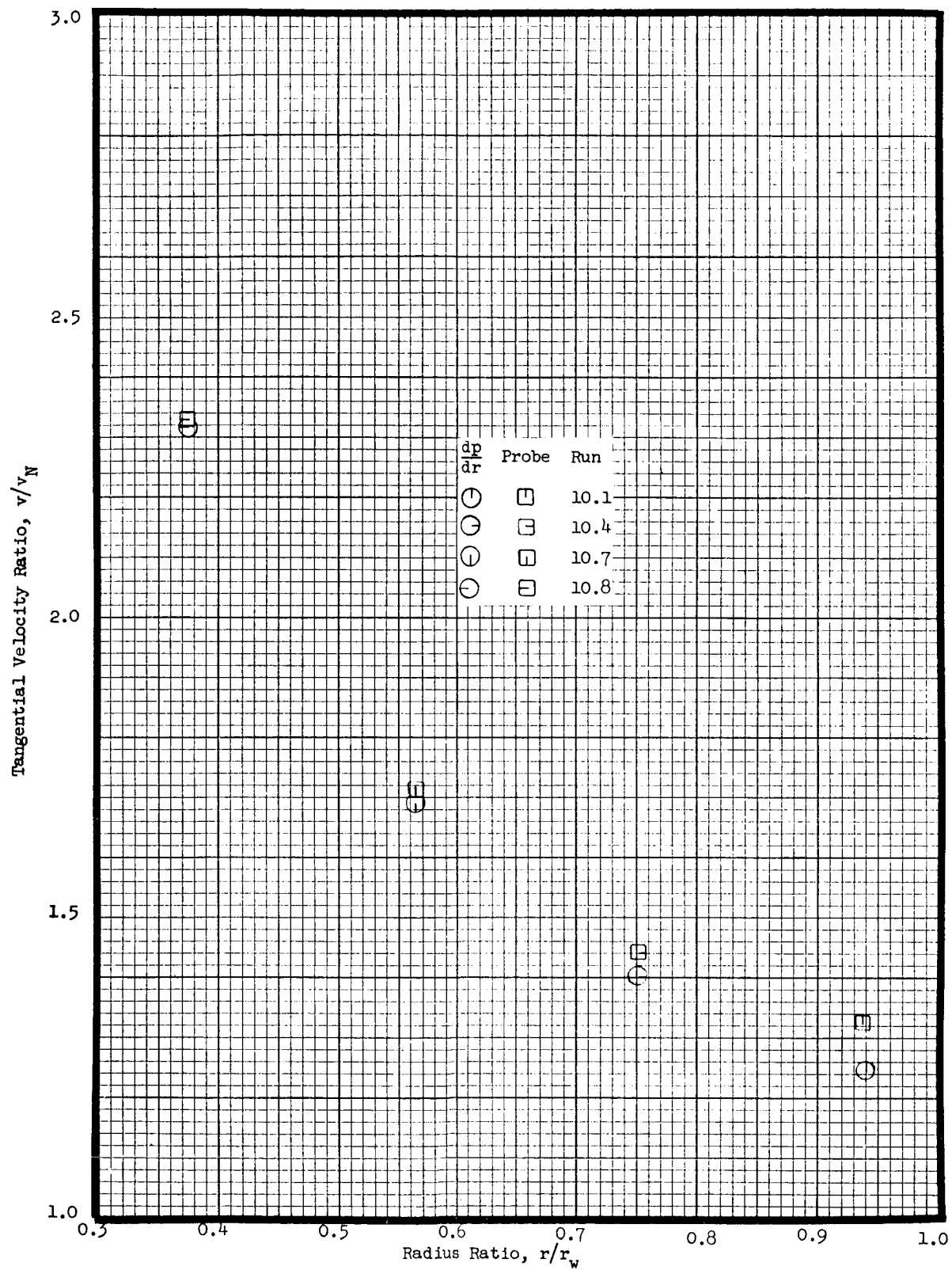
The probing rig sidewall, (see Figure 2-12) which contains a soft rubber strip to allow probe traversing, was found to give essentially the same behavior as a smooth sidewall. The comparison is illustrated in Figure 2-19 for a range of Reynolds numbers. Run 11 was conducted with a smooth wall as contrasted with Run 9 which was made with the probing rig in place, but with no probe inserted in the flow. Thus it may be concluded that the rubber strip in the probing rig sidewall gave rise to no discernible flow disturbances.

2.2.4 Sidewall Boundary Layer Velocity Distributions Additional probing runs were made in the vortex chamber to explore the possibility of significant boundary layer flow. Three axial traverses were made from the centerline to the wall of the chamber at radii of 1.75, 1.25, and 0.75 inches. All three traverses were made on a radial line which was perpendicular to the axes of the two nozzles. The results are presented in Figure 2-20. The outermost traverse showed a thin turbulent boundary layer with no measurable radial component, other than that of



Vortex Chamber Velocity Distribution; Pitot Probe vs dp/dr Derived Velocities

Figure 2-17



Comparison of Probe and dp/dr Derived Vortex Chamber Tangential Velocities

Figure 2-18

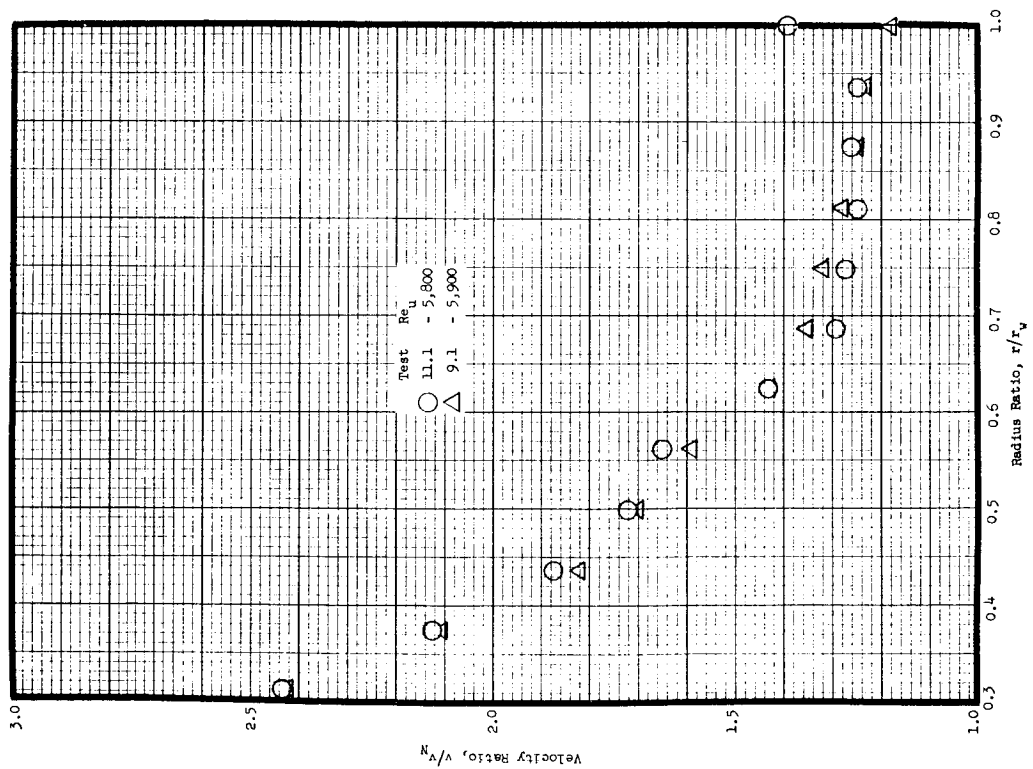


Figure 2-19 (continued)

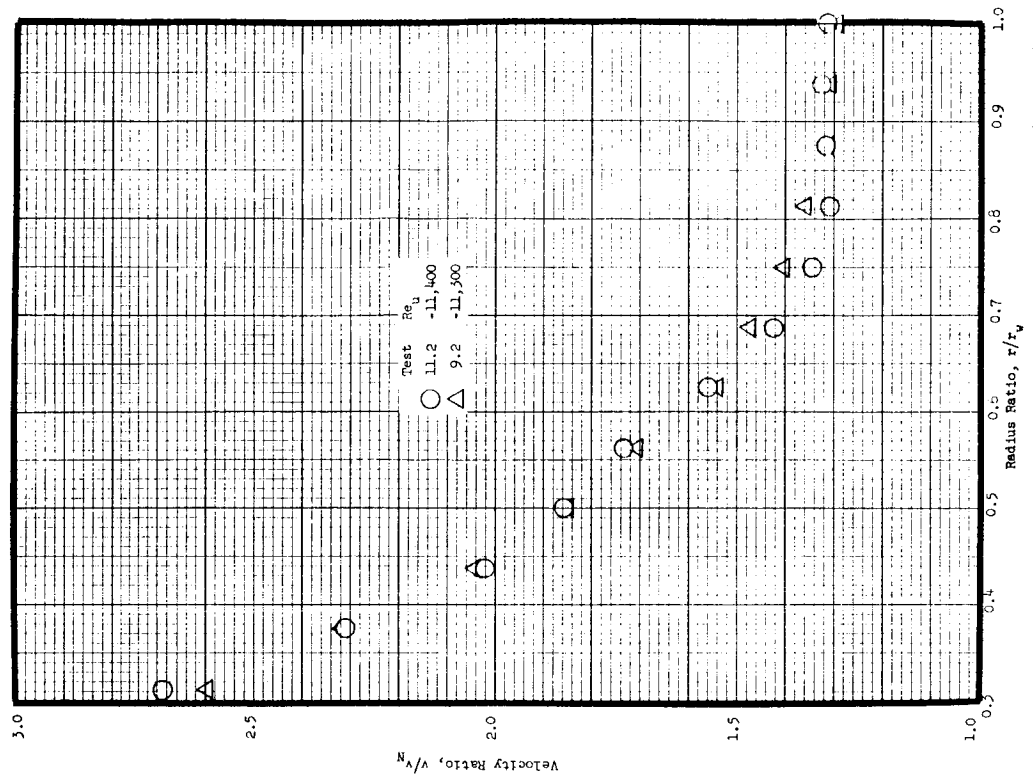


Figure 2-19 (continued)

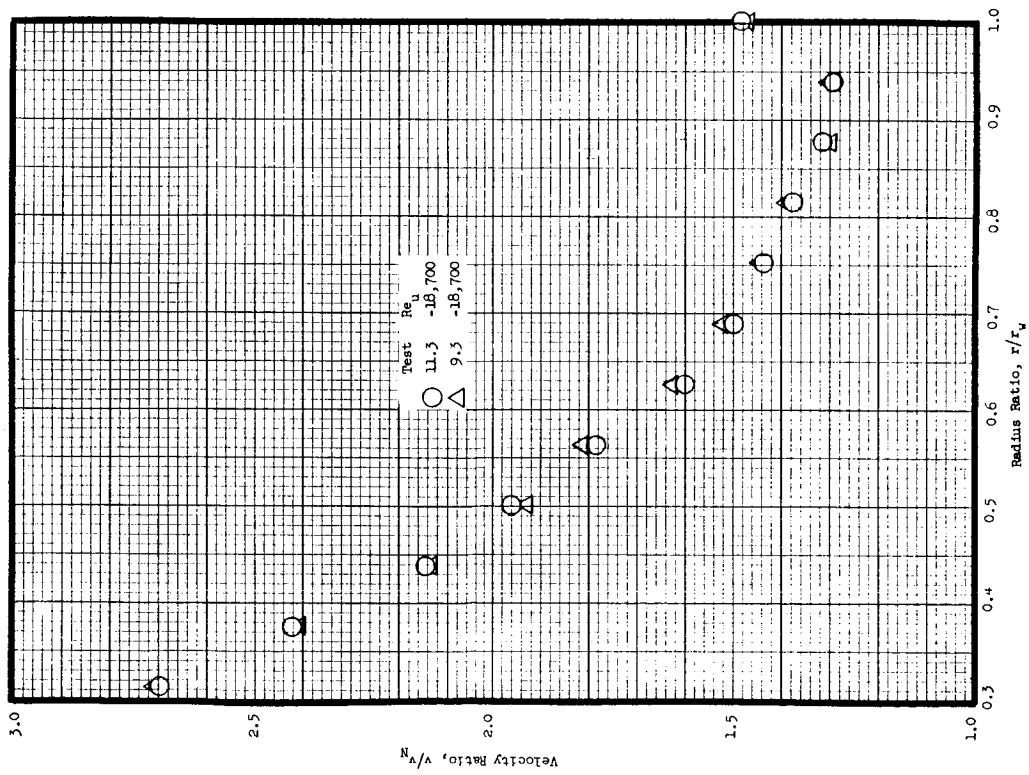
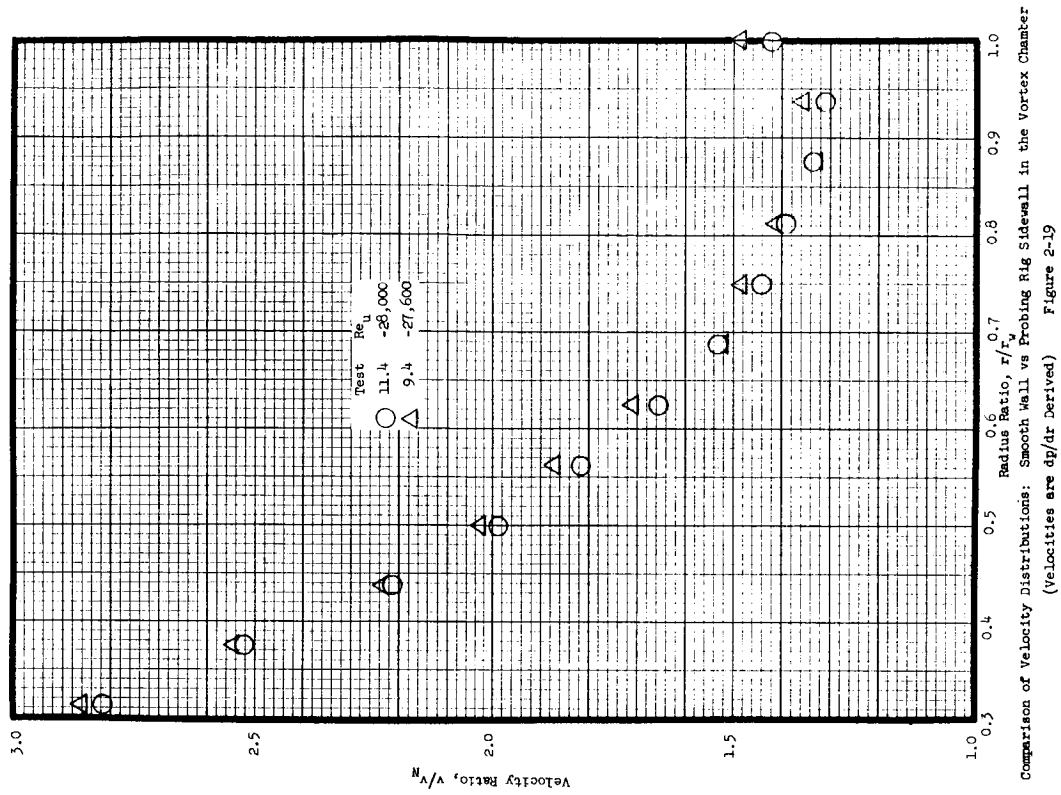
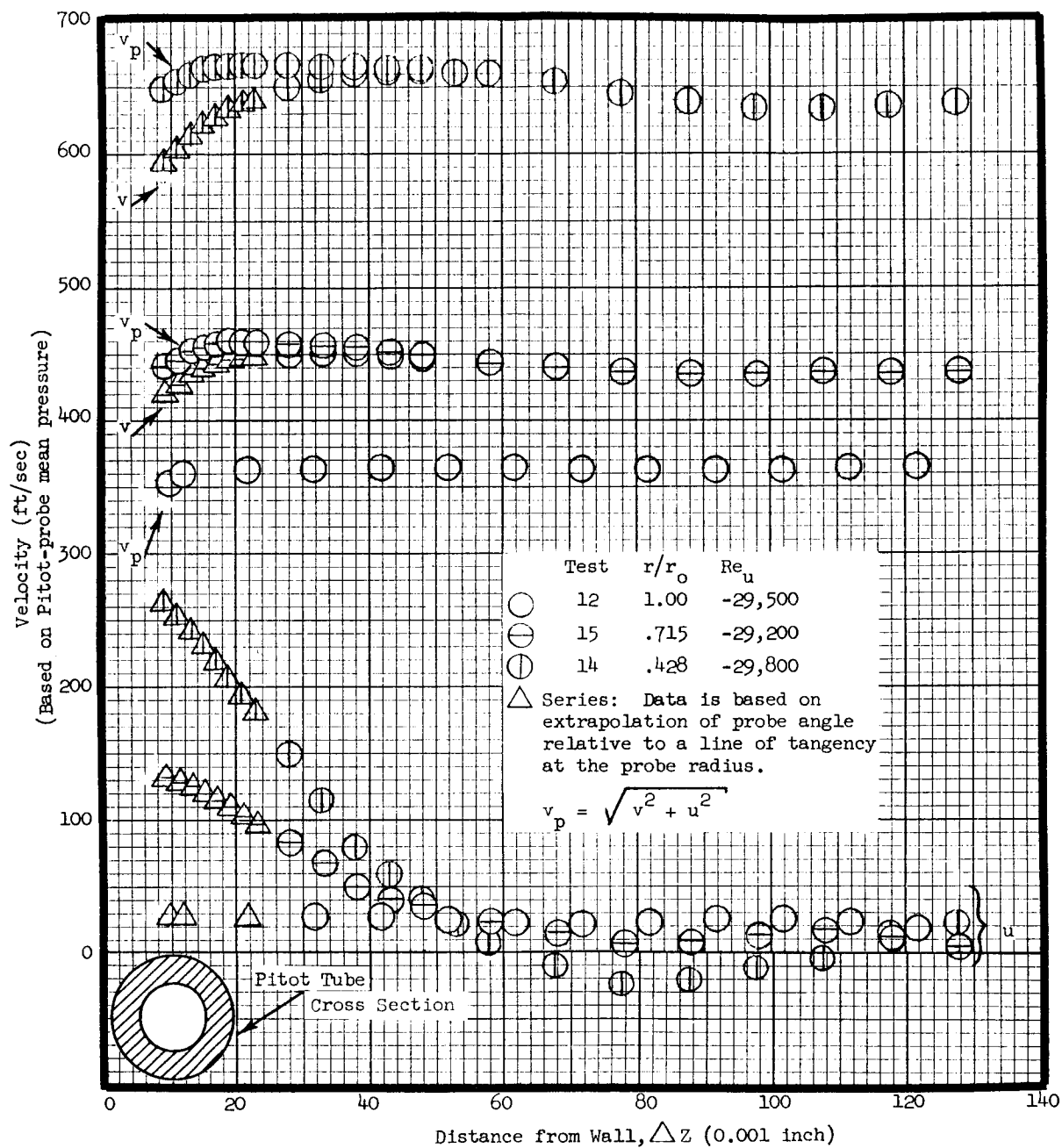


Figure 2-19 (continued)



Comparison of Velocity Distributions: Smooth Wall vs Probing Rig Sidewall in the Vortex Chamber
 (Velocities are dp/dr Derived) Figure 2-19



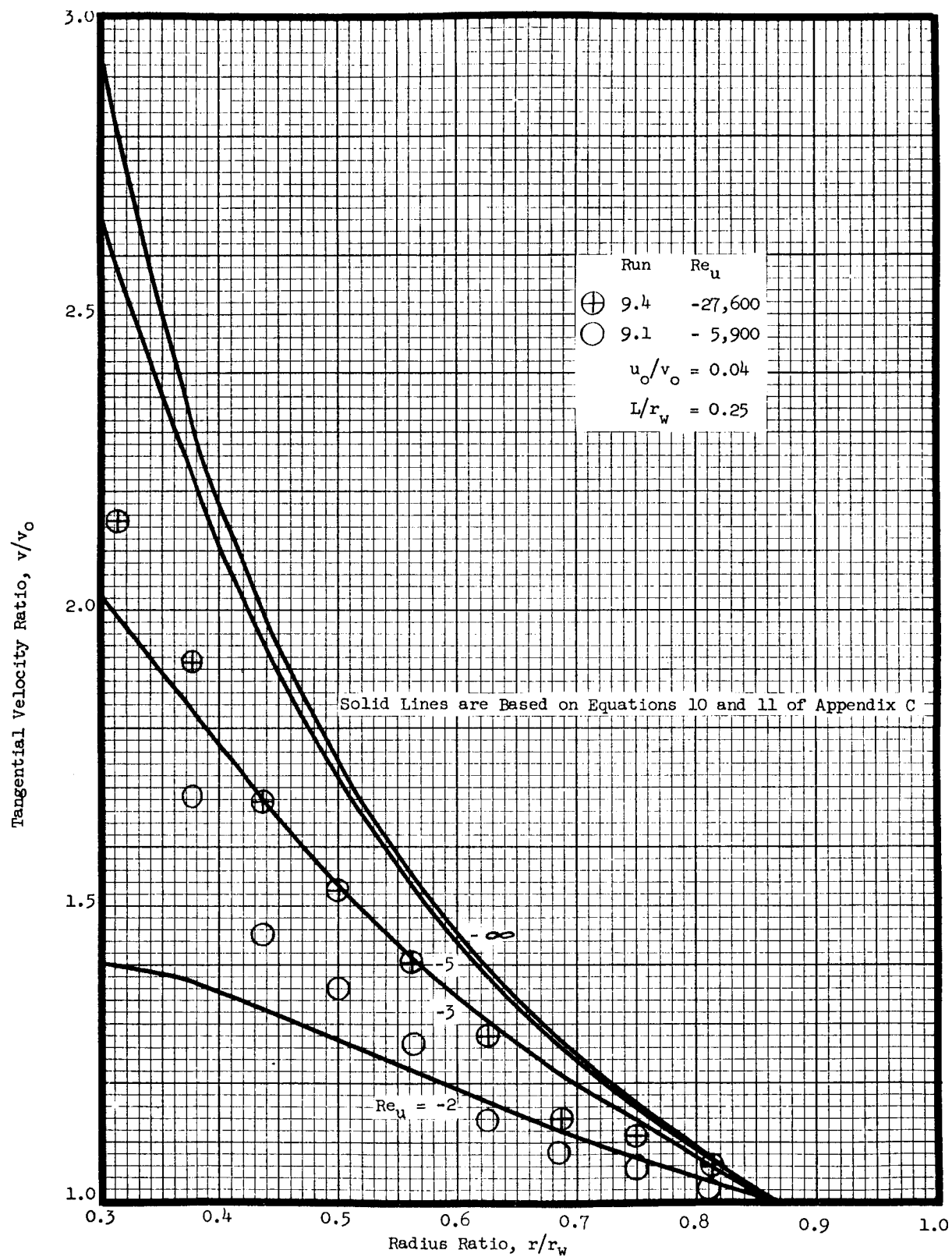
Sidewall Boundary Layer Flow

Figure 2-20

the main flow. The boundary layer thickness was approximately 0.012 inch, and the main flow appeared to be uniform. The second traverse showed a thicker wall boundary layer with a significant radial component. The boundary layer thickness at this point was approximately 0.080 inch. The tangential and radial boundary layer profiles were very similar to those of Reference 11 which showed a slight rise in the tangential velocity and then a $1/n$ - power decrease near the wall. In the present experiments the radial profile could not be determined exactly near the wall because of the probe construction but it appeared to be roughly triangular. The maximum estimated radial velocity was of the order of 200 feet per second compared to a main flow tangential velocity of 470 feet per second. The innermost traverse showed these same characteristics further intensified. The boundary layer thickness was approximately 0.100 inch and the radial profile was much more pronounced. Again the profiles were very similar to those of Reference 11. The radial profile shows a small low-velocity back-flow region near the core flow. The maximum radial velocity was estimated to be of the order of 400 feet per second compared to a main tangential flow velocity of 680 feet per second. At this point the radial boundary layer carried most of the through-flow of the device. Thus, the sidewall boundary layer has been found to be much more important than previously estimated; further work on this phenomenon is imperative.

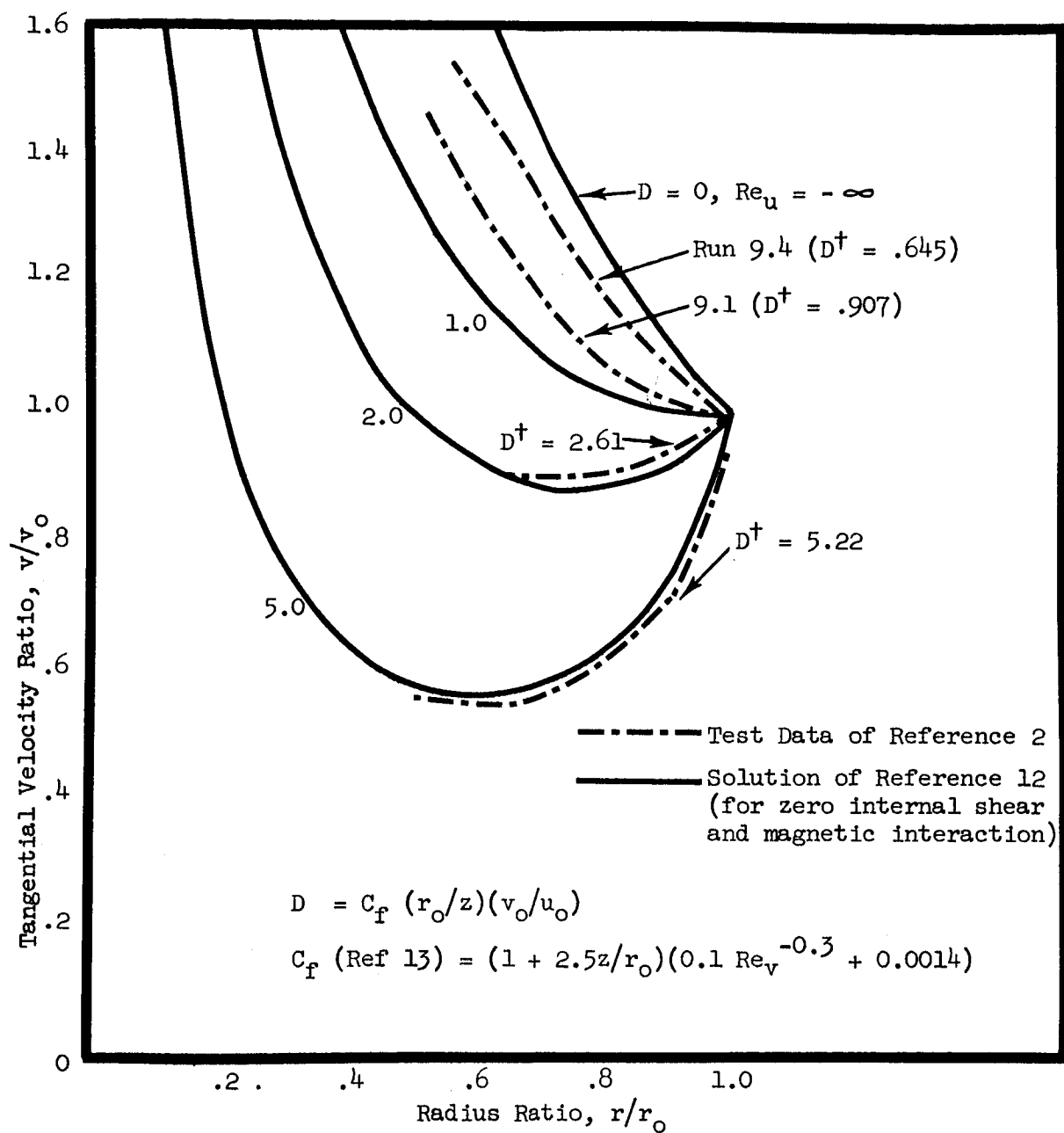
2.2.5 Discussion of Results The results presented in the two previous sections correlate to a reasonable degree with the analytical expressions for velocity distributions in a two-dimensional vortex. However the vortex chamber employed in the experiments was of relatively low aspect ratio and consequently the strong sidewall boundary layer radial flow (secondary flow) and viscous drag on the core fluid must be taken into consideration.

Figure 2-21 presents the measured tangential velocity distributions for the extremes of Reynolds numbers in Run 9. The analytical distributions for various pseudo-laminar velocity profiles are also indicated. Thus it is seen that the profile shapes strongly resemble the analytical profiles, particularly for the greater of the two Reynolds numbers. The deviation of the analytical and experimental profiles is greatest at the minimum value of Reynolds number obtained and at the outer radii. The deviation can be explained by noting the influence of wall drag on tangential velocity profiles, Figure 2-22. The data of the present



Comparison of Experimental and Analytical Velocity Profiles

Figure 2-21



Comparison of Tangential Velocity Profiles
as Influenced by Wall Drag Figure 2-22

work, as well as several of the Reference 2 profiles, appear to be correlated very well at the outer regions of radii by the hypothesis that the wall drag is a dominant factor in determining velocity profiles for operation of small aspect ratio vortex flows at low Re_v .

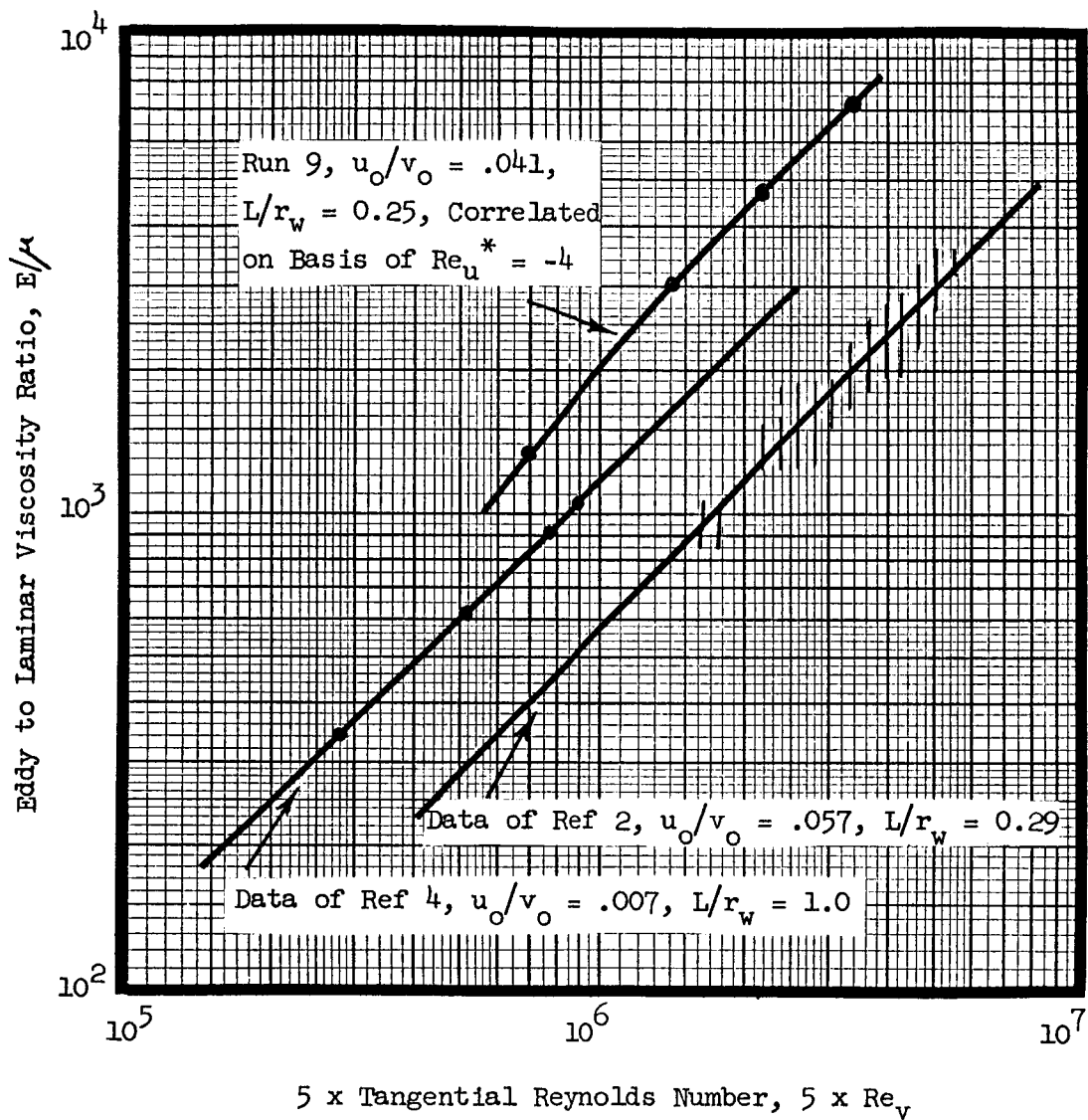
The present results also indicate that the effective eddy viscosity is higher than that predicted by the theory presented in Section 2.1.3. The reason for this is believed to be, in view of the strong secondary flow measured, the substantial portion of total throughput flow which is involved in the sidewall boundary layers; consequently the radial Reynolds number, Re_u , of the core flow is adversely affected.

Figure 2-23 indicates a comparison of the eddy to laminar viscosity ratio for several different experiments. The theory of Section 2.1.3 indicates that the E/μ ratio is a sole function of the u_o/v_o ratio at a given tangential Reynolds number, i.e.,

$$E/\mu = \frac{K^2}{2} Re_v$$

where K is the mixing length parameter and a function only of u_o/v_o (see Figure 2-5). Thus on this basis alone the present results, at a u_o/v_o ratio of 0.041 could be expected to produce an E/μ ratio curve bounded by those of References 2 and 4 in Figure 2-23. However, on the basis a theory developed by Mack¹⁴ for laminar sidewall boundary layers in vortex flow, the boundary layer is expected to be relatively insignificant in the experiments of References 2 and 4, as a result of the small values of Re_v in the former and the large aspect ratio, L/r_w , of the latter. The boundary layer flow was shown to be dominant to that of the core flow and also turbulent in the present experiment. Thus the involvement of such a large portion of total flow that occurs in the boundary layer should be considered when attempting to correlate the tangential velocity distributions and effective viscosities of the core flow.

A better appreciation of the comparison of boundary layer effects for the present experiments and those of Reference 2 is obtained by applying the analysis of Mack¹⁴ to the Reference 2 data. This would indicate that at $Re_v = 10^5$, $u_o/v_o = 0.057$, and $L/r_w = 0.29$, 22 per cent of the total mass flow was in the two sidewall boundary layers of the Reference 2 vortex device. Incidentally at $L/r_w = .56$



Correlation of Viscosity Ratio
with Tangential Reynolds Number Figure 2-23

approximately half of the above percentage is in boundary layer flow, thus explaining why very little aspect ratio effect is evident in the data of Reference 2 presented in Figure 2-2. This analysis is based on the assumption of a laminar boundary layer. This assumption is probably valid for the Reference 2 data inasmuch as the tangential Reynolds numbers are all lower than the transition value of 3×10^5 found by Gregory, Stuart, and Walker¹⁵ for a rotating disk in still air. However exact transition values for boundary layers in jet driven vortex flows have yet to be determined. For a turbulent boundary layer, as was apparently the case in the present experiments at an $Re_v \approx (7)10^5$, the mass flow through the boundary layer is expected to be proportional to $Re_v^{4/5}$ (with the Blasius skin-function law) instead of $Re_v^{1/2}$ for a laminar boundary layer. Thus the ratio of boundary layer flow to core flow will be larger in a turbulent boundary layer for all Re_v greater than some low value. This situation appears to have existed in the present experiments at the upper end of the range of tangential Reynolds numbers.

In conclusion, it appears that the analyses of Section 2.1 are valid for turbulent vortex flow if the aspect ratio is sufficiently large, otherwise the effects of wall drag and boundary layer flow must be taken into consideration.

The experimental techniques applied in this study were shown to give self-consistent results and capable of yielding two-dimensional velocity distributions throughout the annular region of a vortex chamber.

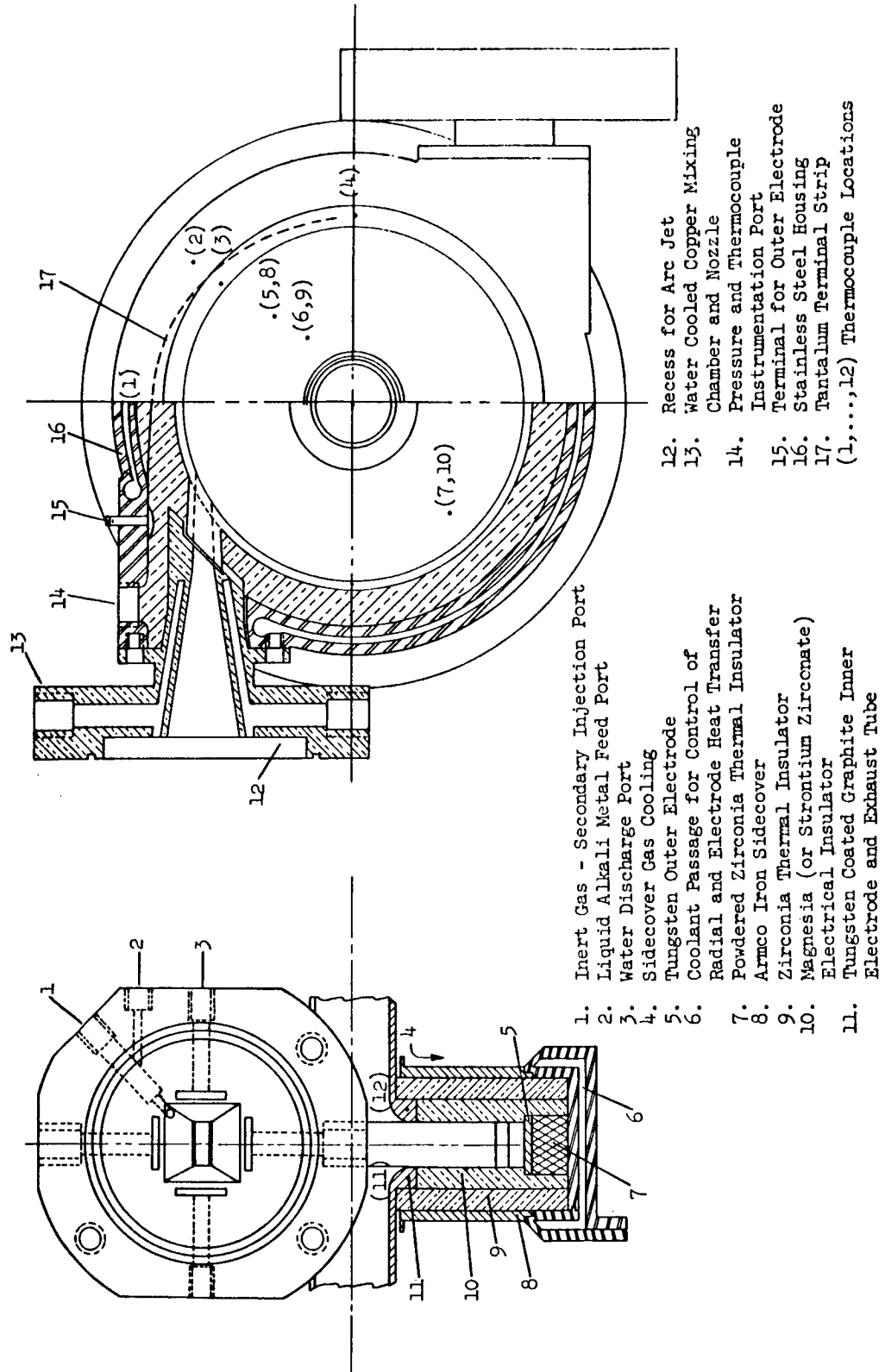
3.0 VORTEX MHD GENERATOR OPERATION

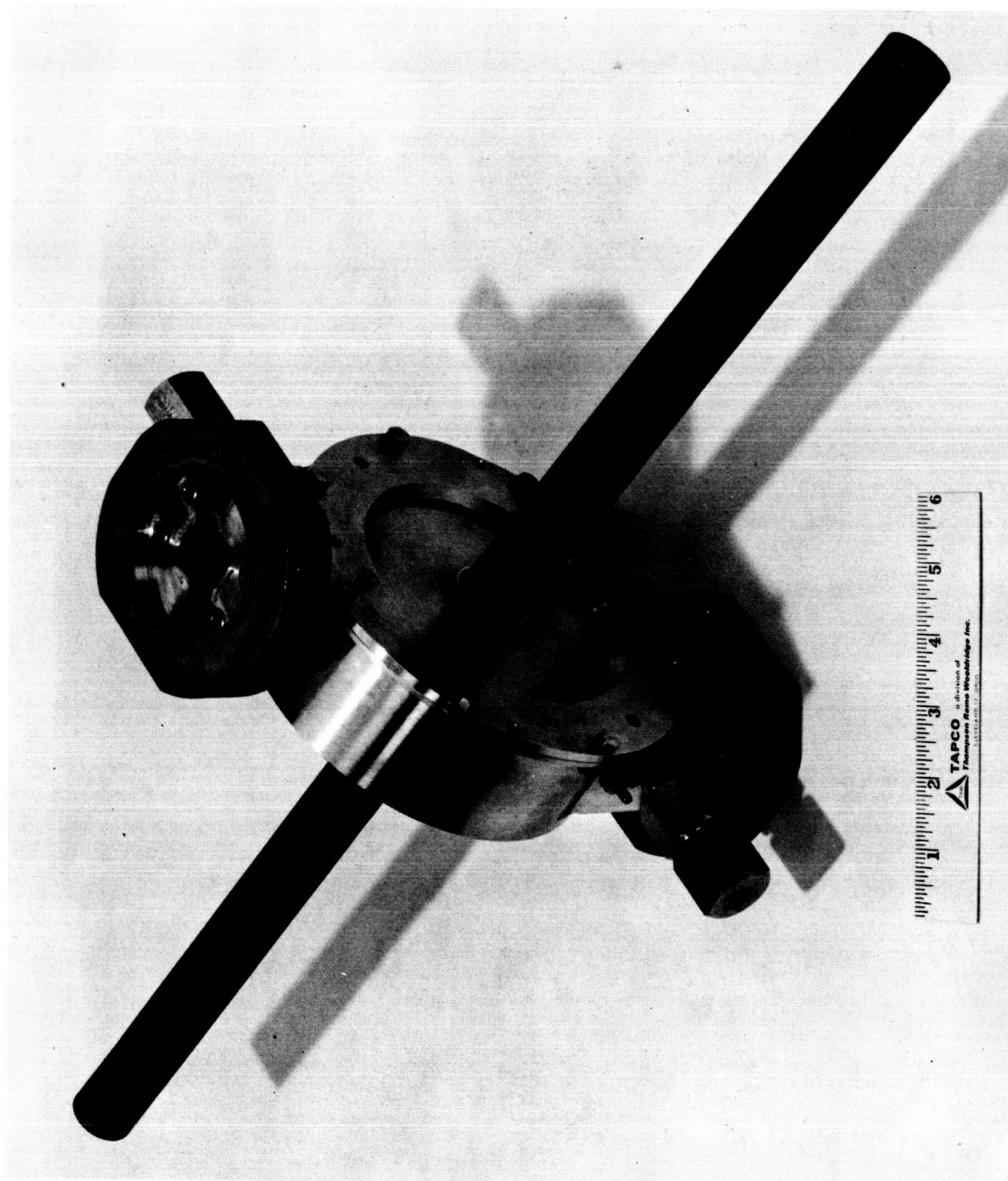
Based on the recommendations of the preceeding NAS5-703 contract, the initial efforts on the present vortex generator program commenced with the acquisition and installation of a dual arc jet facility. The arc jets are identical Plasma-dyne M-4 subsonic heads coupled to two power supplies (each rated at 40 kw continuous, 60 kw peak) for separate or simultaneous operation. Simultaneous operation of both arc jets provides a factor of four increase in the plasma mass flow capability as compared with previous operation. Thus, the increased flow rate, approximately 25 gm sec^{-1} of seeded argon, minimizes the relative importance of the auxiliary phenomena which were encountered in the earlier program. The effects associated with single and multiple jet-driven vortices, previously investigated only in cold gas experiments, were then studied in hot gas power generation experiments.

3.1 Design of the Experimental Vortex MHD Generator The design of an advanced experimental model of the vortex MHD generator was completed and fabricated without any significant difficulty. This model incorporates the changes and refinements suggested by the preceeding NAS5-703 research program. Also included are means for more extensive instrumentation, particularly for the determination and independent control of the sidewall and radial heat transfer from the confined plasma. Significant improvements have been effected in the design of the gas entry region including the nozzle itself. The nozzle is of minimum length and two dimensional, thereby providing a less turbulent jet with an optimum configuration for vortex driving. Figures 3-1, -2, and -3 illustrate the above-mentioned features.

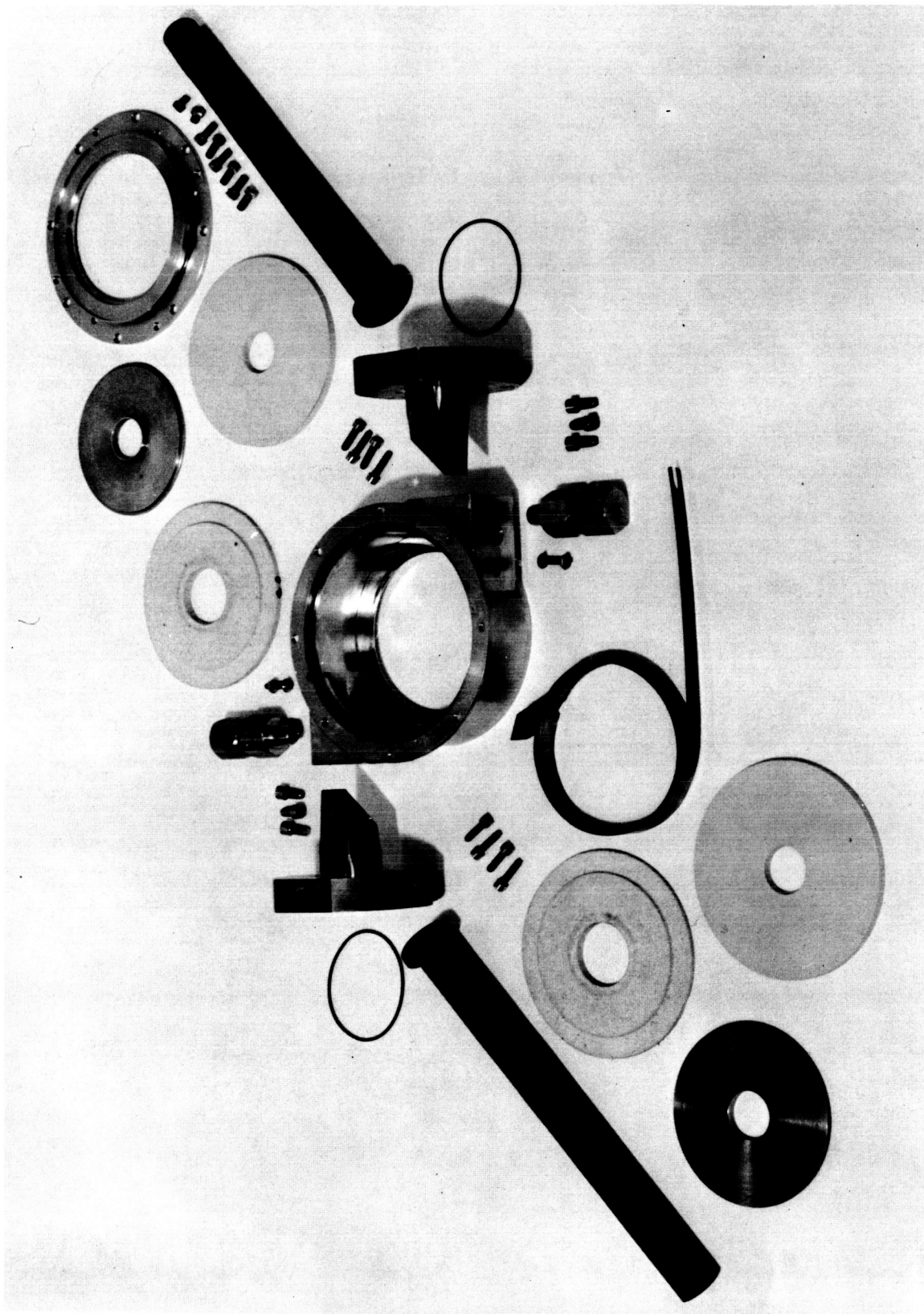
The design of the water-cooled mixing chamber-nozzle accommodates injection of an alkali metal seed material into a region provided for mixing the seed with the arc heated argon; this same region promotes uniformity of the thermodynamic properties of the plasma jets. One of the water-cooled nozzles of the vortex generator was tested by operating it with maximum arc heater input power of 60 kw and discharging into the atmosphere. The water temperature rise was 25°F for 3.2 gpm flowing under a heat of 45 psid. Heat dissipation in the nozzle was thus 12 kw. Operation under these conditions for four minutes did not produce any deterioration of the nozzle. Subsequent operation of the nozzles during generator operation also produced no deterioration.

Experimental Model 1 - Vortex MHD Generator Figure 3-1





EXPERIMENTAL MODEL OF THE VORTEX MHD GENERATOR



VIEW OF THE VORTEX GENERATOR DISASSEMBLED

FIGURE 3-3

Seeding was accomplished either by injecting an aqueous solution of an alkali metal compound (cesium hydroxide), or by injecting the alkali metal (cesium) in a liquid form. The latter method offers the advantage of helping to establish a plasma of relatively simple composition which is free of oxidizing constituents. Furthermore, the electrical conductivity is maximized because of the absence of poisoning constituents, e.g., the electronegative hydroxyl radical.

Various methods of vaporization and atomization of cesium were considered. Because of the need to conserve the relatively expensive cesium and to expedite test sequences with the MHD generator, a system having a fast response to control was sought. These objectives were satisfied by metering the flow of a nonreacting fluid, xylene, which in turn pumped the liquid metal directly to a gas-liquid atomizer; the resulting spray was subsequently directed into the jet issuing from an arc heater. Separate seeding systems were employed for each driving jet. Calculations (based on an analysis of atomization presented in Reference 2) indicated that a diversion to the atomizers of ten per cent of the total argon flow should be capable of producing droplet diameters of approximately 6 and 23μ respectively for potassium and cesium, and that subsequent vaporization in the arc heated argon takes place very rapidly - within a fraction of the length of the mixing chamber - according to a calculation procedure devised by Shapiro and Hawthorne³. Thus, equilibrium ionization was likely in the jets entering the cavity of the vortex generator.

Accordingly a seed injection mechanism was developed and operated for trial purposes by discharging seed solutions, consisting of concentrated aqueous solutions of cesium hydroxide, into the atmosphere. The device consists of an arrangement whereby two diametrically opposed streams of seed solution are directed perpendicularly into a high velocity jet of argon. The resulting atomized spray is then ducted into the generator nozzle mixing chamber adjacent to the front electrode orifice of an arc heater. Subsequent mixing of the impinging spray and arc heated argon produce the required plasma. Operation of the injection mechanism in conjunction with the generator nozzle gave no visible indication of distortion of the nozzle jet. Operation of the injection mechanisms during generator operation appeared to give satisfactory performance with either aqueous solutions of cesium hydroxide or liquid cesium. The latter seed substance was actually an alloy of cesium plus nine per cent (by weight) of NaK (78 per cent K,

22 per cent Na) which was purposefully added to obtain a liquid alloy of low solidification temperature and thereby to simplify the delivery system.

The location of the jets with respect to a purely tangential entry into the vortex cavity was chosen on the basis of maximizing jet velocity recovery, considering the momentum loss⁴ due to shear on the outer cylindrical surface. Thus, the effective vortex driving velocity was calculated to be 0.9 of the incoming jet velocity, for a radial Reynolds number $Re_u^* = 66$ based on an effective eddy viscosity. The design of the generator, Figure 3-1, offers sufficient latitude in component design that relocation of the jets is easily accomplished should other arrangements appear more desirable.

Furthermore, nozzle expansion ratios may be altered most simply by changing the internal contours of that part of the nozzle (an uncooled tungsten extension of the water-cooled copper nozzle) which is actually integral with the outer electrode. This nozzle extension was sized to achieve a jet Mach number of 0.75, an estimated optimum value for maximizing power output when the interrelationship between conductivity and velocity is considered with respect to power density.

The magnet structure employed in the preceeding NAS5-703 contract was modified for the more extensive requirements of the new generator. The principal change was the incorporation of coolant passages, for control of the generator sidewall heat flux, into the magnet pole caps. Measurement of the field intensity produced with the correct generator gap spacing indicated a field intensity of 6,000 gauss at incipient saturation and a maximum deviation of five per cent from the mean field strength throughout the entire generator cavity volume. Fields of 8,000 gauss were obtained at considerably greater coil currents but could be maintained only for short periods (up to one minute) before excessive coil heating occurred. The limitation in field strength is caused primarily by insufficient core area and consequently iron saturation.

Heat transfer in both the axial and radial direction was estimated for the generator with jet total temperatures of 3300°K and static pressures of two atmospheres. The estimate of radial heat transfer through the outer electrode was based on the application of Reynolds analogy of momentum and heat transfer to the momentum loss analysis of Rosengweig⁴. The resulting radial heat transfer was 20 watt cm⁻² for a stainless steel housing temperature of 1000°K. An

electrode temperature of 2600°K results thereby which will permit adequate thermionic emission of at least 1 amp cm⁻² from a tungsten electrode.

Axial heat transfer from the generator sidewalls was estimated, on the basis of the analysis⁵ previously developed for this application, to be approximately 14 watts cm⁻² for a housing temperature of 1000°K. This results in a temperature of 1800°K for the inner surface of a magnesia electrical sidewall insulator and 1700°K at the magnesia-zirconia interface. The latter two temperature levels should be satisfactory, both from the standpoint of negligible sidewall electrical shorting and the liquidus temperature (1750°K) of the magnesia-zirconia binary system.

The combined effects of all heat losses in the generator, but excluding those in the water cooled nozzles, result in a four per cent reduction of the plasma mean static temperature level. This, of course, has its consequences on the plasma conductivity.

The power conversion in the generator was estimated conservatively on the basis of equilibrium plasma conductivity being maintained, allowing for the effects of heat transfer on the static plasma temperature distribution, and considering the effects of turbulence on the velocity distribution. The effective mean conductivity is approximately 1 mho cm⁻¹ under the conditions of pressure, temperature, applied magnetic field of 1 weber m⁻², and a relative cesium seed molar concentration of 0.015. An increase of 15 per cent in conductivity could be expected with a four-fold increase in concentration⁶. The gain, however, is certainly not warranted considering our present purposes and the relatively high cost of cesium.

The deviation from inviscid vortex flow can be judged with reference to Figure 5b of Reference 7 which indicates a measured velocity distribution of a vortex having similar non-dimensional flow and geometry parameters with the exception of having a porous center body. The resulting conservative estimate of power is 880 watts, corresponding to an applied magnetic field of 1 weber m⁻².

A preliminary study of centerbodies for the vortex generator revealed that the desirability of tangential velocity stagnation, as effected completely by a

porous center body, will depend upon the extent to which field induced nonequilibrium can elevate the conductivity in the region of the inner electrode. The best available information regarding nonequilibrium effects⁸ suggested a simple nonstagnating exhaust electrode arrangement of the type illustrated in Figure 3-1 will perform best, in the case of a fairly shallow generator. Thus, the inner electrode arrangement employed was of this type.

3.2 Instrumentation and Test Facility The experimental model of the vortex MHD generator included internal instrumentation and the necessary internal electrical connections to the electrodes. The electrical connections consist of two tantalum strips, each resistance welded to the outer tungsten electrodes and then bolted to the stainless steel generator frame. Difficulties encountered in resistance welding were overcome primarily by cleaning the surfaces to be joined with a hydroxide solution and using well-prepared welding electrodes having a good surface finish to prevent electrode-to-work piece sticking. No intermediate foil was employed as is often the case for joining refractory metals because of the relatively low melting temperatures of the resulting bond. The weldments produced seemed to be structurally adequate although not to the same degree that is possible with non-refractory metals.

The internal instrumentation of the generator include: nozzle upstream static and back pressure ports; radiation shielded $W - W/0.26$ Re thermocouples located on the outer surface of the tungsten electrode ring; C/A thermocouples mounted at the interface of the MgO and ZrO_2 sidewall insulators and also at the interface between the ZrO_2 insulator and soft iron sidewall; C/A thermocouples cemented into the inside surface of the generator frame; and finally $W - W/0.26$ Re thermocouples located in the flanged section of the graphite exhaust tubes and adjacent to the tungsten overlay which forms an electrode surface. With the exception of the latter, all of the thermocouples were located such that radial and azimuthal variations in temperature can be determined as well as the heat flux or thermal conductances of the various insulators. Other thermocouples were installed for purposes of measuring the temperature rise of the air streams which externally cool the generator.

The various gas metering systems required for a generator test were calibrated by a laminar flow meter of 0.5 per cent accuracy. The primary metering elements

are choked nozzles furnished with the necessary temperature and pressure gages. These systems provide the metering and control of primary and secondary (for seed injection) argon flows to the individual arc heaters and nozzles and air cooling flows for the generator sidewalls and periphery.

The control and data recording equipment required for testing the generator is shown in the photograph of the generator test area, Figure 3-4. The nearby power supplies for the arc heaters are not included. Parameters which are indicated and recorded include the generated voltage and current, applied magnetic field, and appropriate generator component temperatures. Data recorders include both high speed and low speed print-out equipment.

A review of possible techniques to measure plasma enthalpy was conducted. For purposes of determining heat transfer coefficients within the vortex generator and also the generator conversion efficiency, a gas-dilution type of calorimeter was indicated. Figure 3-5 shows the gas dilution calorimeter which was constructed. This type of calorimeter was selected in order to obtain a mean stream enthalpy value and also to employ gas dilution as opposed to a water-side heat sink to avoid the possibility of an explosive interaction of a condensed alkali metal and water due to a leak. The operation of the calorimeter is as follows: room temperature nitrogen is supplied to the calorimeter cocurrent with the plasma jet; the three inner tubes shown in the lower part of the picture serve first to direct the unheated nitrogen in a way to protect the calorimeter from direct contact with the high temperature jet and second to thoroughly mix the plasma and nitrogen by two turbulence-producing tantalum screens welded to the center section; finally an array of thermocouples is employed in determining the average temperatures of the resulting gas mixture diluted to a temperature of approximately 1500°F.

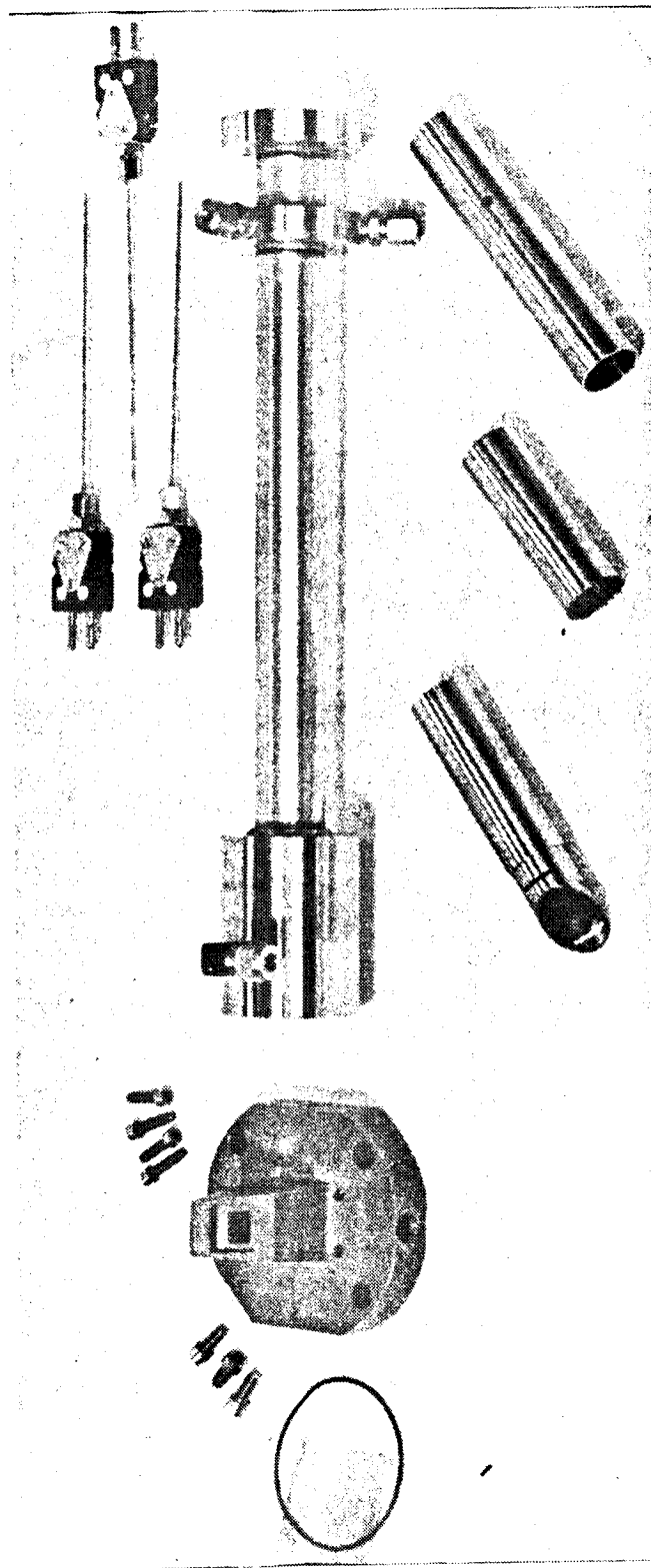
In practice, thermal insulation was placed around the calorimeter shell to improve accuracy in the calorimetric measurements. Also, an exhaust valve, not shown here, can be secured to the end of the calorimeter and make it possible to vary the back pressure - thus providing means of simulating the generator back pressure which the nozzles will experience in generator tests and thereby accurately reproducing the enthalpy of the generator driving jets.



VORTEX MHD GENERATOR TEST FACILITY

895C

FIGURE 3-4



GAS DILUTION CALORIMETER

FIGURE 3-5

A preliminary operational check was performed with the gas dilution calorimeter. Its performance was very satisfactory from the standpoint of both structural capability and thorough mixing of gas streams. A typical result indicated a conversion efficiency of the arc heater and nozzle combination of 63 per cent for an input power of 20 kw. In this case, the mean argon jet temperature of 5300°F was subsequently reduced to 1500°F by dilution of the argon with nitrogen.

3.3 Generator Operating Characteristics and Test Results

3.3.1 Outline of Generator Tests A brief resume of those generator tests which were conducted specifically for the generation of power are indicated in tabular form below:

Table 3-1

Outline of Generator Tests

Test No. 1

Seed:	CsOH
No. of Nozzles:	1
Sidewall Insulator:	MgO
Remarks:	A water cooled arc heater electrode failed prior to seed injection. Resulting leakage of water through the hot generator destroyed the internal ceramic components of the generator.

Test No. 2

Seed:	CsOH
No. of Nozzles:	1
Sidewall Insulator:	MgO
Remarks:	A combination of low plasma conductivity (the gas temperature was reduced by the aqueous seed solution, accidentally supplied at an excessive rate) and ground short on the inner-electrode/exhaust tubes prevented any significant net power conversion. The shorts were caused by deposits of graphite between the exhaust tubes and the magnet iron core. Leakage of gas over the exterior surfaces of the flanged end of the exhaust tubes (which were not protected with a tungsten coating as were the electrode surfaces) and subsequent erosion of the graphite was responsible for the deposits.

Test No. 3

Seed: Cs

No. of Nozzles: 1

Sidewall Insulator: MgO

Remarks: An effort was made to correct the two conditions which led to the reduced power output in the previous test. The seed consisted of cesium metal, replacing the aqueous solution of cesium hydroxide. Thus higher plasma temperatures (and hence conductivity) were achieved at the same cesium to argon mole fraction and argon flow rates. Additional benefits which accrued from the change in seed substance included a fair degree of independence of plasma temperature to seeding rate (in the range of optimum seeding) and a marked reduction in erosion of the refractory metal components of the generator. An attempt to prevent leakage past the exhaust tube flanges by eliminating leakage paths downstream (where the seal problem is less severe due to lower temperatures) was only partially successful. The new seals were effective; however, the graphite exhaust tubes ruptured and thereby provided a new leakage path. Erosion and deposition of graphite occurred subsequently to provide a shorted generator output as in the previous test.

Test No. 4

Seed: Cs

No. of Nozzles: 2

Sidewall Insulator: $\text{SrO} \cdot \text{ZrO}_2$

Remarks: The objectives of this test included the substitution of strontium zirconate for the magnesium oxide sidewall electrical insulators to reduce the volatile loss of insulator material. Two jets were employed to minimize the effects of turbulence in the vortex flow (by an increase in the u/v ratio). And finally more elaborate measures were taken to prevent the type of ground-shortcd generator output which occurred in the two previous runs. These consisted

of adding a tungsten coating to the external surfaces of the graphite exhaust tubes and fastening thin tantalum disks to the rear surfaces of the tube flanges. The disks extended a short radial distance beyond the inner electrode flange and were secured between the zirconia and strontium zirconate sidewalls. Thus the minor gas leakage which had been so instrumental in eroding the exhaust tubes and thereby establishing a ground short was considerably minimized by the new set of seals as well as the ones installed for Test 3.

This test was interrupted by a thermal overload device which shut off one of the two arc heater power supplies because of a high laboratory ambient temperature. The power interruption occurred before achieving the plasma enthalpy required for reasonable conductivity and hence power output. Subsequently, inspection of the graphite exhaust tube revealed that significant erosion and ground shorting there would rule out another test. It was apparent after disassembling the generator that the exhaust tubes were the only components to suffer erosion.

3.3.2 Test Procedures A typical test procedure was programed in the following sequence:

- a) With the generator assembly, installation, and connections completed, the experiment was enclosed under a hood to prevent noxious fumes from contaminating the laboratory.
- b) Instrumentation was allowed to warm up and then calibrated.
- c) Arc heater and generator cooling systems were put into operation.
- d) The generator "warm up" sequence was initiated. It consisted of a gradual increase of argon flow and arc heater power for a two to three minute period to eliminate thermal shock of the ceramic insulators.
- e) All supply conditions were maintained constant while the sidewall shorting resistance was monitored as a function of temperature until the generator achieved thermal equilibrium.

- f) The magnetic field was applied.
- g) Seeding was then initiated, with the rate slowly increased to near optimum, i.e., when the generator output was maximum.
- h) A generator load curve was determined and all other data not automatically recorded were noted.
- i) The seed rate and magnetic field were reduced to zero and the sidewall resistance vs. wall temperature measurement repeated to determine deterioration or other changes in the wall conditions during the preceding steps.
- j) Other test objectives were then attempted.
- k) A shut-down sequence of two to three minutes was then provided to eliminate thermal shock of the ceramic insulators.

The generator was then carefully removed from the electromagnet assembly and disassembled. Attention was given to the condition of the various components in an effort to discover additional information concerning their individual and collective performance.

3.3.3 Mechanical Performance of the Generator The design of the experimental model of the vortex MHD generator appeared to be satisfactory in most respects. Very little development of the model was required during the course of the program. The only significant change required was concerned with the reduction of gas leaking past the exterior surfaces of the exhaust tubes. The inherent flexibility of the model for both geometric changes and material substitutions which was an initial design goal appeared to have been met.

It was unfortunate that assembly time and test preparation was so lengthy as to limit the number of generator tests. However, the generator and instrumentation performance and reliability depended to a great extent upon the careful attention to details. To an extent, this is evidenced by the fact that no damage or deterioration was incurred by the basic structural elements of the generator. Of course, the expendable components, e.g. the electrode assemblies and ceramic sidewalls, suffered deterioration as expected.

A few specific comments regarding the individual components are in order at this point.

Water-cooled nozzles: Some difficulty was anticipated in machining the deep water cooling passages and interior contours of the copper nozzles. However, by the use of electrical discharge machining (EDM) no problems materialized. The nozzles operated satisfactorily, i.e. with no burnout or deterioration during operation at maximum arc heater input power of 60 KW or with secondary argon/seed injection. Water flow and pressure drop in the coolant passages were both moderate under the most severe heat transfer conditions imposed.

Tungsten Nozzle Extension: The tungsten nozzle extensions performed satisfactorily without forced cooling except when water containing seed solutions were used. Erosion then changed significantly the throat dimensions (.500" x .133") within a few minutes. No dimensional changes occurred with the pure cesium seed. The internal contours of these nozzles, consisting of convergent-to-constant area passages of rectangular cross section, were also machined by the EDM process.

Outer-Electrode Assemblies: These assemblies consisted of split tungsten rings (rolled and sintered) to which tantalum electrical lead straps were resistance welded. The tantalum-to-tungsten welds, although a considerable improvement over tungsten-to-tungsten welds, were structurally weak and not extremely reliable. Reliability was improved to the necessary extent by the use of multiple welds, usually six to eight per strap. An occasional crack developed in the tungsten rings but their occurrence was always related to having the heat affected zones of adjacent resistance welds overlaid each other. In no case, however, did loss of electrical continuity to the electrodes occur, and this was the result of employing multiple tantalum straps.

Ceramic Sidewalls: The ceramic sidewalls included two .25" thick electrically-insulating disks adjacent to the plasma vortex flow and two .25" zirconium oxide disks for thermal insulation. The generator geometry is such that material substitutions and changes in total insulator thickness (to a maximum of .5" per side) are easily accommodated. Thus when a replacement for the MgO electrical insulators was indicated, due to severe erosion, strontium zirconate disks, suitably sized with regard to their coefficients of thermal expansion, were employed without requiring dimensional changes in the other generator components. The zirconium oxide disks performed without any evident sign of deterioration.

However, it was necessary to destroy at least one of the pair for disassembly purposes.

Inner-Electrode/Exhaust Tubes: The major component performance problem was presented by the integral inner-electrode/exhaust tubes. As discussed previously, the plasma which leaked out from the vortex cavity and past the outer surfaces of the flanged ends of the tubes eroded the unprotected graphite and subsequently deposited it in a region of lower temperature. These deposits were electrically conducting and shorted the generator output by grounding the normally insulated exhaust tubes to the adjacent magnet iron cores and pole caps. Constructional changes in the last test, reviewed in section 3.3.1, were effective only temporarily in preventing a recurrence of the aforementioned problem. The inability to apply a sound tungsten coating over the entire inner surfaces of the graphite tubes led to premature tube failure. Exhaust tubes made entirely of refractory metals thus appear to be necessary for adequate test periods.

The plasma sprayed tungsten coatings applied to the graphite tubes were successful in adherence to the graphite substrate and were able to prevent erosion in the immediate region of the coating.

Frame: The frame served as a basic support structure for the other generator components and in addition was double walled to provide cooling (air blast cooling) in the region of the outer electrode. The material, 310 series stainless steel, was selected primarily on the basis of its relatively high scaling temperature. Other requirements of the frame, such as gas sealing and the absence of distortion or local melting, were satisfied in all tests.

Generator Internal Instrumentation: The internal instrumentation consisted of pressure and temperature (thermocouple) readouts. Nozzle upstream static pressures were determined by conventional ports located at the extreme upstream end of the copper nozzles. Nozzle downstream (exhaust plane) static pressures were transferred out of the generator by molybdenum tubes (.040" O.D. x .024 i.d.) with ends terminated adjacent to the tungsten nozzle extension in the nozzle exhaust plane.

Thermocouples were located at the outer and inner electrodes, the ceramic interfaces, the inner surface of the soft iron sidecovers, and the inner surface of frame. The location of these thermocouples is indicated in Figure 3-1 by reference to the bracketed numbers.

Numbers 1 and 2 are chromel/alumel couples which were spot welded into small grooves machined into the internal surface of the generator frame in the plane of symmetry. The grooves, as well as copper cement which was applied over the couple hot junctions, served to establish the junctions at the temperatures of the inside surface.

Numbers 3 and 4 are W-W/.26 Re couples resistance-welded to the outer surface of the tungsten electrode in the plane of symmetry. These particular couples were radiation shielded by single strips of tantalum also resistance-welded to the electrode in the vicinity of the couple hot junctions. Welding difficulties were experienced initially with the assembly of these couples, specifically the tungsten-to-tungsten welds at the electrode and at the extension wire connections. The latter problem was overcome by the use of platinum foil interlayers and the former by shaping one of the welder electrodes to encompass almost entirely the tungsten wire of the couple.

Numbers 5 through 10 establish a radial and axial array of temperatures in the assembly of sidewall components. Numbers 5, 6, and 7 are C/A couples located at the interface of the electrical and thermal insulators. These particular couples were prone to failure because of exposure to the plasma, a condition permitted only by prior failure of the electrical insulator. Numbers 8, 9 and 10 are C/A couples fastened to the inside surface of the soft iron sidecover in a manner similar to Numbers 1 and 2.

The inner electrodes contain W-W/.26 Re couples, Numbers 11 and 12, which were cemented by a magnesium oxide compound into the graphite flanges of the exhaust tubes just beneath the tungsten layer/electrode surface.

External Cooling Systems: In addition to the copper-nozzle cooling which has been discussed already, the generator is provided with four separately controlled air blast cooling systems. Two are located internally for control of radial and electrode heat transfer; the other two control the axial flow of heat from

the generator. In the latter systems, air is forced to flow radially outward over the soft iron sidecovers and is confined to spaces of .040 inch axial depth per side between the sidecovers and the magnet pole caps. The depths of these passages are maintained by very narrow radial ribs on the surfaces of the pole caps.

3.3.4 Materials Performance The performance of materials in the generator tests are summarized in Table 3-2. Erosion, including chemical attack and volatilization was the primary mode of failure in some cases, as suggested by the discussion of Section 4.2. Tungsten was very rapidly degraded in the presence of water vapor supplied with the cesium hydroxide seed solutions. Magnesium oxide volatilized quite rapidly at the high temperatures of generator operation. The graphite was readily attacked by both of the seed substances employed.

In the presence of a cesium seeded argon plasma, both the tungsten components and the strontium zirconate electrical insulators appeared to have withstood erosion effects. The strontium zirconate did exhibit radial cracks which were contained so well however that the functional performance of the insulators was not diminished. Radial cracks have been a general characteristic of almost all of the ceramic sidewalls employed in the generator tests. These cracks most likely have been due to excessive thermally induced stresses. Both steady-state and transient thermal stresses have been evaluated for the conditions of the laboratory operation of the generator. The stress analysis for asymmetrical plate cooling and for radial temperature gradients are described below. It appears that excessive radial temperature gradients were responsible for the radial cracks.

The maximum allowable temperature difference between the plasma and sidewall can be estimated on the basis of the following relation for asymmetrical sidewall cooling.

Table 3-2
Materials Performance in Generator Tests

Test No.	Tungsten Nozzle Extension (s)	Outer Electrode Assemblies	Electrical Insulator	Thermal Insulator	Inner Electrode Assemblies	Internal Thermocouples
Erosion (and chemical interaction)						
1	None - no seed.	Very slight. Possible reaction with adjacent MgO.	MgO: Extreme erosion in vicinity of outer electrode.	ZrO ₂ : No deterioration.	No deterioration.	Welded connections were susceptible to mechanical failure. MgO/ZrO ₂ interface couples were destroyed due to failure of MgO insulator.
2	Very extensive after 6 minute exposure to CsOH seed.	Slight with tungsten. Tantalum had recrystallized and undergone extensive erosion in some regions.	MgO: Slight erosion due to low average plasma temperature.	ZrO ₂ : No deterioration.	No tungsten erosion. Extensive graphite erosion at flange end.	MgO/ZrO ₂ interface couples were destroyed due to failure of MgO insulator. W - W/.26 Re couples were susceptible both to weld failure and loss of continuity due to erosion (in the case of CsOH seed).
3	None after 6 minute exposure to Cs seed.	None.	MgO: Extreme erosion in vicinity of outer electrode.	ZrO ₂ : Slight erosion due to failure of MgO insulator.	No tungsten erosion. Extensive graphite erosion at flange end and tube failure due to Cs attack.	MgO/ZrO ₂ interface couples were destroyed due to failure of MgO insulator. W - W/.26 Re couples were susceptible both to weld failure and loss of continuity due to erosion (in the case of CsOH seed).
4	None after 6 minute exposure to Cs seed.	None.	SrO·ZrO ₂ : Thermal stress cracks. No erosion.	ZrO ₂ : No deterioration.	Extensive erosion of graphite, including cathode substrate.	Electrode and ceramic sidewall interface couples were omitted to expedite generator assembly. No deterioration of remaining couples occurred.
Thermal Stress						
1	None noted.	None noted.	Severe failure enhanced by erosion damage.	None noted.	None noted.	Weld failures were possibly due to thermal stress.
2	None noted.	None noted except for weld induced crack.	Stress cracks were present but all sections were very well contained.	None noted.	None noted.	Weld failures were possibly due to thermal stress.
3	None noted.	None noted except for weld induced crack.	Extreme failure.	None noted.	None noted.	Weld failures were possibly due to thermal stress.
4.	None noted	None noted.	Stress cracks were present but all sections were very well contained.	None noted.	None noted.	None.
Electrical Resistivity						
	-	-	MgO [†] : $\rho = .01 e^{27,200/T}$ in ohm cm	-	-	-
			SrO·ZrO ₂ ^{††} : $\rho = 0.316 e^{17,500/T}$			
Thermal Conductivity			MgO [†] : $k = .02 \text{ cal sec}^{-1} \text{ cm}^{-1} / ^\circ\text{C}$ at T = 1500°K	$k^\ddagger = 0.028 \text{ cal sec}^{-1} \text{ cm}^{-1} / ^\circ\text{C}$ (mean value over the temperature range 2000°F to 4500°F)	-	-
			SrO·ZrO ₂ : information not available			

[†] Based on correlation with the general law for resistivity of semiconductors, $\rho = Ae^{B/KT}$. Coefficients based on Reference 9.

^{††} Coefficients given are those for an analogous compound CaO·ZrO₂.

[‡] Data based on Zirconium Corp. of America information.

$$\Delta T_{\max} = \frac{S(1-\nu)}{\alpha E} \left(1.5 + \frac{9.6k}{bh} \right) = 1.5R + \frac{2.48R'}{bh} \quad (\text{Reference 10})$$

where S = stress

ν = Poisson ratio

α = coefficient of expansion

E = modulus of elasticity

k = coefficient of thermal conductivity

b = plate thickness

h = heat transfer film coefficient

The property values of ThO_2 are assumed since it is known to be more shock sensitive than either MgO or $\text{SrO} \cdot \text{ZrO}_2$ and the property values of the strontium zirconate are not yet completely determined. Thus for ThO_2 at 1000°C the values of R and R' are 70°C and $0.5 \text{ cal sec}^{-1} \text{ cm}^{-1}/^\circ\text{C}$ respectively (Reference 10) and the values of $b = 0.63 \text{ cm}$ and $h = 10^{-2} \text{ watt sec}^{-1} \text{ cm}^{-2}/^\circ\text{C}$ representative of the generator experiments indicate a $\Delta T_{\max} = 980^\circ\text{C}$. Hence generator cooling and heating rates (heating may be shown to be a less severe condition) were controlled so that the plasma temperature and the time dependent temperature of the ceramic sidewall did not provide a difference in excess of the maximum allowable. This resulted in generator startup and shut down periods of approximately three minutes each and surface spalling of the ceramics was avoided entirely.

The possible existence of substantial stresses due to radial temperature gradients in the ceramic sidewalls was revealed by inspection of the two-dimensional stress relations for a disc (Reference 11):

$$\sigma_r = -\alpha E \cdot \frac{1}{r^2} \int_r^a T_r dr + \frac{E}{1-\nu^2} \left[C_1 (1+\nu) - C_2 (1-\nu) \frac{1}{r^2} \right]$$

$$\sigma_\theta = \alpha E \cdot \frac{1}{r^2} \int_a^r T_r dr - \alpha E T + \frac{E}{1-\nu^2} \left[C_1 (1+\nu) + C_2 (1-\nu) \frac{1}{r^2} \right]$$

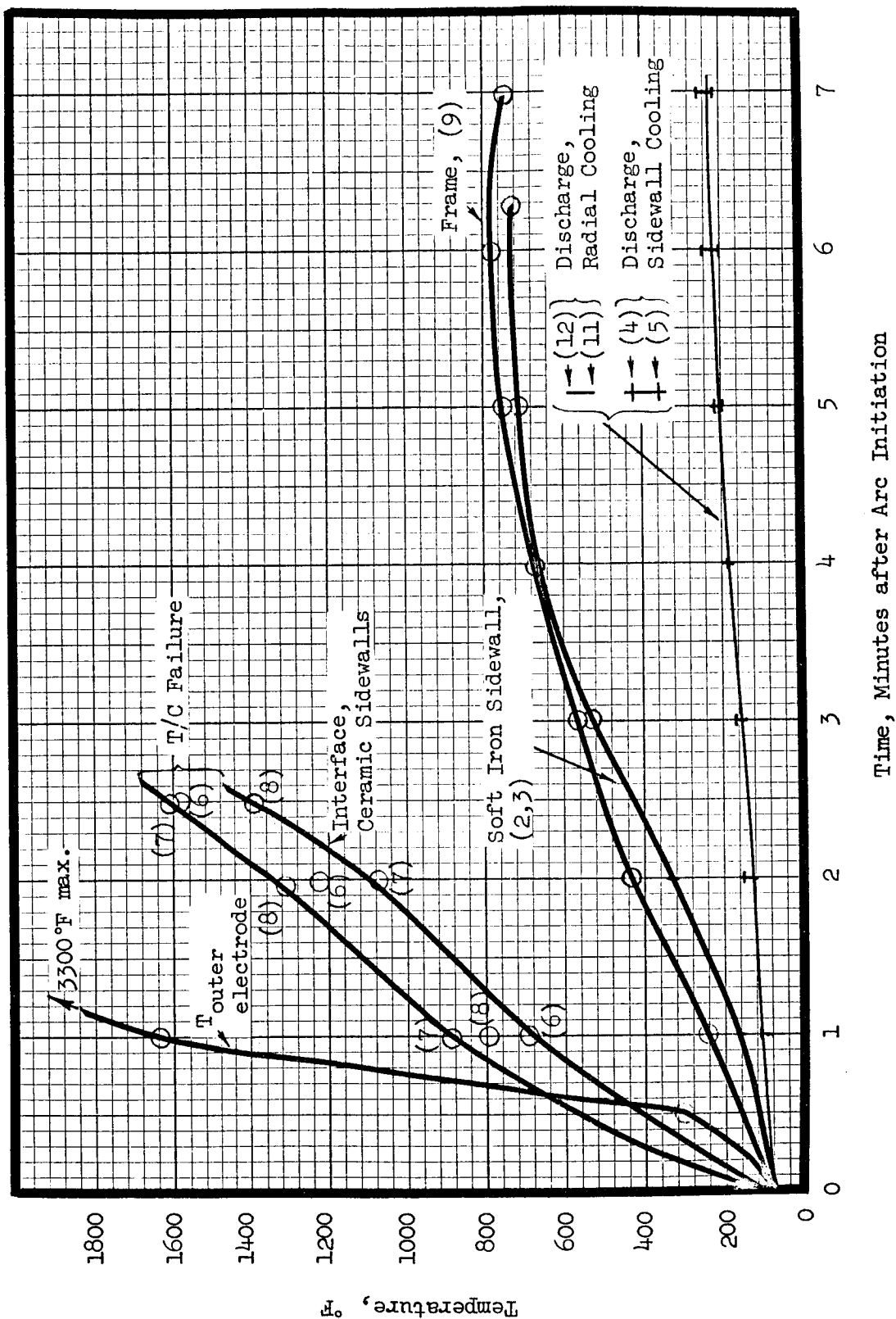
where C_1 and C_2 are integration constants determined by the appropriate boundary conditions. The most severe stress condition appeared to be an azimuthal

component of tensile stress at the disc inner radius. Assuming that the radial temperature gradient of the generator ceramic sidewall was a linear function of radius and approximately equal to 100 C°/cm, and property values for MgO at 2300°F ($\alpha = 7.7 \times 10^{-6}/^{\circ}\text{F}$, $E = 4 \times 10^6$, Reference 12), we find the calculated stress to equal the tensile strength, 6000 psi, of MgO. This type of stress failure thus offers a reasonable explanation for the existence of the ceramic sidewall radial cracks mentioned previously.

3.3.5 Heat Transfer and Thermal Distribution The limited scope of the experimental phase of the generator study imposed severe restrictions with respect to the correlation of component performance and analysis. At best, therefore, the tests can give only a crude comparison between actual performance and theory. Since a wide discrepancy between theory and performance can be attributed to many unknowns, such as the actual heat transfer film coefficient and thermal conduction coefficients of the ceramic sidewalls, a good correlation between theory and tests for a few test points does not necessarily imply that the theory is adequate. A considerably more extensive approach would be necessary. The use of thermocouples both at the interface of the ceramic sidewalls and at the interior surfaces of the generator frame and soft iron sidewalls were intended to improve the accuracy of correlation. However, failure of the interface thermocouples (or their extension wire connections) prior to the establishment of thermal equilibrium conditions permits only a crude comparison of the measured and predicted heat transfer rates. Nevertheless this comparison will be discussed; it will be based on the data from Test No. 3 for which the thermal data is most complete.

The temperature-time profile of this test is illustrated in Figure 3-6 and other data is included in Table 3-3.

By application of the heat transfer design equations, described in Section 3.1, to the analysis of conditions in the region of the outer electrode, one finds a mean thermal conductivity of 0.023 watt/cm °C for the zirconia powder insulation between the outer electrode and generator frame. This is compared with the value of 0.013 watt/cm °C originally assumed on the basis that its thermal conductivity would be approximately that of the solid high density forms of zirconia. The nature of this particular grade of zirconia is such that a value of conductivity approaching the larger of the two values above could well be expected if the



Temperature-Time Profile of Test No. 3 Figure 3-6

density of packing did not approach that of the high density (350 lb/ft³) solid zirconia.

Table 3-3
Data-Test No. 3
(at Thermal Equilibrium)

$W_{\text{argon}} = 12.9 \text{ gm sec}^{-1}$	$T_{\text{electrode - outer}} = 3300^{\circ}\text{F} (2100^{\circ}\text{K})$
$P (\text{Cs}) = 0.0185$	$T_{\text{electrode - inner}} = 2900^{\circ}\text{F} (1870^{\circ}\text{K})$
Arc Jet Power = 38 kw	$T_{\text{cylindrical frame}} = 789^{\circ}\text{F} (690^{\circ}\text{K})$
$p_o^o = 30 \text{ psig}$	$T_{\text{soft iron sidewall}} = 800^{\circ}\text{F} (700^{\circ}\text{K})$
$p_o = 16 \text{ psig}$	

Air Blast Cooling:

	W_{air} (gm sec ⁻¹)	Temperature Rise (°F)	Heat Transfer (kw)
Left side	27	160	2.41
Right side	27	130	1.96
First half radial cooling	8.6	120	.576
Second half radial cooling	8.6	155	.745

The adiabatic wall temperature, in the absence of direct calorimetric measurements, must be inferred from the measured electrode temperature and the heat transfer film coefficient analysis. At a film coefficient, estimated to be 0.0302 watt/cm² C°, the adiabatic wall temperature is 3190°K. This value can be employed next in a calculation for sidewall heat transfer. Under the conditions of test, the calculated mean film coefficient at the sidewalls is 0.0156 watt/cm² C°. Assuming a mean thermal conductivity of 0.013 and 0.0755 watt cm/°C for MgO and ZrO₂ respectively, the calculated total heat transfer to the soft iron sidewalls at 700°K is 2.47 kw. The measured value of 4.37 kw is thus substantially greater. If the thermal conductivity of ZrO₂ is actually closer to the 0.023 watt cm/°C value indicated for the powder form, then the calculated total sidewall heat transfer is 2.99 kw. The remaining discrepancy is considered to be primarily due to an underestimation of the gas film coefficient.

The most important requirements for better heat transfer prediction are thus seen to be the need for additional knowledge of the property values of the thermal insulation (zirconia) and improvements in the analysis of the gas film coefficient.

3.3.6 Thermodynamic Performance The most disappointing aspect of the generator tests was the inability of the two tests (Nos. 2 and 3) not aborted by commercial equipment failures to produce a significant net power output. Measurements of the generator internal impedance during these tests explain this situation, however. The value of interelectrode resistance was approximately 40 ohms when the generator achieved its operating temperature but before the injection of seed material. During the course of establishing the desired seed flow rate, the graphite exhaust tubes were eroded by the seeded argon at an extremely rapid rate and subsequently graphite deposits were built up between the tubes and the magnet core. This action provided a very effective internal shorting impedance of approximately 0.01 ohm which shunted the actual generator output. The magnitude of this impedance was so small with respect to the impedance of the plasma in the vortex cavity that an analysis of the magnetohydrodynamic performance of the generator was impractical.

The generator tests were also intended to provide a check on the possibility of magnetic damping of turbulence. This phenomenon was also obscured by the condition of shorting since the open circuit vortex pressure distribution must be analyzed to determine the extent of magnetic damping. The extent of this effect however was expected to be very small. To show this, note that the ratio of the dissipation due to eddy currents to the dissipation due to viscosity, as derived in Reference 13, is given by

$$D_j/D_\mu = O(2.5 \times 10^{-5} \sigma B^2 L/\mu).$$

Thus not until the Hartmann number based on the effective shearing length ($\approx L$) of the generator approaches the order of 200, would one expect that the turbulence would begin to differ markedly from its usual form. Under the conditions of the present tests with $\sigma = 40$ mhos/m, $\mu = 8 \times 10^{-5}$ newton sec./m², and $B = 0.6$ weber/m², this departure from ordinary turbulence takes place when the effective depth of the vortex cavity becomes of the order of 3 cm, about twice the depth of the present generator.

3.3.7 Hall Effects and Nonequilibrium Ionization Vortex MHD generators may be constrained so as to minimize the degrading Hall effects. The generalized Ohm's law as applied to the vortex generator shows that the flow direction and the magnetic field can be oriented relative to one another in such a way that the Hall potential due to the tangential velocity can actually be used to reduce the azimuthal "ring" currents, while the Hall potential due to the radial velocity can be made to enhance the radial flow of current. Thus the usual reduction in effective conductivity due to Hall effects can be minimized. To explain this, consider the expression for radial and azimuthal current:

$$j_r = \frac{\sigma}{1 + (\omega\tau)^2} \left[E_r + vB + (\omega\tau) u |B| \right] \quad (1)$$

$$j_\theta = \frac{\sigma}{1 + (\omega\tau)^2} \left[-uB + (\omega\tau)(E_r + vB) \frac{B}{|B|} \right] \quad (2)$$

If, for example, the azimuthal current can be made to vanish by imposing the condition

$$uB = (\omega\tau)(E_r + vB) \quad (3)$$

then the expression for radial current becomes simply

$$j_r = \sigma(E_r + vB) \quad (4)$$

without the usual reduction in effective conductivity at significant $(\omega\tau)$ typical of linear MHD generators with continuous electrodes.

The above condition (Equation 3) may also be written in the form

$$u/v = (\omega\tau)(1 - K) \quad (5)$$

where $K \equiv -E_r/vB$ is the local generator coefficient. This condition, as well as the expression for power density in the MHD generator, namely

$$P/V = \sigma_{\text{eff.}} (vB)^2 (1 - K)K$$

must be considered with respect to the overall generator performance. It is instructive therefore to determine what maximum value of $(\omega\tau)$ can be effectively

utilized by the vortex MHD generator for probable ranges of u/v and K . The ratio u/v must be large enough to reduce the effects of turbulence and yet not contribute significantly to the loss of kinetic energy due to the radial velocity. This range is of the order of 10^{-2} to $1/3$ where the latter corresponds to a ten per cent loss of kinetic energy. The range of K will be from 0.5 for an open cycle application of short duration (where the fuel weight is a relatively small part of the total system weight) to 0.95 for an application in which generator conversion efficiency is a determining factor.

For example then if we let $u/v = 1/3$ and $K = 0.8$, a value of $\omega\tau = \frac{u/v}{1-K} = 1.7$ may be employed with complete cancellation of all azimuthal currents. Were it not for the suppression of azimuthal Hall current by the normal "ring" current produced by the radial component of velocity, the generator power density would be reduced by $\left(1 - \frac{1}{1 + (\omega\tau)^2}\right) 100\% = 74.5\%$.

This mode of operation (which satisfies the condition of Equation 3) also requires that the radial mass and current flow directions must be identical. Thus the electrode adjacent to the exhaust gases serves as a cathode or electron emitter. Since this is the cooler of the two electrodes, thermionic emission limitations must be given consideration if sheath losses due to field-induced emission are to be avoided.

It is quite likely that thermionic emission from tungsten, which has field-free vacuum emission of 14.2 a/cm^2 at 3000°K and 233 a/cm^2 at 3500°K , will be adequate for open cycle generator applications. Enhanced emission rates, due to adsorbed cesium atoms on the tungsten surface, does not appear to offer much improvement compared with the vacuum emission rates because of the rapid boil off of the cesium surface film at high tungsten temperature. Even at lower surface temperatures, the cesium flux rates corresponding to the conditions of the present experiment or the example of Section 6.3 (typically 6×10^{18} and $1.3 \times 10^{20} \text{ atoms sec}^{-1} \text{ cm}^{-2}$ respectively) are insufficient to provide emission exceeding a calculated 4 a/cm^2 , based on the analysis and experiments of Reference 14.

The results of the present generator tests do not permit an adequate test of the Hall effect or cathode emission analysis above. However, the example of computer calculated power output, Table 6-2, does indicate the very strong improvement in power density which results when the direction of radial current and flow are properly oriented.

Operation in the regime of high $\omega\tau$ is not necessarily an objective with combustion plasmas inasmuch as they are unlikely to produce significant electron heating and consequently non-thermal ionization. Monatomic gas plasmas on the other hand do not exhibit the characteristically high electron collision energy loss factors of combustion plasmas and, therefore, may prove suitable for closed cycle power generation at moderate temperature levels. However, the large values of $\omega\tau$ required for substantial electron heating,¹⁵ on the order of four or more, would require excessive u/v ratios in a vortex generator unless load coefficients of approximately $K = 0.9$ or more are acceptable. It remains to be seen whether the intrinsically high generator efficiency and low power density associated with such values of K can be justified for long term power applications. It is also unclear whether a segmented electrode linear MHD channel which is theoretically capable of complete Hall current suppression could operate effectively, i.e., without eddy current losses due to non-uniform flow,¹⁶ at very high $\omega\tau$ values.

Electron heating could not be expected to be significant in the present generator tests which employed monatomic plasmas, even assuming that the plasmas were completely free from contamination. The ratio of electron temperature to neutral gas particle temperature can be estimated on the basis of the following equation (Equation 9 of Reference 15):

$$\frac{T_e}{T} = 1 + \frac{1}{3} (1 - K)^2 \frac{(\omega\tau)^2}{1 + (\omega\tau)^2} \frac{M^2}{\delta^2} \quad (6)$$

where δ = mean electron loss factor =
$$\frac{\sum_i \chi_i n_i \sum_i \left(\frac{\chi_i Q_{ei} \delta_i}{n_i} \right)}{\sum_i \chi_i Q_{ei}}$$

$\delta_i \approx 10^0$ for monatomic molecules, $\sim 10^1$ to 10^3 for diatomic and polyatomic molecules, a correction factor which accounts for possible inelastic collisions, deviations from a Maxwellian distribution, and a non-constant collision frequency.

χ_i = mole fraction of i-th species.

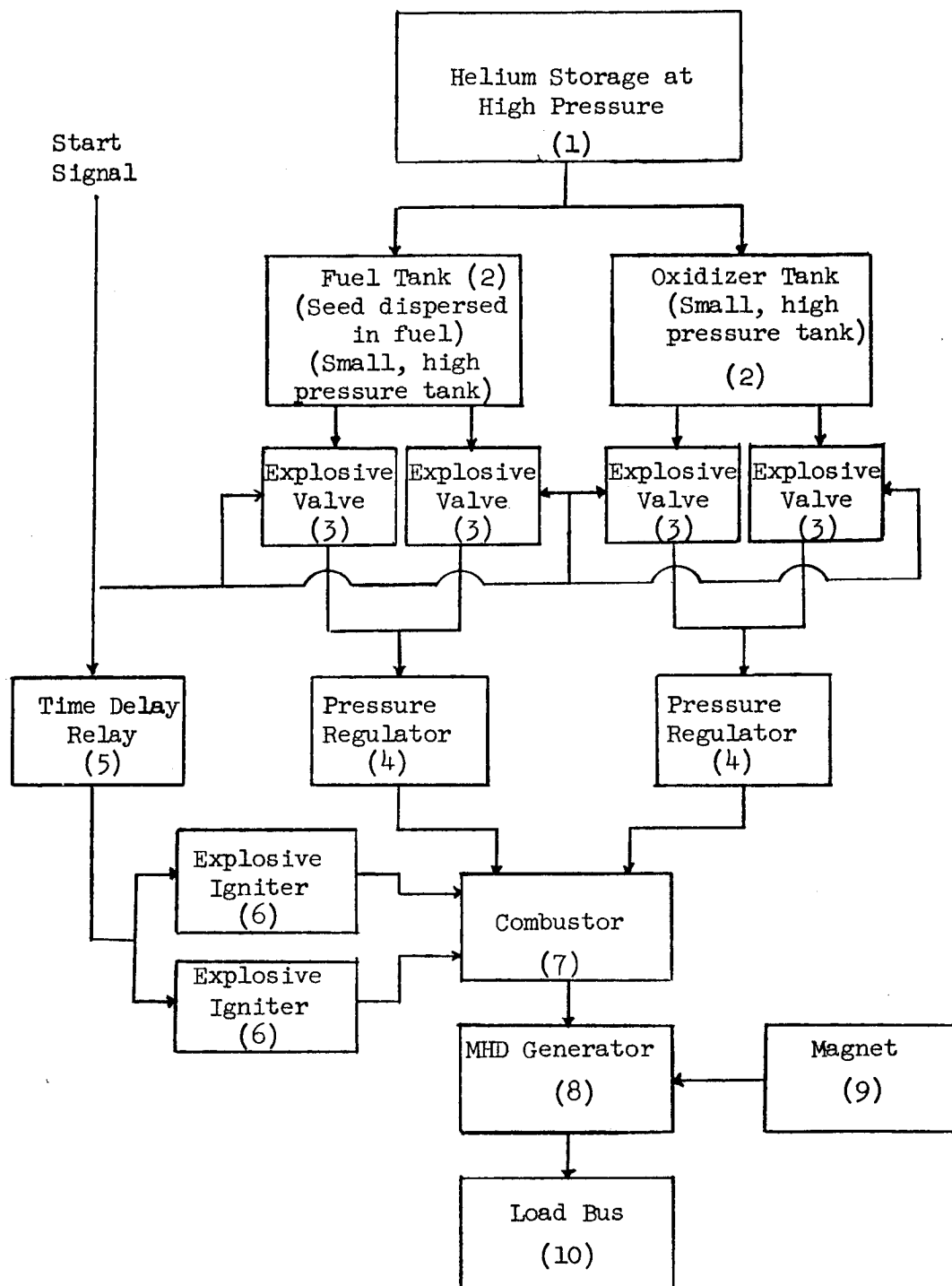
Thus the maximum value of the electron temperature elevation expected in the present tests was only four per cent, calculated on the basis of $\omega\tau = 0.5$, $K = 0.5$, $M = 0.9$, $\gamma = 5/3$, and $\delta = 0.52$.

4.0 INVESTIGATION OF VORTEX GENERATOR SYSTEM RELIABILITY AND MATERIALS LIFETIME

4.1 Vortex MHD Generator System Reliability A first attempt has been made at estimating the anticipated reliability of an open cycle MHD space power system. Unfortunately this task is not as straightforward as the prediction of reliability for electronic systems, for which a wealth of data is available on failure rates in terms of component electrical loading, ambient temperature, etc. Caution and judgment must be used in the case of an MHD power system since the corresponding failure-rate data of critical components is not available simply because a sufficiently large number of such devices have not been tested to warrant the tabulation of the requisite data.

The approach to the problem has been simply to use the available failure rate data for "non-MHD" system components (e.g., fuel tanks, valves, regulators, etc.) and to treat separately those system components which are of an "MHD nature". These latter components have been considered by estimating their "wear out" time, based on erosion rate and evaporative loss calculations. Under the assumption that the shortest wear out time is the limiting factor for the MHD power system (that is, the most rapidly degrading component defines an upper limit to the duration of power), one may attempt to calculate the total system reliability for a mission of duration substantially less than this wear out time. In this approach one essentially acknowledges the fact that at some time the MHD system will no longer produce power or will produce power below an acceptable output level, but assumes that the high temperature MHD components will degrade (or "fail") at a predictable rate, rather than because of random or chance failures.

An example will serve to illustrate the method. Consider the simplified MHD space power system shown in Figure 4-1. Failure rate data is available for all the components shown except, of course, for component 8, the MHD generator. Reliability data for conventional insulators show such low failure rates that their minute effect will be neglected in the following computation. The insulators will instead be considered to be "MHD components" subject to wear-out rather than to chance failure. The only redundancy postulated is in components 3 and 6, the explosive valves and igniters, respectively, which is justified because of their relatively light weight. We assume that the system is designed



MHD Power System Schematic

Figure 4-1

to run until the entire fuel inventory is expended, which will arbitrarily be taken to be one hour. Table 4-1 lists the mean generic failure rates; also listed is a factor GF_r^* which included the redundancy in the explosive-actuated devices. The reliability calculation assumes a dormancy-type power mission such that electrical power is required in a vehicle some time after orbit has been established; the effects of launch and orbital dormancy are neglected. In principle the launch and "waiting" reliabilities could be calculated, but since the power system is inoperative during these phases, these reliabilities may be expected to be relatively high.

The computation proceeds by assuming an application factor, K_A , equal to unity for all components, and an operating mode factor, K_{Op} , of two, corresponding to orbital operation. Where two of the same component are employed, this is included in the calculation of the component adjusted failure rate, F_r . The system mean-time-to-failure t_s is next calculated ($t_s = 10^6 / \sum F_r$) and finally the system reliability, $R_s = e^{-t/t_s}$ (exclusive of the generator itself) for a one hour mission.

The resulting "reliability" level could be raised even further by using the lower extreme values of available failure rate data. This would be an interesting exercise at best, and would have little practical significance. The calculation carried through above yields an interesting reliability, but at an undefined confidence level. In essence the result obtained indicates that the incorporation of an MHD converter into a space power system should not introduce any a priori obstacles to reliability, as far as the accessory systems are concerned.

Still to be resolved, however, is the matter of the "wear out time" of the MHD converter itself. This determination is no routine task, since the time for appreciable component degradation depends upon such a variety of factors including operating temperature, degree of generator cooling (efficiency), specific propellants selected, etc., all of which in turn directly influence the choice of materials for use in the MHD converter. Ideally, of course, the wear out time determination should be the result of experimental testing, indeed of a number of consistent test results so that a confidence level can be defined. This effort appears premature at present, however, in that the current state of the art is such that basic exploratory work is still required with a variety of propellant and materials combinations. Furthermore, contractual efforts with the vortex geometry were of a somewhat more fundamental nature and sought to

Table 4-1

Reliability Parameters

Component

No.	Name	GFr (Mean) (10 ⁶ hr) ⁻¹	Ref.	GFr* (10 ⁶ hr) ⁻¹	K _A	K _{op}	N	Fr (10 ⁶ hr) ⁻¹
1	Helium Storage Tank	0.07	1	0.07	1	2	1	0.14
2	Tank, Small, High Pressure	0.08	1	0.08	1	2	2	0.32
3	Explosive Valve	1 in 10 ⁴	2	"0.01"	1	2	2	0.04
4	Pressure Regulator	2.14	1	2.14	1	2	2	8.56
5	Relay, Time Delay	0.39/cs	1	0.39 [†]	1	2	1	0.78
6	Explosive Igniter	1 in 10 ⁴	2	"0.01"	1	2	2	0.04
7	Combustor	1.78	3	1.78	1	2	1	3.56
8	MHD Converter	-	-	-	-	-	-	-
9	Magnet	5.65	1	5.65	1	2	1	11.30
10	Wire Termination, Between Equipment	0.05	1	0.05	1	2	1	0.10

$$\Sigma Fr = 24.84$$

$$Fr = GFr^* K_{op} K_A N$$

$$t_s = 10^6 / 24.84$$

$$t_s = 10^6 / \Sigma Fr$$

$$R_s = 1 - \frac{t}{t_s} = 1 - \frac{24.84}{10^6} = 1 - (24.84 \times 10^6)$$

$$R_s = e^{-t/t_s}$$

$$= \frac{1.00000000}{0.99997514}$$

† one contact set

establish the performance characteristics of the vortex conversion concept. To this end the experimentation reported used arc-heated argon to power the vortex prototypes which resulted in an experimentally convenient input-energy source whose mass flow, velocity, and temperature could be varied as required. The experimental determination of the wear out time, employing fuels which might logically be used in an open-cycle system, thus was deferred.

Wear out time estimates, for the present at least, must be the result of less direct efforts. One may employ erosion rate data from a variety of sources, including MHD experimentation, rocket nozzle data, etc. or one may attempt to compute the erosion rates of potentially attractive materials under several conditions. An attempt has been made to estimate the wear out time of several critical components in an MHD power generator. The results are given in the following subsection.

The reliability calculation carried through for the MHD space power system concerned only the accessory system components and not the MHD converter itself. The computation tacitly assumed that the components considered were subject to chance or random failure and that an exponential failure distribution consequently applied. Since the MHD converter components, specifically the electrodes and insulators, are subject to wear out rather than to chance failure, the same methods of computing their reliability cannot be generally employed, even if the wear out times are known, since the same failure distribution does not apply. The calculation of the reliability of an MHD converter would require a more sophisticated approach. The applicable distribution (presumably either normal or Lognormal) would have to be determined before the computation could be made. This level of reliability analysis was considered to be beyond the scope of the present effort and somewhat premature, in view of the availability only of calculated wear out times unsupported experimentally.

4.2 Vortex Generator Materials Lifetime The erosion degradation of critical components of an open cycle MHD power generator may occur in any or all of three ways: thermal, chemical, or mechanical. The first of these, thermal erosion, refers to the melting or sublimation of electrodes and insulators. This mechanism may essentially be eliminated by the selection of materials with sufficiently high melting or sublimation temperatures and the operation of these

materials at temperatures such that these processes are minimized resorting to component cooling, if necessary.

The second mechanism, chemical erosion, usually implies oxidation of components but in a more general sense refers to all the possible chemical reactions which may take place at high temperature between the reaction products of the seeded combustion gas and the generator components. The last effect, caused by the erosive or abrasive action of the high velocity gas particles, constitutes what may be termed mechanical erosion. There would appear to be no completely satisfactory theory by which the extent of this type of material degradation can be computed; in most cases the approach has been experimental. Erosive mass loss has been measured for rocket nozzles of various materials for a variety of propellants. Unfortunately this type of experimentation does not allow the separate determination of thermal, chemical, or mechanical erosion; only the gross combined effect is measured.

The following study will be concerned primarily with the action of chemical erosion upon the electrodes and electrical insulators of an open-cycle MHD generator driven with a cesium-seeded cyanogen-oxygen combustion process. However, the approach is general and may be applied to other working fluids. The approach will be to estimate the magnitude of the controlling chemical reactions and thus to attempt an approximation of component lifetimes. The mechanical erosion effect will not be considered as such, but a mass transfer rate will be calculated and compared with the results obtained assuming vacuum evaporation. This mass transfer coefficient will include many of the properties of the high velocity plasma stream. It is felt that this mass loss mechanism constitutes a more realistic model for estimating component erosion rates than is afforded by the assumption of vacuum evaporation.

Electrode Erosion The degradation of electrodes for an open cycle MHD power generator will be considered first. For sufficient thermionic emission for the generator power range under consideration, electron current density capabilities ranging from about 1 to 100 amperes/cm² are required. These high values of current density in turn necessitate high temperature operation of the electron emitter. Tungsten has therefore been selected as a first choice for an electrode material, providing in excess of one ampere/cm² at 2700°K to more than 100 amperes/cm² at 3400°K. These values are for pure (undoped) tungsten

electrodes under conditions of vacuum emission; experimental evidence indicates that even higher current densities may be expected under conditions likely to be found in practical generators.

Operation of tungsten electrodes at temperatures of 2500°K and higher results in sufficient tungsten vapor pressure so that some electrode mass will be lost by evaporation. The loss rate by this mechanism is a strong function of the electrode temperature and whether the effect will become critical will depend upon the particular loss rate and the electrode lifetime required.

A first approach to this problem is to calculate the evaporative mass loss of tungsten electrodes on the basis of evaporation into vacuum. This has been done before (4) and the results are repeated here for purposes of completeness and comparison. Table 4-2 shows some of the characteristics of tungsten electrodes at several temperatures in the range of interest. The mass loss rates were calculated from the equation

$$m = p \sqrt{\frac{m}{2\pi RT}} \quad , \quad (1)$$

where m is the mass loss ($\text{gm}/\text{cm}^2 \text{ sec}$)

p is the vapor pressure (dyne/cm^2)

R is the gas constant ($\text{ergs}/\text{mole } ^\circ\text{C}$)

m is the molecular weight (of the evaporating material)

T is the absolute temperature ($^\circ\text{K}$)

Also shown are the calculated surface depletion rates ($m \times \text{time}/\text{tungsten density}$) in mm eroded per 100 hours.

Table 4-2

Characteristics of Tungsten Electrodes

Temperature ($^\circ\text{K}$)	Thermionic Vacuum Emission Current Density ($\text{amperes}/\text{cm}^2$) (Ref. 5)	Vapor Pressure (dynes/cm^2) (Ref. 5)	Vacuum Evaporation Rate ($\text{gm}/\text{cm}^2 \text{ sec}$)	Surface Depletion Rate ($\text{mm}/100 \text{ hours}$)
2500	0.3	1.33×10^{-4}	1.58×10^{-9}	2.94×10^{-4}
2750	2.5	5.35×10^{-3}	6.06×10^{-8}	1.13×10^{-2}
3000	14.0	1.33×10^{-1}	1.44×10^{-6}	2.68×10^{-1}
3250	63.0	1.33	1.39×10^{-5}	2.59
3500	233.0	12.0	1.20×10^{-4}	22.3

The calculation of electrode mass loss on the basis of vacuum evaporation is only one approach to the problem. So-called "similarity relations for mass transfer" (6) were employed next to calculate the loss rate of tungsten electrodes as tungsten diffused into the plasma stream. The following plasma characteristics were assumed:

$$\text{Viscosity: } \mu = 1.25 \times 10^{-3} \text{ gm/cm sec.}$$

$$\text{Density: } \rho = 7.22 \times 10^{-5} \text{ gm/cm}^3$$

$$\text{Velocity: } u = 9.55 \times 10^4 \text{ cm/sec.}$$

$$\text{Thermal Conductivity: } k = 1.985 \times 10^4 \text{ ergs/cm sec } ^\circ\text{K}$$

$$\text{Prandtl Number: } Pr = 0.83$$

$$\text{Temperature: } T = 4020^\circ\text{K}$$

$$\text{Heat Capacity: } c_p = 5.09 \times 10^8 \text{ ergs/mole } ^\circ\text{K}$$

$$\text{Molecular Weight: } m = 38.5 \text{ gm/mole}$$

The Reynolds number was calculated for flow over the length of an electrode of 5 cm radius ($l = 2\pi r = 10\pi \text{ cm}$):

$$Re = \frac{\rho u l}{\mu} = 173,000$$

Laminar flow was consequently assumed. The average mass transfer coefficient h_D was calculated from the Lewis relation,

$$h_D = \frac{h}{c_p} = \frac{1}{c_p} \left(Nu \frac{k}{l} \right) \quad (2)$$

where $Nu = 0.664 (Pr)^{1/3} (Re)^{1/2}$,

h is the film heat transfer coefficient

c_p' is the heat capacity per unit volume at constant pressure.

For the present case $Pr = 0.83$ and $(Pr)^{1/3} = 0.939$; for $Re = 173,000$, $(Re)^{1/2} = 416$, so that

$$Nu = (0.664)(0.939)(416) = 259$$

Consequently $h = Nu (k/l) = 16.35 \times 10^4 \text{ ergs/cm}^2 \text{ sec } ^\circ\text{K}$ and

$$h_D = \frac{h}{c_p} = \frac{h}{c_p \rho} = 171 \text{ cm/sec.}$$

Having calculated an average mass transfer coefficient, the tungsten mass loss may be determined from the relation

$$m = \frac{\lambda_D}{RT_w} \Delta p \quad (3)$$

where m is the mass loss rate ($\text{gm}/\text{cm}^2 \text{ sec}$),

R is the gas constant ($\text{ergs}/\text{mole } ^\circ\text{C}$),

T_w is the temperature of the evaporating surface ($^\circ\text{K}$)

Δp is the pressure difference (dynes/cm^2) between vapor at the surface and in the stream.

For simplicity, Δp is simply taken to be the vapor pressure of tungsten at the surface temperature T_w ; in an open cycle system there is negligible partial pressure of tungsten in the stream itself. Tungsten loss and surface depletion or erosion rates were calculated from equation (3) for the temperatures of interest. The results are given in Table 4-3. It is interesting to note that the resulting rates are almost two orders of magnitude less than the rates based on vacuum evaporation (Table 4-2).

Table 4-3

Tungsten Electrode Mass Transfer Loss
(Diffusion into Plasma Stream)

Temperature ($^\circ\text{K}$)	Mass Loss Rate ($\text{gm}/\text{cm}^2 \text{ sec}$)	Surface Erosion Rate ($\text{mm}/100 \text{ hours}$)
2500	2.02×10^{-11}	3.76×10^{-6}
2750	1.37×10^{-10}	1.37×10^{-4}
3000	1.68×10^{-8}	3.12×10^{-3}
3250	1.55×10^{-7}	2.88×10^{-2}
3500	1.30×10^{-6}	2.41×10^{-1}

These mass transfer and vacuum evaporation calculations do not take into consideration possible chemical reactions between the cyanogen-oxygen combustion products and the tungsten electrodes. The $\text{C}_2\text{N}_2\text{-O}_2$ reaction products will include (7) N_2 , CO , CO_2 , and O_2 all of which can react with tungsten (8) and the effects of which should, of course, be thoroughly investigated in a complete analysis. However, this presented a task considerably in excess of the scope of the present

effort in that the simultaneous solution of the governing equilibrium equations would require machine computation. A simple analysis was made, nonetheless, to estimate the electrode degradation because of tungsten oxidation.

The oxide of tungsten most frequently treated in the literature is the trioxide, WO_3 . One may expect some WO_3 formation according to the reaction:



for which $\Delta G = -50,500 + 10.35T$ (9). Knowing the free energy of the reaction as a function of temperature, the effect of the WO_3 production and attendant tungsten mass loss may be calculated over the temperature range of interest. Since it may be shown that the O_2 content in the $C_2N_2-O_2$ combustion products is quite small, the reaction of equation (4) may be treated separately without a simultaneous recalculation and adjustment of the partial pressures of the other constituents of the gas.

Since $\Delta G = -RT \ln K$ where $K = (p_{WO_3})^{2/3}/(p_{O_2})$, the partial pressure of the tungsten trioxide (p_{WO_3}) may be determined once the partial pressure of the oxygen (p_{O_2}) is known. Knowing p_{WO_3} , its mass loss rate (and that of the tungsten metal) may be calculated on the basis of both diffusion into the plasma stream (mass transfer) and vacuum evaporation. The calculation of the effect of the reaction of equation (4) thus began with the estimation of the oxygen partial pressure in the plasma.

The partial pressures of the major constituents of the $C_2N_2-O_2$ combustion products are known (7) and are given below:

Table 4-4

Partial Pressures of $C_2N_2-O_2$ Combustion Products (Ref. 7)

Pressure = 1 atmosphere, Temperature = 4520°K

Seeding: 0.10 initial (precombustion) mole fraction of Cs.

CN:	0.001 atm	Cs:	0.040
N_2 :	0.297	N:	0.005
CO:	0.598	O:	0.002
C:	0.002	$e^- = Cs^+$:	0.027

The O_2 content was estimated from a consideration of the reaction

$$O_2 = 2(O)$$

for which it was estimated that $K \geq 4$ at $4520^\circ K$ (10). Since in this case $K = (p_O)^2/(p_{O_2})$, $(p_{O_2}) \leq (p_O)^2/4$ and assuming $(p_{O_2}) + (p_O) \approx 0.002$ atm, we find that $p_{O_2} \leq 10^{-6}$ atm.

Having thus estimated p_{O_2} , p_{WO_3} may be computed knowing the free energies at the particular temperature. The results are presented in Table 4-5.

Table 4-5

WO_3 Partial Pressure from $2/3 W(s) + O_2 = 2/3 WO_3(g)$

$$\Delta G = -50,000 + 10.35T = -RT \ln K$$

$$\text{where } K = (p_{WO_3})^{2/3}/(p_{O_2})$$

$$\text{and } p_{O_2} = 10^{-6} \text{ atm.}$$

Temperature (°K)	ΔG (Kcal/mole)	K	(p_{WO_3}) (dynes/cm ²)
2500	-24.6	142.	1.69
2750	-22.0	56.5	0.425
3000	-19.5	26.5	0.1365
3250	-16.9	13.77	0.0512
3500	-14.3	7.85	0.022

This information in turn allows the calculation of the WO_3 loss rates, either by mass transfer or vacuum evaporation. The results are listed in Table 4-6. The vacuum evaporation was computed using equation (1) where M was taken to be the molecular weight of WO_3 . The mass transfer rate of WO_3 was calculated from equation (3) with Δp equal to the WO_3 vapor pressure (in dynes/cm²) given in Table 4-5; h_D , characteristic only of the gas stream, remained the same.

The mass transfer calculation again predicts rates some two orders of magnitude less than on the basis of vacuum evaporation. The numerical value of the tungsten loss rate will be less (by the ratio of the molecular weights) than for the WO_3 loss. Table 4-7 lists the tungsten loss rates because of WO_3 formation from

tungsten- O_2 reaction, plus the surface erosion rates, for both vacuum evaporation and mass transfer.

Table 4-6
Loss Rates of WO_3

Temperature (°K)	Loss by Vacuum Evaporation (gm/cm ² sec)	Loss by Mass Transfer (gm/cm ² sec)
2500	2.26×10^{-5}	3.22×10^{-7}
2750	5.40×10^{-6}	7.35×10^{-8}
3000	1.66×10^{-6}	2.16×10^{-8}
3250	6.0×10^{-7}	7.5×10^{-9}
3500	2.48×10^{-7}	3.0×10^{-9}

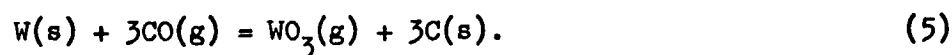
Table 4-7
Tungsten Electrode Loss by Oxidation
(WO_3 Formation from $W-O_2$ Reaction)

Temperature (°K)	Loss by Vacuum Evaporation		Loss by Diffusion into Stream	
	Mass Loss (gm/cm ² sec)	Surface Erosion (mm/100 hours)	Mass Loss (gm/cm ² sec)	Surface Erosion (mm/100 hours)
2500	1.79×10^{-5}	3.33	2.55×10^{-7}	4.74×10^{-2}
2750	4.28×10^{-6}	7.96×10^{-1}	5.83×10^{-8}	1.08×10^{-2}
3000	1.32×10^{-6}	2.45×10^{-1}	1.72×10^{-8}	3.20×10^{-3}
3250	4.76×10^{-7}	8.85×10^{-2}	5.95×10^{-9}	1.11×10^{-3}
3500	1.97×10^{-7}	3.66×10^{-2}	2.38×10^{-9}	4.42×10^{-4}

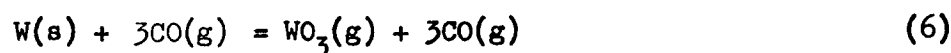
It is seen that the mass transfer analysis again yields degradation rates some two orders of magnitude less than the assumption of vacuum evaporation. The trends shown in this table indicate a decreasing loss at higher temperatures. Comparison of Tables 4-2, -3, and -7, however, shows tungsten oxidation to be the predominant effect at lower temperatures ($< 3000^\circ K$) and evaporation at high ($> 3000^\circ K$).

A number of other possible chemical reactions with tungsten electrodes have been considered, including reaction with CO_2 , CO , and N_2 ; the last two species constitute about ninety per cent of the post-combustion gas. (Table 4-4).

Very little WO_3 formation may be expected by the reaction



It has been shown (11) that at 4800°F (2920°K), 0.5 atm. pressure of $CO(g)$ yields but 5×10^{-15} atm. of $WO_3(g)$, a completely negligible quantity. In fact the high CO partial pressure in the Cs -seeded $C_2N_2-O_2$ combustion products (~ 0.6 atm. for the cesium seeding level of interest (7)) serves to inhibit $WO_3(g)$ formation because of tungsten oxidation by CO_2 . A CO -to- CO_2 partial pressure ratio of the order of 100 has been claimed (11) significantly to reduce tungsten oxidation ($WO_3(g)$ formation) by the reaction



From a tabulation of calculated equilibrium partial pressures of $WO_3(g)$ by tungsten- CO_2 reaction at various temperatures and CO -to- CO_2 partial pressure ratios (11), the $WO_3(g)$ pressure has been estimated for the p_{CO}/p_{CO_2} value expected in the $C_2N_2-O_2$ combustion products; this ratio will later be shown to be approximately 2×10^4 . The tungsten loss rates corresponding to these $WO_3(g)$ pressures are shown in Table 4-8.

Table 4-8
Tungsten Electrode Loss by Oxidation
(WO_3 Formation from $W-CO_2$ Reaction; $p_{CO}/p_{CO_2} = 2 \times 10^4$)

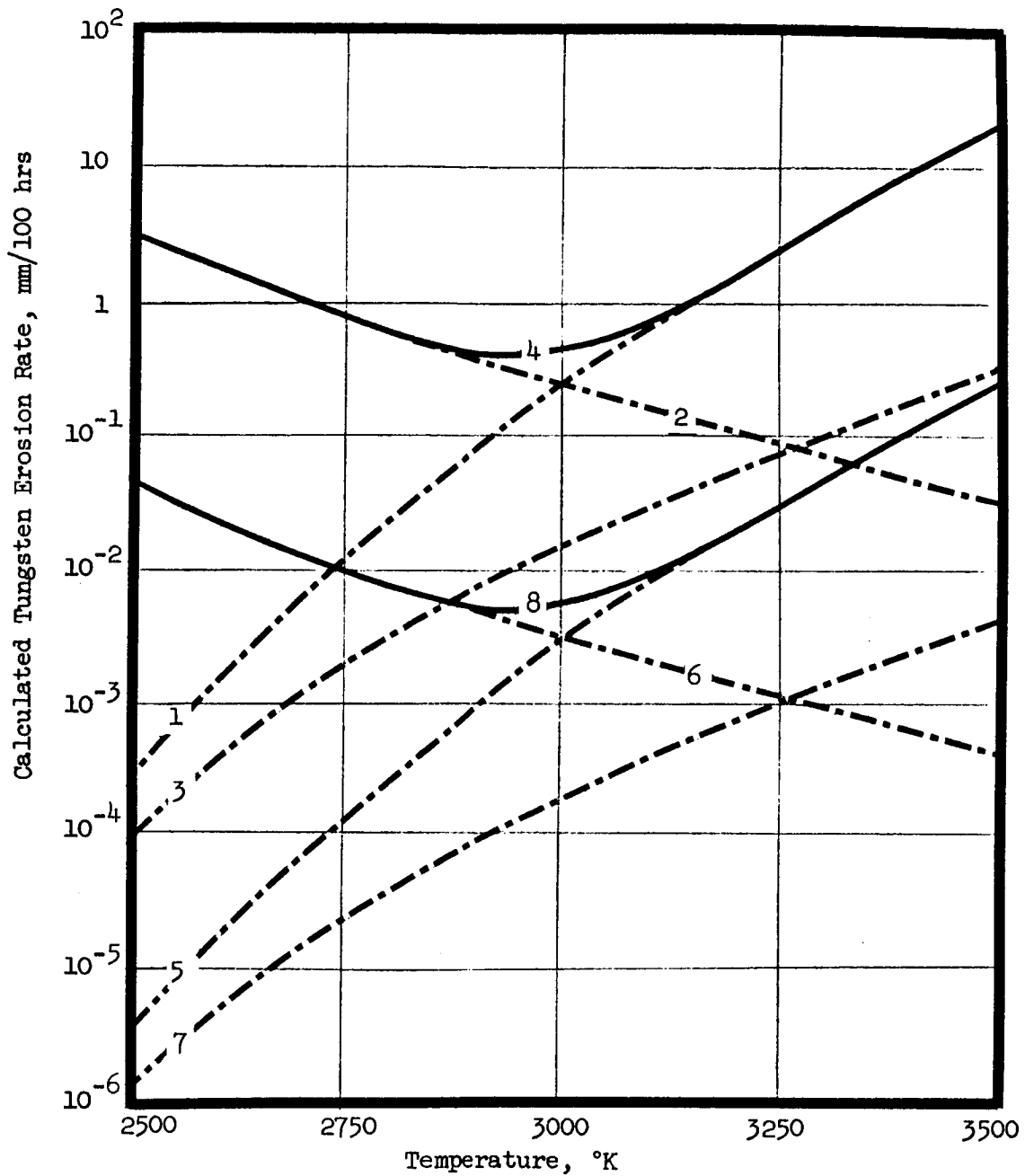
Temperature (°K)	2500	2750	3000	3250	3500
$WO_3(g)$ Pressure (dynes/cm ²)	5×10^{-5}	10^{-3}	8×10^{-3}	4×10^{-2}	2×10^{-1}
<u>Loss by Vacuum Evaporation</u>					
Mass Loss (gm/cm ² sec)	5.30×10^{-10}	1.01×10^{-8}	7.75×10^{-8}	3.72×10^{-7}	1.79×10^{-6}
Surface Erosion (mm/100 hours)	9.86×10^{-5}	1.88×10^{-3}	1.44×10^{-2}	6.92×10^{-2}	3.33×10^{-1}
<u>Loss by Diffusion into Stream</u>					
Mass Loss (gm/cm ² sec)	7.57×10^{-12}	1.37×10^{-10}	1.01×10^{-9}	4.65×10^{-9}	2.05×10^{-8}
Surface Erosion (mm/100 hours)	1.41×10^{-6}	2.55×10^{-5}	1.88×10^{-4}	8.65×10^{-4}	3.81×10^{-3}

Reaction between the tungsten and the nitrogen content of the plasma will be assumed to be relatively insignificant, based upon experimental results (12) to 2373°K.

A summary is appropriate at this point. Of the possible electrode deterioration mechanisms considered, only two appear to be significant. This is shown in Figure 4-2 where the surface erosion rates listed in Tables 4-2, -3, -7, and -8 are plotted; for comparison purposes, both the vacuum evaporation and stream diffusion rates are shown. It is apparent that oxidation by CO_2 is a second order effect and that the electrode loss is governed primarily by oxidation by O_2 or by tungsten evaporation, depending upon the temperature range. Also shown in the figure are the net effects of these two processes in combination. The curves show a minimum near 2900°K. One would not necessarily expect to find such a pronounced minimum experimentally, since a number of simplifying assumptions were made in the above analysis. Only a few possible chemical reactions were considered, and these were studied separately, without the more elegant approach of the simultaneous computation of the various partial pressures involved. Nonetheless, the results indicate potentially satisfactory performance for tungsten electrodes.

On the basis of mass transfer by diffusion into the plasma stream, the conclusion from Figure 4-2 is that tungsten electrodes should erode at a rate of about 0.25 mm/100 hours at 3500°K, a temperature near the melting point and fully capable of providing more than ample thermionic emission current density to insure satisfactory generator operation. Operation at lower electrode temperature would, of course, yield longer lifetimes.

Electrical Insulator Erosion The erosion degradation of sidewall electrical insulators for open cycle MHD (vortex) power generators has been carried through in a fashion similar to the approach employed above for electrodes. Several obvious differences, however, must be considered. As in the case of electrodes, it is desirable to operate the insulators at as high a temperature as possible so as to maintain generator efficiency through minimum heat loss. The tendency of the resistivity of all high temperature insulators to drop rapidly with increasing temperature necessitates some compromise in this area. Consequently an insulator temperature yielding adequate lifetime may in fact turn out to be too high to maintain sufficient interelectrode resistivity; this in turn may require lower temperature operation with the attendant efficiency penalty.



Legend:

	Vacuum Evaporation	Diffusion into Stream
Tungsten Evaporation	1	5
WO ₃ Effect from W-O ₂ Reaction	2	6
WO ₃ Effect from W-CO ₃ Reaction	3	7
Total Loss	4	8

Calculated Tungsten Erosion Rate

Figure 4-2

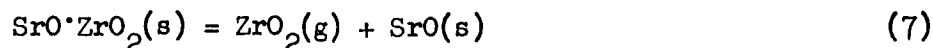
A second area of difference is in the basic mass (or heat) transfer process. Mass transfer from tungsten electrodes was calculated on the basis of laminar flow. Both theory and experiment indicate that the sidewall heat transfer is likely to be turbulent. Consequently, the mass transfer rates for diffusion from insulators into the plasma stream were computed on the basis of a turbulent heat transfer coefficient.

In practice, it has been found advantageous to construct the generator sidewalls of two layers, an electrically insulating layer in "direct" contact with the electrodes and the plasma and a "backing" layer of thermal insulation (usually zirconium oxide). The analysis to follow will consider only the former; this will be the more critical component since it will operate at considerably higher temperature and will have a more direct influence on generator performance. The thermal insulation layer should present no particular difficulties, particularly since the finite thickness of electrical insulator (usually also at least a fair thermal insulator) may be expected to keep even the "hot" side of the thermal insulator at a temperature sufficiently low so that chemical erosion is negligible.

A variety of high temperature electrical insulators have been studied for use in MHD power generators. For open cycle applications strontium zirconate ($\text{SrO} \cdot \text{ZrO}_2$) has been shown (9) to enjoy substantial advantages over magnesium oxide (MgO), beryllium oxide (BeO), and boron nitride (BN). Thus the degradation rate of $\text{SrO} \cdot \text{ZrO}_2$ in the presence of the $\text{C}_2\text{N}_2\text{-O}_2$ combustion products will be estimated to evaluate the potential of this insulator for use in an MHD generator employing this fuel. As before, mass loss both by the vacuum evaporation and stream diffusion mechanisms will be calculated.

The accuracy of the subsequent analysis will depend strongly upon the value assumed for the free energy of formation of strontium zirconate. The exact value is not available, but it has been assumed (9) that a reasonable estimate is -30 Kcal/mole, based upon the free energy of formation of $\text{CaO} \cdot \text{SiO}_2$, an analogous compound. To indicate the strong dependence of the $\text{SrO} \cdot \text{ZrO}_2$ degradation rate upon this free energy of formation, the calculations will be carried out for two other values, -10 Kcal/mole and -60 Kcal/mole, which may be regarded as bounding values between which the true value must lie (13).

Two processes governing the degradation of $\text{SrO} \cdot \text{ZrO}_2$ may be considered, volatilization of ZrO_2 or Sr. Free energies for these reactions may be calculated, within the limitations discussed above for the $\text{SrO} \cdot \text{ZrO}_2$ formation energy. The effect of ZrO_2 volatilization may be estimated from the reaction



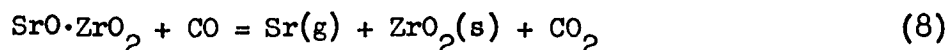
for which $\Delta G = \frac{173,170}{223,170} - 38.0 T$, depending upon the value taken for ΔG_f ($\text{SrO} \cdot \text{ZrO}_2$). Rate calculations for $\text{SrO} \cdot \text{ZrO}_2$ degradation have been carried through (in the same manner as for the electrode erosion) in the temperature range 2000°K to 3000°K, where the latter temperature represents the approximate melting point of strontium zirconate. The results are summarized in Table 4-9.

The rates listed for loss by diffusion into the plasma stream were calculated from equation (3) with the average mass transfer coefficient $\bar{h}_D = 233.6 \text{ cm/sec}$; this value was based on a film heat transfer coefficient $\bar{h} = 2.23 \times 10^5 \text{ erg/cm}^2 \text{ sec } ^\circ\text{K}$, as determined for turbulent flow conditions (14).

It is apparent from Table 4-9 that the rate at which insulator material may be expected to be lost is extremely sensitive to the free energy of formation assumed; the loss rates for $\Delta G_f (\text{SrO} \cdot \text{ZrO}_2) = -10 \text{ Kcal/mole}$ range from about 3×10^5 to 4.5×10^3 times greater, depending upon the temperature, than for $\Delta G_f (\text{SrO} \cdot \text{ZrO}_2) = -60 \text{ Kcal/mole}$.

Even under the worst conditions of temperature and assumed formation energy, however, the calculated erosion rates are not particularly severe. Unfortunately $\text{SrO} \cdot \text{ZrO}_2$ loss by ZrO_2 volatilization is not the predominant effect in the degradation process. As will be shown below, $\text{SrO} \cdot \text{ZrO}_2$ loss by Sr volatilization is the controlling factor.

This effect is described by the reaction



for which $\Delta G = \frac{115,990}{165,990} - 21.84 T$, depending upon $\Delta G_f (\text{SrO} \cdot \text{ZrO}_2)$.

In the reaction of equation (8)

Table 4-9

SrO·ZrO₂ Loss by ZrO₂ Volatilization

SrO·ZrO ₂ Loss:						
Formation Energy (Kcal/mole)	Temperature (°K)	By Vacuum Evaporation		By Diffusion into Stream		
		p _{ZrO₂} (dynes/cm ²)	Mass Loss (gm/cm ² sec.)	Surface Erosion (mm/100 hours)	Mass Loss (gm/cm ² sec.)	Surface Erosion (mm/100 hours)
-10	2000	2.31 x 10 ⁻⁵	4.62 x 10 ⁻¹⁰	3.04 x 10 ⁻⁴	7.34 x 10 ⁻¹²	4.82 x 10 ⁻⁶
	2250	3.01 x 10 ⁻³	5.67 x 10 ⁻⁸	3.73 x 10 ⁻²	8.52 x 10 ⁻¹⁰	5.60 x 10 ⁻⁴
	2500	1.43 x 10 ⁻¹	2.56 x 10 ⁻⁶	1.68	3.64 x 10 ⁻⁸	2.39 x 10 ⁻²
	2750	3.39	5.78 x 10 ⁻⁵	38.0	7.84 x 10 ⁻⁷	5.15 x 10 ⁻¹
	3000	48.9	7.98 x 10 ⁻⁴	5.24 x 10 ²	1.04 x 10 ⁻⁵	6.83
-30	2000	1.495 x 10 ⁻⁷	2.98 x 10 ⁻¹²	1.96 x 10 ⁻⁶	4.77 x 10 ⁻¹⁴	3.13 x 10 ⁻⁸
	2250	3.34 x 10 ⁻⁵	6.29 x 10 ⁻¹⁰	4.13 x 10 ⁻⁴	9.44 x 10 ⁻¹²	6.20 x 10 ⁻⁶
	2500	2.53 x 10 ⁻³	4.53 x 10 ⁻⁸	2.98 x 10 ⁻²	6.44 x 10 ⁻¹⁰	4.23 x 10 ⁻⁴
	2750	8.89 x 10 ⁻²	1.52 x 10 ⁻⁶	9.98 x 10 ⁻¹	2.06 x 10 ⁻⁸	1.35 x 10 ⁻²
	3000	1.69	2.76 x 10 ⁻⁵	18.1	3.59 x 10 ⁻⁷	2.36 x 10 ⁻¹
-60	2000	7.79 x 10 ⁻¹¹	1.56 x 10 ⁻¹⁵	1.02 x 10 ⁻⁹	2.48 x 10 ⁻¹⁷	1.63 x 10 ⁻¹¹
	2250	4.02 x 10 ⁻⁸	7.58 x 10 ⁻¹³	4.98 x 10 ⁻⁷	1.14 x 10 ⁻¹⁴	7.49 x 10 ⁻⁹
	2500	5.98 x 10 ⁻⁶	1.15 x 10 ⁻¹⁰	7.55 x 10 ⁻⁵	1.52 x 10 ⁻¹²	9.98 x 10 ⁻⁷
	2750	3.55 x 10 ⁻⁴	6.05 x 10 ⁻⁹	3.97 x 10 ⁻³	7.62 x 10 ⁻¹¹	5.00 x 10 ⁻⁵
	3000	1.07 x 10 ⁻²	1.75 x 10 ⁻⁷	1.15 x 10 ⁻¹	2.26 x 10 ⁻⁹	1.48 x 10 ⁻³

$$K = \left(\frac{p_{\text{CO}_2}}{p_{\text{CO}}} \right) p_{\text{Sr}} \quad (9)$$

so that the strontium vapor pressure or volatilization tendency may be thought of as being influenced by the $p_{\text{CO}}/p_{\text{CO}_2}$ partial pressure ratio of the combustion plasma. For the present case of cesium-seeded $\text{C}_2\text{N}_2\text{-O}_2$, it has been shown that $p_{\text{O}_2} \approx 10^{-6}$ atm.

Thus from the reaction



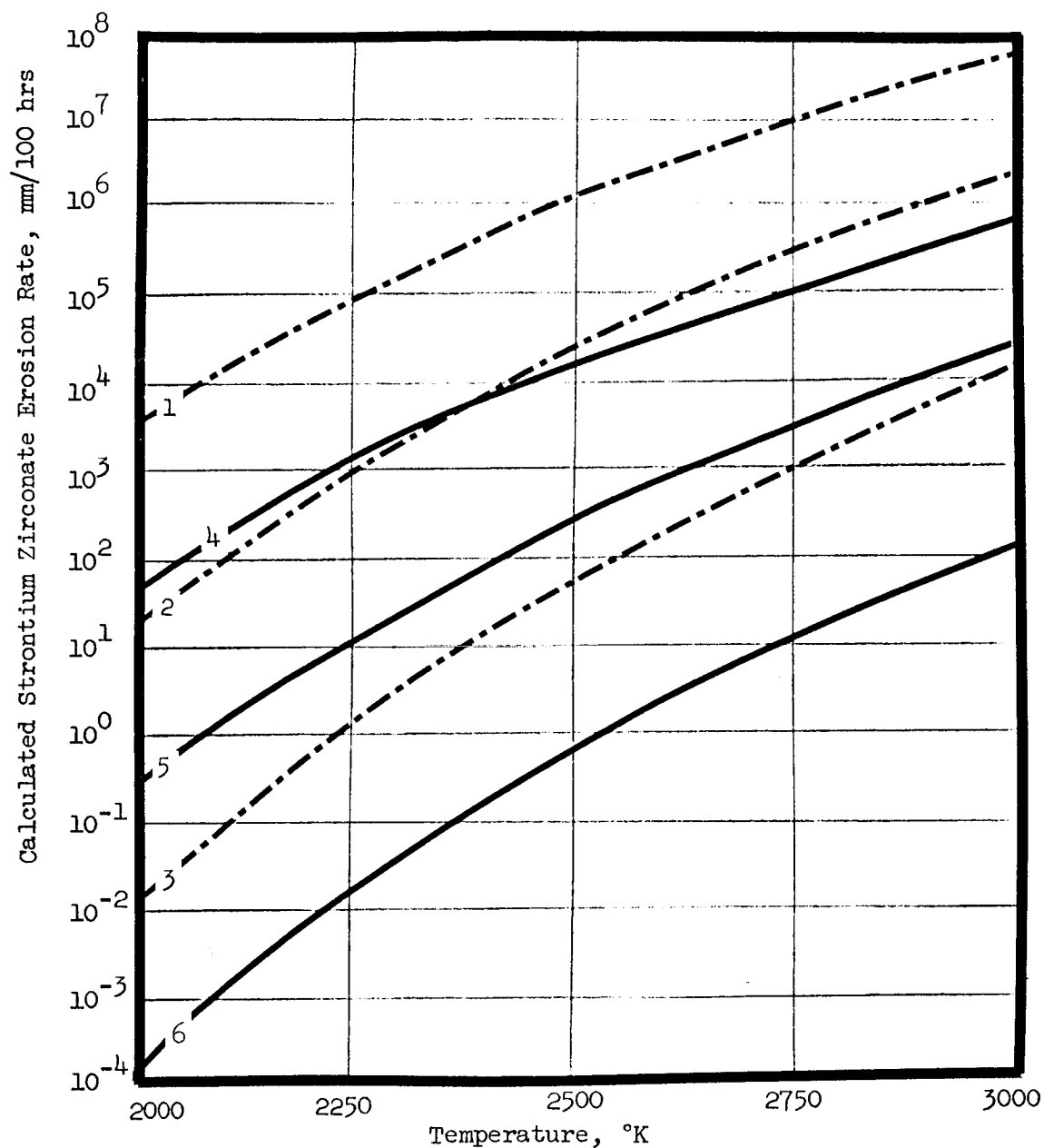
for which $\Delta G = -67,500 + 20.71 T$, one may compute ΔG at the plasma temperature and, since $p_{\text{CO}} = 0.598$ atm. (Table 4-4), one finds $p_{\text{CO}}/p_{\text{CO}_2} \approx 2 \times 10^4$. Equation (9) then becomes

$$p_{\text{Sr}} = 2 \times 10^4 K \quad (11)$$

which shows the adverse effect of the high $p_{\text{CO}}/p_{\text{CO}_2}$ ratio of the plasma in terms of the increased tendency for Sr volatilization. (It will be recalled that it was this high ratio which so effectively inhibited the tungsten electrode oxidation process described by equation (6)).

The extent of the strontium volatilization may now be calculated from equation (8) for the three values of $\Delta G_f(\text{SrO} \cdot \text{ZrO}_2)$. The results are given in Table 4-10. Here again the effect of the various values of free energy of formation is apparent, but more important is the fact that the loss rates calculated are some 10^5 to 10^7 higher than for $\text{SrO} \cdot \text{ZrO}_2$ degradation by ZrO_2 volatilization (Table 4-9). The latter effect may therefore be regarded as insignificant relative to the former. The surface erosion rate data from Table 4-10 are plotted in Figure 4-3 for both vacuum evaporation and Sr diffusion into the plasma stream.

A number of conclusions may be drawn from Figure 4-3. First of all it will be assumed that erosion by diffusion into the plasma stream constitutes a more realistic loss model than vacuum evaporation. Furthermore an insulator erosion rate of about 10^2 mm/100 hours will be taken as representative of what might be acceptable in a 10 kw-size vortex power generator; this rate corresponds to about a twenty per cent increase in generator volume (twenty per cent pressure



Legend:

- | | | |
|---|---|-------------------------|
| 1 | $\Delta G_f(\text{SrO} \cdot \text{ZrO}_2) = -10 \text{ Kcal/mole}$ | } Vacuum Evaporation |
| 2 | $\Delta G_f(\text{SrO} \cdot \text{ZrO}_2) = -30 \text{ Kcal/mole}$ | |
| 3 | $\Delta G_f(\text{SrO} \cdot \text{ZrO}_2) = -60 \text{ Kcal/mole}$ | |
| 4 | $\Delta G_f(\text{SrO} \cdot \text{ZrO}_2) = -10 \text{ Kcal/mole}$ | } Diffusion into Stream |
| 5 | $\Delta G_f(\text{SrO} \cdot \text{ZrO}_2) = -30 \text{ Kcal/mole}$ | |
| 6 | $\Delta G_f(\text{SrO} \cdot \text{ZrO}_2) = -60 \text{ Kcal/mole}$ | |

Calculated Strontium Zirconate Erosion Rate

Figure 4-3

Table 4-10

SrO·ZrO₂ Loss by Sr Volatilization

		SrO·ZrO ₂ Loss:					
Formation Energy (Kcal/mole)	Temperature (°K)	By Vacuum Evaporation			By Diffusion into Stream		
		P _{Sr} (dynes/cm ²)	Mass Loss (gm/cm ² sec.)	Surface Erosion (mm/100 hours)	Mass Loss (gm/cm ² sec.)	Surface Erosion (mm/100 hours)	
-10	2000	2.43 x 10 ²	5.77 x 10 ⁻³	3.79 x 10 ³	7.74 x 10 ⁻⁵	5.09 x 10 ⁻¹	
	2250	6.86 x 10 ³	1.40 x 10 ⁻¹	9.20 x 10 ⁴	1.78 x 10 ⁻³	1.16 x 10 ³	
	2500	8.42 x 10 ⁴	1.79	1.18 x 10 ⁶	2.15 x 10 ⁻²	1.41 x 10 ⁴	
	2750	7.04 x 10 ⁵	14.2	9.33 x 10 ⁶	1.63 x 10 ⁻¹	1.07 x 10 ⁵	
	3000	4.14 x 10 ⁶	8.03 x 10 ¹	5.28 x 10 ⁷	8.80 x 10 ⁻¹	5.78 x 10 ⁵	
-30	2000	1.57	3.73 x 10 ⁻⁵	2.45 x 10 ¹	5.02 x 10 ⁻⁷	3.29 x 10 ⁻¹	
	2250	7.08 x 10 ¹	1.58 x 10 ⁻³	1.03 x 10 ³	2.01 x 10 ⁻⁵	1.32 x 10 ¹	
	2500	15.00 x 10 ²	3.18 x 10 ⁻²	2.09 x 10 ⁴	3.83 x 10 ⁻⁴	2.51 x 10 ²	
	2750	18.00 x 10 ³	3.64 x 10 ⁻¹	2.39 x 10 ⁵	4.17 x 10 ⁻³	2.74 x 10 ³	
	3000	14.4 x 10 ⁴	2.79	1.83 x 10 ⁶	3.06 x 10 ⁻²	2.01 x 10 ⁴	
-60	2000	8.18 x 10 ⁻⁴	1.94 x 10 ⁻⁸	1.27 x 10 ⁻²	2.61 x 10 ⁻¹⁰	1.71 x 10 ⁻⁴	
	2250	8.54 x 10 ⁻²	1.91 x 10 ⁻⁶	1.25	2.42 x 10 ⁻⁸	1.59 x 10 ⁻²	
	2500	3.52	7.48 x 10 ⁻⁵	4.9 x 10 ¹	8.98 x 10 ⁻⁶	5.90 x 10 ⁻¹	
	2750	7.39 x 10 ¹	1.49 x 10 ⁻³	9.79 x 10 ²	1.71 x 10 ⁻⁵	1.12 x 10 ¹	
	3000	9.32 x 10 ²	1.80 x 10 ⁻²	1.18 x 10 ⁴	1.98 x 10 ⁻⁴	1.30 x 10 ²	

drop) over an hour of operation. On this basis Figure 4-3 shows that strontium zirconate would be an acceptable insulator only at temperatures of 2000°K or less if the free energy of formation of strontium zirconate is -10 Kcal/mole or less. If this energy, on the other hand, is more nearly -60 Kcal/mole, then this insulator may be operated at temperatures up to its melting point ($\sim 3000^\circ\text{K}$) without incurring excessive erosion; whether this material would maintain adequate electrical resistivity at temperatures close to its melting point is another matter.

Since the free energy of formation of $\text{SrO} \cdot \text{ZrO}_2$ is more probably some intermediate value near -30 Kcal/mole, one might expect acceptable erosion rates to temperatures near 2500°K. Figure 4-3 shows an erosion rate of 250 mm/100 hours at this temperature and 0.33 mm/100 hours for 2000°K. The upper limit of insulator operating temperature will be determined by the exact value of formation free energy and considerations of the resistivity characteristics.

Summary The lifetimes of tungsten electrodes and strontium zirconate insulators have been estimated for the case of an open-cycle vortex MHD power generator driven with a cesium-seeded cyanogen-oxygen combustion plasma. A number of chemical reactions between the various combustion products and these materials were studied in an effort to determine the process controlling the erosion rate. This rate in turn was calculated on the basis of material loss by vacuum evaporation from the solid-gas reactions and by diffusion into the plasma stream. The approach used in obtaining the lifetime estimates summarized below should be applicable as well to other electrodes and insulator materials used in conjunction with other fuels.

The behavior of tungsten electrodes was studied in terms of their vaporization tendency and chemical reaction with O_2 , CO_2 and CO to form WO_3 . The results indicate that in the temperature range of interest ($\geq 3000^\circ\text{K}$), the tungsten erosion is primarily the result of tungsten evaporation into the gas stream. Tungsten oxidation through reaction with CO_2 was determined to be a negligible factor since the high partial pressure of CO found in the $\text{C}_2\text{N}_2\text{-O}_2$ products effectively inhibited this reaction. Oxidation through reaction with O_2 was significant over a certain temperature range, but the tungsten evaporative loss was found to control the degradation at temperatures $\geq 3000^\circ\text{K}$. On the basis of

mass transfer by diffusion into the stream, it was shown that tungsten electrodes should be capable of operation at temperatures to 3500°K ($> 100 \text{ amp/cm}^2$ thermionic emission) with an erosion rate less than 0.25 mm/100 hours.

The analysis of strontium zirconate insulators ($\text{SrO} \cdot \text{ZrO}_2$) employed a similar approach. It was assumed that the $\text{SrO} \cdot \text{ZrO}_2$ could erode either by volatilization of the ZrO_2 or the Sr. The latter effect was found to be at least 10^5 times as strong as the former; the high ratio of CO to CO_2 content in the $(\text{C}_2\text{N}_2-\text{O}_2)$ plasma (which led to increased electrode lifetimes by minimizing the WO_3 formation tendency) was found to have an adverse effect upon the $\text{SrO} \cdot \text{ZrO}_2$, promoting its mass loss through Sr volatilization. The extent of this predominating effect depends strongly upon the free energy of formation of $\text{SrO} \cdot \text{ZrO}_2$, the exact value of which is unavailable; consequently the $\text{SrO} \cdot \text{ZrO}_2$ loss rates were calculated for a range of free energies of formation. On the basis of the "most probable" value (-30 Kcal/mole) a mass transfer erosion rate of 250 mm/100 hours at 2500°K was calculated; operation at 2000°K was determined to lower this rate to 0.33 mm/100 hours.

5.0 GENERATOR MAGNET SYSTEMS

Optimum magnet configurations of the permanent magnet, electromagnet (iron-core), and cryogenic superconducting type were investigated for the vortex MHD power generator. The operating characteristics of each type were determined for the example of Section 6.3 and their salient features are compared below. Air-core copper and cryogenic cooled air-core aluminum and sodium magnets were not considered since they are considered to be at least a factor of ten greater in weight than the cryogenic superconducting magnet¹.

Permanent Magnet The relationship of the permanent magnet to the vortex generator is shown in the schematic of Figure 5-1. A single C-magnet for this application is to be preferred over other possible configurations, such as a multiple-C arrangement or a single symmetric continuous-C magnet, for reasons of simplicity, compactness, and reduced flux leakage factors.

Alnico V-7 is selected for the permanent magnet material because of its high external energy density of 7×10^6 gauss-oersted. This selection insures the lightest and smallest volume permanent magnet for the given magnetic field requirements of any commercially available magnet material. A disadvantage of Alnico V-7 is its higher processing cost which is the result of the requirement for casting it in a magnetic field. The calculation of magnet weight and geometry is initiated by determining its length

$$L_m = \frac{f B_g L_g}{H_d} \quad (1)$$

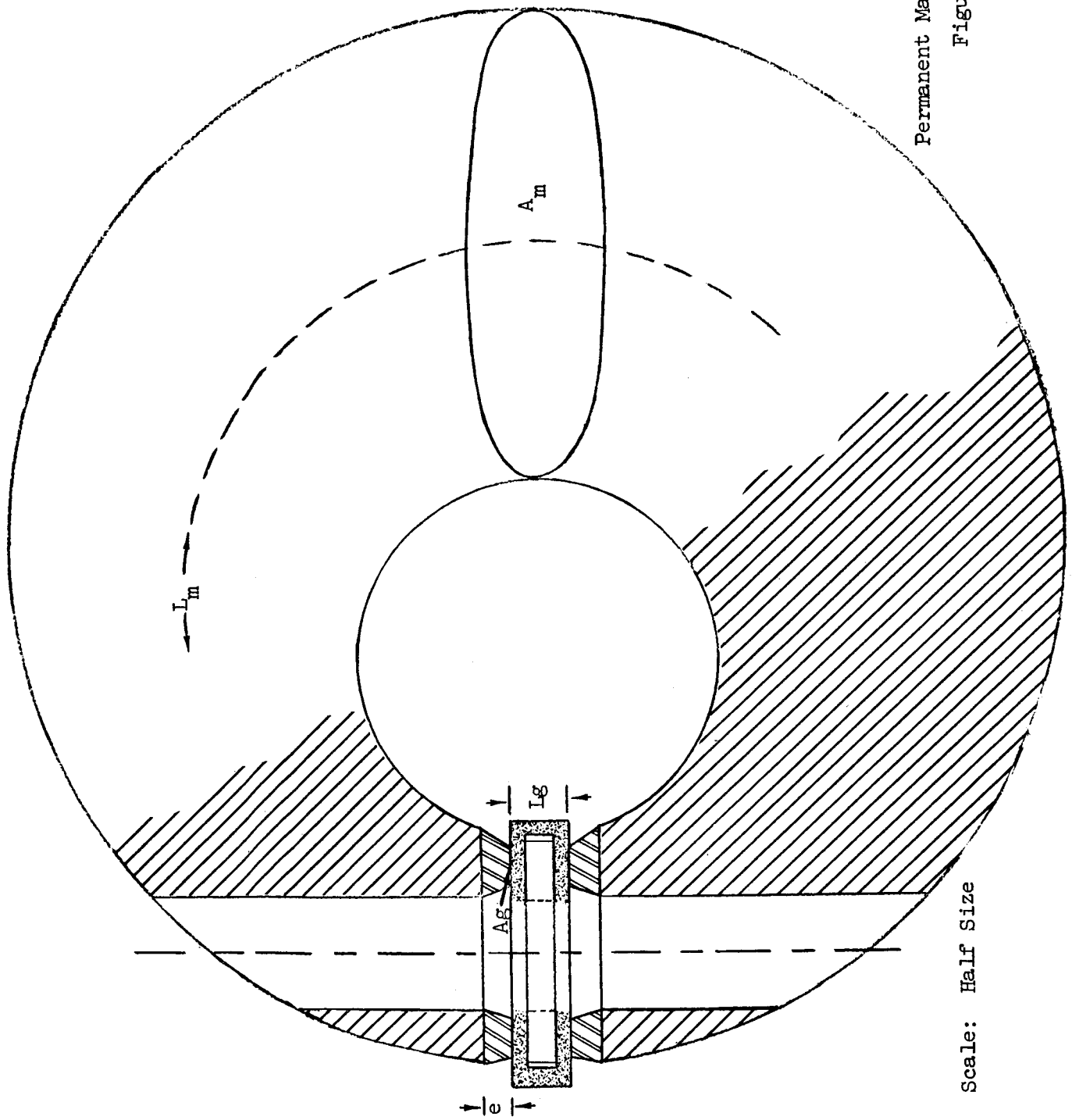
where f = reluctance factor

B_g = flux density in gap

L_g = length of gap

H_d = magnetomotive force corresponding to operating point in B-H curve.

B_g and L_g are fixed by the example at 15,000 gauss and 2.28 cm respectively. For operation at the peak energy density point on the B-H curve of Alnico V-7, H_d = 650 oersteds. The reluctance factor f is the ratio of the sum of the MMF's required by the gap, any soft iron flux concentrators, joint reluctance, and the additional MMF required to accommodate the geometry of the gap itself, to the MMF required for the gap. The usual reluctance factors vary from 1.1 to 1.5; a value of $f = 1.3$ will be assumed for this example.



Permanent Magnet Schematic

Figure 5-1

Scale: Half Size

The leakage coefficient (σ), which plays an important role in determining the magnet area (A_m), can vary however over a large range and does require calculation. This area dependence is shown by the following relation

$$A_m = \frac{B_d A_g \sigma}{B_d} \quad (2)$$

where A_m = area of magnet at its neutral section

A_g = gap area

B_d = magnetic induction corresponding to operating point on B-H curve.

the gap area (A_g) will be taken to be two thirds of the area over which the magnetic field is required by the vortex generator. The factor of two thirds is arbitrary and was selected on the basis that the large flux leakage coefficient which occurs as a result of the poor gap geometry will provide a nearly uniform flux density over the entire active volume of the vortex generator. The two thirds factor also corresponds to the approximate value of area convergence required by the flux concentrators (i.e., pole pieces). A_g is thus 22.1 cm^2 .

The leakage coefficient was calculated on the basis of generalized formula for permanent magnet configurations, Reference 2. For the concentric and slightly eccentric C-magnet with tapered soft iron pole pieces

$$\sigma = 1 + \frac{L_g}{A_g} \left[1.7 U_a \left(\frac{e}{e + L_g} + \frac{a}{a + L_g + e} \right) \right] \quad (3)$$

where the length, a , is calculated as one-sixth of the C-magnet's average length, U_a is the perimeter of the gap ($= 2\pi [r_1 + r_0]$), and e equals the length of each tapered pole piece. For the dimensions indicated in Figure 5-1, the corresponding leakage coefficient is $\sigma = 7.7$.

The area of the magnet at its neutral plane is thus, for $B_d = 10,770$ gauss (the induction of Alnico V-7 at the peak energy density point of operation), equal to $A_m = 237 \text{ cm}^2$. The average cross-sectional area of the magnet, assuming a linear taper between the neutral plane and the gap, is then $\bar{A}_m = 135 \text{ cm}^2$.

The resulting weight of the permanent magnet, calculated on the basis of

$$W_{\text{mag.}} = \rho_{\text{mag.}} \bar{A}_m L_m$$

and the mass density of Alnico V-7 (0.265 lb/in^3) is 149 lb. This will be the heaviest of the magnet systems considered but it has a fixed weight, is independent of the dormancy or power duration requirements, and demands no external cooling.

It is worth mentioning in passing that one might expect a more efficient permanent magnet arrangement if the magnet material is located adjacent to both sides of the gap and with an iron backstrap return path. The flux leakage coefficient in this case is reduced to 6.3, but the change is so slight that the corresponding reduction in the weight of the Alnico V-7 is more than compensated by the added weight of the iron return path. The weight estimate above is therefore considered to be a minimum regardless of the arrangement of the magnetic circuit.

Electromagnet An iron-core copper electromagnet of the configuration described in Figure 5-2 will be considered next. A completely symmetric geometry will be assumed although it is understood that provision for the generator jet(s) must be included in a more exact analysis. The optimum configuration for this type of magnet is that of Figure 5-2; it is based on prior experience with calculating examples of magnet systems for the vortex generator study of the NAS5-703 contract.

The copper coil must provide the MMF required by both the iron and the gap. Thus the amp-turns required by the gap are given by

$$NI_{\text{gap}} = \frac{10B_g L_g}{4\pi} \quad (4)$$

where $B_g = 15,000$ gauss

$$L_g = 2.276 \text{ cm}$$

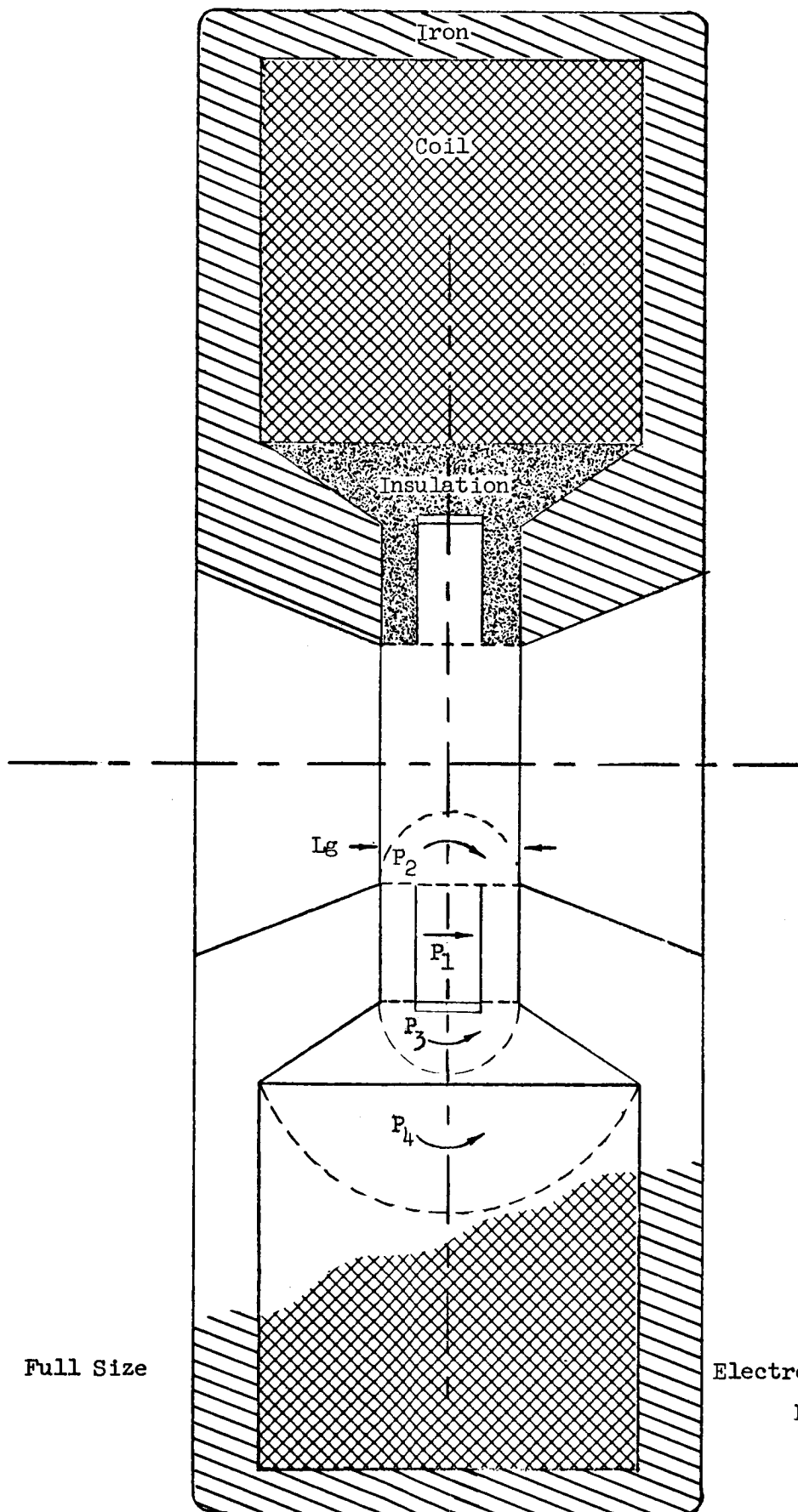
and equal 23,900. The iron requirement, given by

$$NI_{\text{iron}} = \frac{10 H_{\text{iron}} L_{\text{iron}}}{4\pi} \quad (5)$$

where $H_{\text{iron}} = 70$ oersted at $B_{\text{iron}} = 18,000$ gauss for pure iron annealed

$$L_{\text{iron}} \approx 30 \text{ cm}$$

is 1,670 amp-turns. Thus the total requirement is 25,600 amp-turns. This can be satisfied by 60 and 90 turns for the high and low current cases respectively,



Scale: Full Size

Electromagnet Schematic
Figure 5-2

of the generator example in Section 6.3, if the coil is wired in series with the output of the generator. A coil with this number of turns and with the geometry indicated in Figure 5-2 should be convenient to fabricate by winding full coil-width strips of insulated copper into a single coil. The required exterior coil shape can be machined subsequently.

The power dissipated by this coil can be calculated by the following equation

$$\text{Power}_{\text{coil}} = \frac{I^2 \rho^* 2\pi \bar{r}}{ab} \quad (6)$$

where I = coil current

ρ^* = copper resistivity, incorporating a packing factor

$$= 3 \times 10^{-6} \text{ ohm-cm}$$

\bar{r} = mean coil radius

ab = cross-sectional area of coil

If we assume the coil to have the dimensions $a = b = 6$ cm and a mean radius $\bar{r} = 8$ cm, then the power dissipation is approximately 2.4 kw. The coil could be made smaller, for a net saving of weight, but at the expense of increasing the power dissipation and thereby possibly exceeding the regenerative cooling capacity of the fuel and oxidizer.

In order to complete the calculation of the magnet structure, and hence its weight, the flux leakage coefficient and iron area must be determined next.

The formulas derived by Roter (Reference 3) for estimating the permeances of probably flux paths were employed for the calculation of the leakage coefficient:

$$\sigma = \frac{\sum_i P}{P_1} \quad (7)$$

where $\sum_i P$ = sum of all flux path permeances

P_1 = gap permeance

The four flux paths considered are labeled in Figure 5-2. Their permeances were calculated to be 9.76, 6.53, 4.65, and 1.91 μ -cm respectively for paths one

through four, where μ is the permeability of free space. The total permeance is thus 22.8 μ -cm and the leakage coefficient $\sigma = 2.34$. For a magnet gap area equal to the area defined by the outer and inner radius of the vortex generator, over which the 15,000 gauss field is required, the cross sectional area of the iron,

$$A_{\text{iron}} = \sigma \frac{B_g}{B_{\text{iron}}} A_g \quad (8)$$

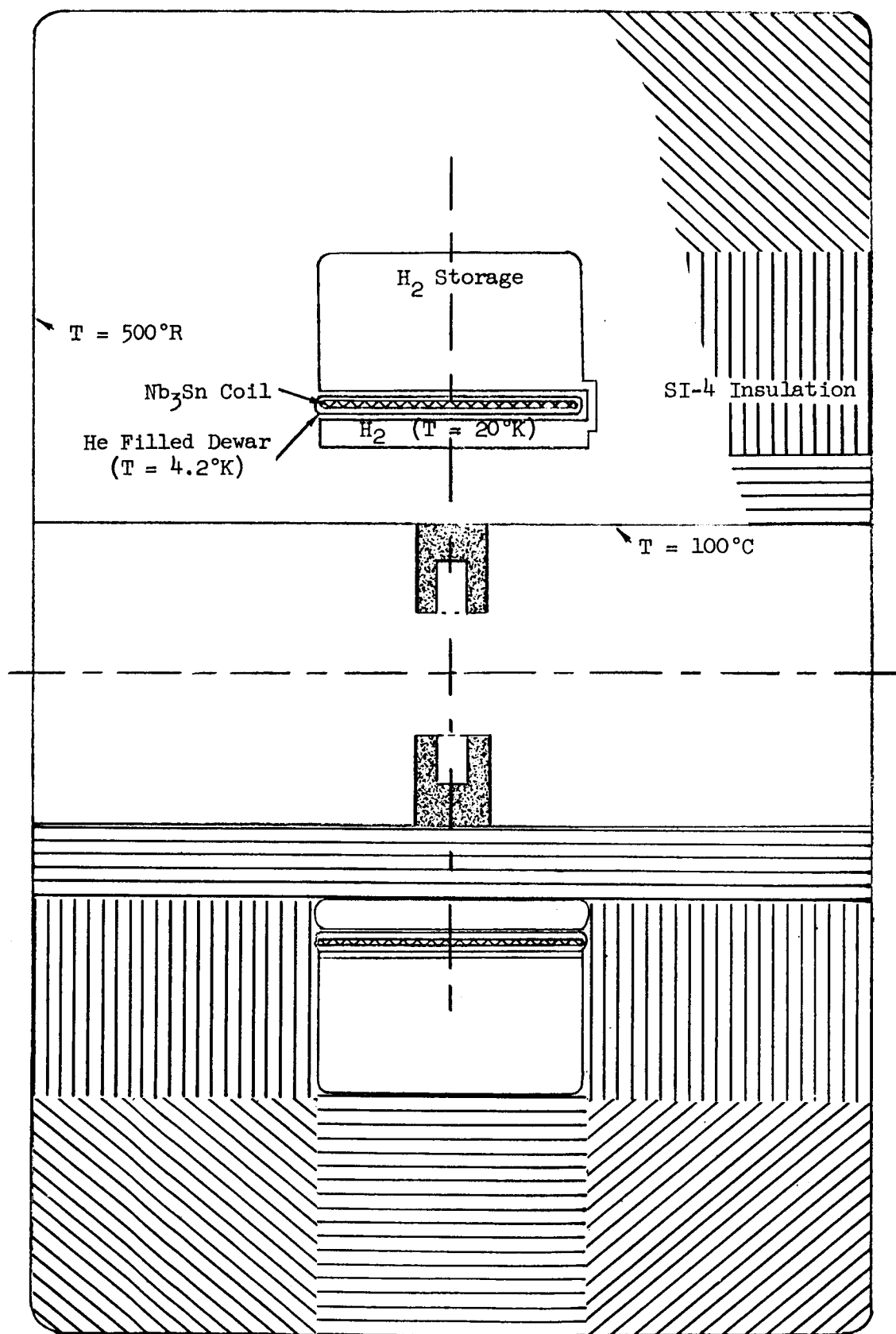
is 52.7 cm² for $B_{\text{iron}} = 18,000$ gauss and $A_g = 31.6$ cm². The radial thickness of the iron at the central plane of the generator is thus, for an outer radius of the coil of 11 cm, equal to 0.7 cm. This value permits an estimate of the resulting envelop and weight of the magnet assembly. The assembly occupies a volume defined by a cylinder of 23.4 cm diameter by 7.4 cm length. Its weight is approximately 55 lb.

In summary, the electromagnet weighs approximately one third of the permanent magnet but it requires about one third of the gross power output of the generator in this example and also requires special cooling about equal to its power dissipation.

Superconducting Magnet The cryogenic temperatures required by a superconducting magnet coil can be maintained by refrigeration or by cryogenic fluids with constant boil off. It is this latter method which will receive attention here since it is expected to be the more reliable and lighter of the two methods for a reasonably short total mission time.

The arrangement of the various elements of the magnet system is illustrated in Figure 5-3. The insulation thicknesses indicated there are not necessarily optimum but they are adequate in maintaining negligibly small heat flux. The temperature distribution noted in the above figure corresponds to that which occurs during generator operation. The outer surface temperature of 500°R is assumed to correspond to the normal operating temperature of electrical components which are supposed to comprise the mission payload.

For purposes of simplicity in this example, a single cryogenic magnet system is assumed. In practice two separate systems in a Helmholtz pair arrangement would be employed in order to provide space for the nozzles of the generator. However,



Superconducting Magnet Schematic

Figure 5-3

the performance of this dual magnet system is not expected to be significantly different from the calculated performance of a single system.

By use of a superinsulation, such as the Linde Co. SI-4 with a mean value of thermal conductivity equal to 2.5×10^{-5} BTU °F/hr ft (in vacuum, over the temperature range of interest) and a single low emissivity ($\epsilon = 0.02$) radiation shield between the H_2 and He tanks, the following boil off rates are obtained during generator operation:

$$W_{H_2} = (2.0) 10^{-4} \text{ lb/hr.}$$

$$W_{He} = (1.4) 10^{-6} \text{ lb/hr}$$

These rates include an allowance for heat conduction through tank supports and fill lines (equal to the heat conduction through the insulation or shielding) and do not include the boil off due to heat flux to the outer hydrogen storage tank. The latter boil off rate cannot be estimated until the tank size, which depends on the dormancy time, is known.

The hydrogen requirement for a dormancy of three months was calculated to be 0.5 lb; the helium boil off is negligible for this duration of time. The entire cryo-magnet system weight for a three month mission is approximately 17 lb of which 12 lb is represented by the SI-4 insulation (its density is 5.0 lb/ft³) and the balance by the tankage and cryogenic fluids.

The size of this cryogenic system will permit the inclusion of a superconducting solenoid with a length-to-diameter ratio of one half and a mean radius of 8.80 cm. The number of ampere-turns required to produce the required 15 kilogauss field at the outer radius of the generator ($r_o = 3.75$ cm) may be determined by reference to Figure 1 of Reference 4. For the radius ratio of $3.75/8.80 = .426$

$$\frac{4B_z}{\mu (NI/L)} = 1.96 \quad (\text{Figure 1 of Ref. 4})$$

and the number of ampere-turns required is $(2.15) 10^5$. For an assumed current density of 10^5 amp/cm² in the superconducting coil, the required radial thickness of the coil is 0.244 cm.

When producing the magnetic field required at the interior of the solenoid, the coil itself is exposed to a 21.9 kilogauss field (again this determination was made by reference to Figure 1 of Ref. 4). This is still a rather conservative field for a Nb_3Sn superconductor. At a temperature of 4.2°K (He boiling point) and a current density of 10^5 amp/cm², the critical field of niobium tin is approximately 100 kilogauss (Reference 5). Thus the application of fields greater than the 15 kilogauss assumed could be applied to the generator for improved performance.

In conclusion, the superconducting magnet system is the lightest of the three types considered, if the required period of dormancy does not exceed three months. The electromagnet is smaller and lighter than the permanent magnet without regard for the source of its power. A self-excited electromagnet generator system will probably be comparable in weight to a permanent-magnet generator system. Furthermore the heat rejection requirements of the electromagnet may pose a serious problem.

6.0 NUMERICAL SIMULATION OF THE VORTEX MHD GENERATOR

As an aid in evaluating the parameters affecting the operation of the vortex MHD generator and in determining overall generator performance, two computer programs have been written. The first of these computes the dependence of temperature on pressure in an isentropic nozzle process. This program has been employed to determine real gas effects in the driving gas as it passes from a combustion chamber through the inlet nozzle of a vortex chamber. The other program simulates the interrelationship between the temperature and the velocity components, considered as functions of radial distance from the axis to the vortex chamber. For economy of programming, both of these programs use the same main routine and (Runge-Kutta) integration subroutine. They differ only in the evaluation subroutines that supply values of the derivatives of the dependent variables being integrated. When appropriately signaled by the main routine, the evaluation subroutines also handle input and output of the quantities with which they are involved.

The two computer programs are designed to be used as follows:

- (1) The conditions describing the plasma in a supply plenum or in a combustion chamber (after burning) serve as input to the nozzle program.
- (2) The nozzle program computes the gas temperature after expansion through the nozzle for each of several possible nozzle discharge pressures.
- (3) An inlet pressure-temperature combination is selected which is expected to yield good generator performance.
- (4) The conditions describing the gas at the nozzle exit are determined; these serve as input for a possible calculation of the effect of drag reduction due to viscous shear losses at the outer cylindrical surface of the vortex chamber.
- (5) The conditions describing the gas at the effective outer radius of the vortex are calculated; they serve as input to the vortex simulation program, along with assumed initial values for the first-order radial derivatives of the dependent variables.
- (6) The vortex program computes the values of the temperature and components of velocity at the inner radius of the vortex, for several sets of assumed initial values of the derivatives.

- (7) A set of initial values is selected which matches flow conditions for the inner (gas discharge) region of the vortex.
- (8) The vortex program recomputes the desired case as finely as desired, yielding electric field values as a function of the radial distance.
- (9) The electric field is integrated numerically to find the generated output voltage.
- (10) The output power is obtained as the product of the current (an input constant) and the voltage.
- (11) A load curve (power vs. current) can then be determined by repeating the appropriate steps above a sufficient number of times.

6.1 Basic Equations and Assumptions The calculations performed by the program include real gas effects (assuming equilibrium conditions prevail) and are based on the differential conservation equations for momentum, angular momentum and energy in compressible vortex flow:

$$\rho u \frac{du}{dr} - \rho \frac{v^2}{r} = (2\mu + \lambda) \left(\frac{d^2 u}{dr^2} + \frac{1}{r} \frac{du}{dr} - \frac{u}{r^2} \right) - \frac{dp}{dr} - C_f \frac{\rho u |u|}{z} + j_\theta B \quad (1A)$$

$$\rho u \left(\frac{dv}{dr} + \frac{v}{r} \right) = \mu \left(\frac{d^2 v}{dr^2} + \frac{1}{r} \frac{dv}{dr} - \frac{v}{r^2} \right) - C_f \frac{\rho v |v|}{z} - j_r B \quad (1B)$$

$$\rho u \frac{dh^\circ}{dr} = j_r E + k \left(\frac{d^2 T}{dr^2} + \frac{1}{r} \frac{dT}{dr} \right) + \mu \left[v \frac{d^2 v}{dr^2} + \frac{dv^2}{dr} - \frac{v}{r} \frac{dv}{dr} \right] + (2\mu + \lambda) \left[u \frac{d^2 u}{dr^2} + \left(\frac{du}{dr} \right)^2 \right] + (2\mu + 3\lambda) \left(\frac{u}{r} \frac{du}{dr} \right) + 2h(T_{aw} - T_{iw}) \quad (1C)$$

where μ and λ are the effective first and second coefficients of viscosity for turbulent flow and k is thermal conductivity; the other quantities are defined in what follows. It will be noted that this set of conservation equations includes terms to account for the effects of wall heat transfer (through the term involving the film coefficient h , the adiabatic wall temperature T_{aw} , and the internal wall temperature T_{iw}) and viscous drag on the sidewall surfaces (through the term which includes the drag coefficient C_f). In these equations, the stagnation enthalpy h° is given by

$$h^{\circ} = \frac{1}{\mathcal{M}} \left[\frac{9 - 4P}{2} RT + \left(\frac{5}{2} RT + I \right) \epsilon \right] + \frac{1}{2} (u^2 + v^2) \quad (2)$$

in which the degree of ionization ϵ is related to temperature T and pressure p through the Saha equation, and the other quantities are:

I = ionization potential of the seed gas

P = mole fraction of seed gas

\mathcal{M} = mean molecular weight of the gas mixture

R = universal gas constant

u = radial velocity

v = azimuthal velocity

Furthermore, the electric field E (which is radial due to assumed symmetries in the geometry) is related to the current density components j_r (radial) and j_{θ} (azimuthal) by the Ohm's Law equations

$$j_r = \frac{\sigma}{1 + (\omega \tau)^2} \left[E + vB + (\omega \tau) uB \right] \quad (3A)$$

$$j_{\theta} = \frac{\sigma}{1 + (\omega \tau)^2} \left[(\omega \tau) (E + vB) - uB \right] \quad (3B)$$

in which the local conductivity σ is a function of T, ϵ , and electron collision cross sections, the product $\omega \tau$ (ω = electron cyclotron frequency, τ = electron mean free time) depends on σ and the magnetic induction B (axial by symmetry). The total radial current I is a fixed arbitrary input parameter; j_r is obtained from $I = 2\pi r z j_r$, where z is the axial depth (a given quantity); E is obtained by solving (3A); and j_{θ} is found from (3B). In all the above formulas the pressure p is eliminated wherever it appears by the application of the equation of state $p = (1 + \epsilon) \rho RT / \mathcal{M}$, and ρ is then eliminated through the equation of continuity: rate of mass flow = $W = -2\pi \rho u r z$.

6.2 The Computer Program for Numerical Simulation of the Vortex MHD

Generator The result of combining the equations of the previous section is a set of three second-order differential equations for the three dependent variables u, v , and T as functions of the radial distance r . This set is reduced to a set of six first-order equations in $u, v, T, du/dr, dv/dr$, and dT/dr , which are

integrated by the computer program.

However, this program, as it was initially written, proved to be extremely unwieldy although apparently correct. A very small integration step size, typically $1/75$ or less of the radial distance $(r_o - r_i)$, and many trials of assumed initial values of the first-order radial derivatives of the dependent variables were required in order to proceed even a few steps before the integration process went out of bounds. This occurred because the second derivatives appeared only in terms of small relative magnitude and they could not be evaluated exactly. Any lack of precision or accuracy in these derivatives at a given step of the integration led to a larger error at the next step. The integration was badly unstable.

Consequently, the program was modified to yield an approximate solution by neglecting the viscous and internal heat conduction terms in the basic equations. The solution then became much more tractable and reasonably accurate for the type of generator (described in Section 6.3) wherein the plasma static temperature remains fairly uniform and the electrical interaction is great enough to cause the vortex flow to behave as in solid body rotation. The first condition reduces the chances for internal heat conduction and the latter reduces shearing deformation and hence viscous effects.

An improved programming procedure which includes these two effects was devised subsequently. It consists of integrating the basic equations as a set of first-order differential equations with the second radial derivatives of u , v , and T being obtained through numerical differentiation of the first derivatives and used in the viscous and internal heat conduction terms. However, this procedure was not developed in time to be incorporated into the results presented here. The analysis which follows constitutes the basis for the computer program actually employed in the present study. The computers employed were an IBM 7070 and IBM 1401.

For the approximate solution, the equations for two-dimensional flow are used, neglecting the viscosity and internal heat conductivity terms. The conservation equations for momentum, azimuthal and radial, and energy, are

$$\rho_u \frac{dv}{dr} + \rho_u \frac{v}{r} = -j_r B - \frac{C_f \rho_v |v|}{z}, \quad (4A)$$

$$\rho_u \frac{du}{dr} - \rho \frac{v^2}{r} = -\frac{dp}{dr} + j_\theta B - \frac{C_f \rho_u |u|}{z}, \quad (4B)$$

$$\begin{aligned} \rho_u \frac{R}{m} \left[\frac{9}{2} (1 - P) + \frac{5}{2} (P + \epsilon) \right] \frac{dT}{dr} + \rho_u \frac{R}{m} \frac{5}{2} T \frac{d\epsilon}{dr} + \rho_u \frac{1}{m} I \frac{d}{dr} \\ + \rho u^2 \frac{du}{dr} + \rho_{uv} \frac{dv}{dr} = j_r E - 2 \frac{\hbar^1}{z} (T_{aw} - T_{iw}). \end{aligned} \quad (4C)$$

The equations of continuity, state, and the Saha equation are

$$\rho_{ur} z = -\frac{W}{2\pi} = \text{constant} = Q, \quad (5)$$

$$\frac{p}{(1 + \epsilon)} \rho T = \frac{R}{m} = \text{constant}, \quad (6)$$

$$\frac{p \epsilon^2 e^{\frac{I}{RT}}}{(1 + \epsilon)(P - \epsilon) T^{5/2}} = \frac{2g^*}{g} \cdot \frac{(2\pi m_e)^{3/2} k^{5/2}}{\hbar^3} = \text{constant} = G. \quad (7)$$

The variables v , u , T are chosen as basic, dependent on r . Equations for dv/dr , du/dr , dT/dr are obtained by manipulating (4A) through (7).

Equation (5) is solved for:

$$\rho = \frac{Q}{urz}, \quad \frac{d\rho}{dr} = -\rho \left(\frac{1}{u} \frac{du}{dr} + \frac{1}{r} + \frac{1}{z} \frac{dz}{dr} \right). \quad (8)$$

Equation (6) becomes

$$\frac{\rho_{ur} z}{(1 + \epsilon) T} = \frac{R}{m} Q.$$

This is solved for p:

$$p = \frac{\frac{R}{M} Q (1 + \epsilon) T}{urz}, \quad \frac{dp}{dr} = p \left(\frac{1}{1 + \epsilon} \frac{d\epsilon}{dr} + \frac{1}{T} \frac{dT}{dr} + \frac{1}{\rho} \frac{d\rho}{dr} \right). \quad (9)$$

Equation (7) becomes

$$\frac{\epsilon^2 e^{\frac{I}{RT}}}{(P - \epsilon) urz T^{3/2}} = \frac{G}{\frac{R}{M} Q}, \quad \frac{\epsilon^2}{P - \epsilon} = \frac{G}{\frac{R}{M} Q} urz T^{3/2} e^{-\frac{I}{RT}} = Z.$$

This is solved for ϵ :

$$\begin{aligned} \epsilon &= -\frac{1}{2} Z + \sqrt{\frac{1}{4} Z^2 + PZ}, \quad \frac{d\epsilon}{dr} = \frac{P - \epsilon}{2\epsilon + Z} \frac{dZ}{dr} \\ &= \frac{(P - \epsilon) Z}{2\epsilon + Z} \left[\left(\frac{3}{2} + \frac{I}{RT} \right) \frac{1}{T} \frac{dT}{dr} - \frac{1}{\rho} \frac{d\rho}{dr} \right] \\ &= \frac{\epsilon(P - \epsilon)}{2P - \epsilon} \left[\left(\frac{3}{2} + \frac{I}{RT} \right) \frac{1}{T} \frac{dT}{dr} - \frac{1}{\rho} \frac{d\rho}{dr} \right] \end{aligned} \quad (10)$$

The conservation equations become

$$\rho u \frac{dv}{dr} + \rho u \frac{v}{r} = -j_r^B - \frac{C_f \rho v |v|}{z}, \quad (4A)$$

$$\begin{aligned} \rho u \frac{du}{dr} - \rho \frac{v^2}{r} &= -\frac{p}{1 + \epsilon} \frac{d\epsilon}{dr} - \frac{p}{T} \frac{dT}{dr} - \frac{p}{\rho} \frac{d\rho}{dr} + j_\theta^B - \frac{C_f \rho u |u|}{z} \\ &= -\left[\frac{p \epsilon (P - \epsilon)}{(1 + \epsilon)(2P - \epsilon)} \left(\frac{3}{2} + \frac{I}{RT} \right) + p \right] \frac{1}{T} \frac{dT}{dr} \\ &\quad - \left[\frac{p \epsilon (P - \epsilon)}{(1 + \epsilon)(2P - \epsilon)} - p \right] \left(\frac{1}{u} \frac{du}{dr} + \frac{1}{r} + \frac{1}{z} \frac{dz}{dr} \right) \\ &\quad + j_\theta^B - \frac{C_f \rho u |u|}{z}, \end{aligned} \quad (4B1)$$

$$\begin{aligned}
& \rho_u \frac{R}{m} \left[\frac{9}{2} (1 - P) + \frac{5}{2} (P + \epsilon) \right] \frac{dT}{dr} + \rho_u \frac{R}{m} \left(\frac{5}{2} + \frac{I}{RT} \right) T \frac{d\epsilon}{dr} + \rho_u^2 \frac{du}{dr} + \rho_{uv} \frac{dv}{dr} \\
& = \rho_u \frac{R}{m} \left[\frac{9}{2} (1 - P) + \frac{5}{2} (P + \epsilon) + \left(\frac{5}{2} + \frac{I}{RT} \right) \frac{\epsilon (P - \epsilon)}{2P - \epsilon} \left(\frac{3}{2} + \frac{I}{RT} \right) \right] \frac{dT}{dr} \\
& + \rho_u \left[\frac{R}{m} \left(\frac{5}{2} + \frac{I}{RT} \right) T \frac{\epsilon (P - \epsilon)}{2P - \epsilon} \frac{1}{u} + u \right] \frac{du}{dr} + \rho_{uv} \frac{dv}{dr} \\
& + \rho_u \frac{R}{m} \left(\frac{5}{2} + \frac{I}{RT} \right) T \frac{\epsilon (P - \epsilon)}{2P - \epsilon} \left(\frac{1}{r} + \frac{1}{z} \frac{dz}{dr} \right) \\
& = j_r E - 2h \frac{1}{z} (T_{aw} - T_{iw}) .
\end{aligned} \tag{4C1}$$

When simplified to the case $C_f = B = E = \epsilon = P = 0$, equations (4A), (4B1), (4C1) become

$$\rho_u \frac{dv}{dr} + \rho_u \frac{v}{r} = 0 , \tag{4A'}$$

$$\rho_u \frac{du}{dr} - \rho \frac{v^2}{r} = -p \left(\frac{1}{T} \frac{dT}{dr} - \frac{1}{u} \frac{du}{dr} - \frac{1}{r} \right) , \tag{4B1'}$$

$$\rho_u \frac{R}{m} \cdot \frac{9}{2} \frac{dT}{dr} + \rho_u \left(u \frac{du}{dr} + v \frac{dv}{dr} \right) = 0 . \tag{4C1'}$$

The magnitudes of the coefficients are approximately such that the terms $\rho_u \frac{du}{dr}$ and $-p \frac{1}{T} \frac{dT}{dr}$ in (4B1') and $\rho_u^2 \frac{du}{dr}$ in (4C1') are negligibly small or nearly so. These terms should not be made pivotal in the solution. This is avoided by solving (4C1') for $\frac{dT}{dr}$ and substituting the resulting expression into (4B1'). Then the values of dv/dr , du/dr , dT/dr are found from (4A'), (4B1'), (4C1') in that order. The same scheme is used in the more general case.

Solving (4C1) for $\frac{dT}{dr}$ gives

$$\frac{dT}{dr} = \frac{j_r E - 2h \frac{1}{z} (T_{aw} - T_{iw})}{\rho_u D} - \frac{(AT \frac{1}{u} + u) \frac{du}{dr} + v \frac{dv}{dr} + AT \left(\frac{1}{r} + \frac{1}{z} \frac{dz}{dr} \right)}{D} , \tag{11}$$

$$D = \frac{R}{M} \left[\frac{9}{2} (1 - P) + \frac{5}{2} (P + \epsilon) \right] + A \left(\frac{3}{2} + \frac{I}{RT} \right),$$

$$A = \frac{R}{M} \left(\frac{5}{2} + \frac{I}{RT} \right) \frac{\epsilon (P - \epsilon)}{2P - \epsilon}.$$

Substitution into (4B1) results in

$$\begin{aligned} \rho u \frac{du}{dr} - \rho \frac{v^2}{r} = & - \left[p^F \left(\frac{3}{2} + \frac{I}{RT} \right) + p \right] \frac{1}{T} \cdot \frac{j_r^E - H}{\rho u D} + j_\theta^B - \frac{C_f \rho u |u|}{z} \\ & + \left\{ \left[p^F \left(\frac{3}{2} + \frac{I}{RT} \right) + p \right] \frac{1}{T} \cdot \frac{AT \frac{1}{u} + u}{D} - (p^F - p) \frac{1}{u} \right\} \frac{du}{dr} \\ & + \left[p^F \left(\frac{3}{2} + \frac{I}{RT} \right) + p \right] \frac{1}{T} \cdot \frac{v}{D} \frac{dv}{dr} \\ & + \left\{ \left[p^F \left(\frac{3}{2} + \frac{I}{RT} \right) + p \right] \frac{1}{T} \cdot \frac{AT}{D} - (p^F - p) \right\} \left(\frac{1}{r} + \frac{1}{z} \frac{dz}{dr} \right), \\ F = & \frac{\epsilon (P - \epsilon)}{(1 + \epsilon)(2P - \epsilon)}, \end{aligned} \quad (4B2)$$

$$H = 2h_z^1 (T_{aw} - T_{iw}).$$

Dividing equation (4B2) by p and solving for du/dr gives

$$\frac{du}{dr} = - \frac{J(j_r^E - H)}{T \rho u D S} + \frac{j_\theta^B - \frac{C_f \rho u |u|}{z}}{p S} + \frac{J v}{T D S} \frac{dv}{dr} + \left(\frac{J A}{D S} - \frac{L}{S} \right) \left(\frac{1}{r} + \frac{1}{z} \frac{dz}{dr} \right) + \frac{\rho v^2}{r p S}, \quad (12)$$

$$S = \frac{\rho u}{p} - \frac{J(AT \frac{1}{u} + u)}{T D} + L \frac{1}{u},$$

$$J = F \left(\frac{3}{2} + \frac{I}{RT} \right) + 1,$$

$$L = F - 1.$$

Finally, solving (4A) for $\frac{dv}{dr}$ gives

$$\frac{dv}{dr} = -\frac{j_r B}{\rho u} - \frac{C_f v |v|}{zu} - \frac{v}{r} . \quad (13)$$

Evaluation of (13), (12), (11) in sequence permits numerical integration of the differential equations using a standard method such as Runge Kutta. The application of this computer program is demonstrated in the example of an open cycle vortex MHD generator to follow.

6.3 Example of Computed Generator Performance An example will serve to indicate both the application of the numerical simulation program and the performance to be expected from a vortex MHD generator. A chemically-fueled open cycle system was selected as being appropriate for the example because of its suitability for the short term power applications described in Section 7.1.

A possible arrangement of the vortex generator components in a power system package is illustrated in Figure 6-1. By employing high-temperature producing non-hydrocarbon fuels (e.g., cyanogen/oxygen) high power densities can be achieved with the moderate magnetic fields provided by permanent magnets. Component temperatures can be controlled by regenerative cooling supplied by both the fuel and oxidizer.

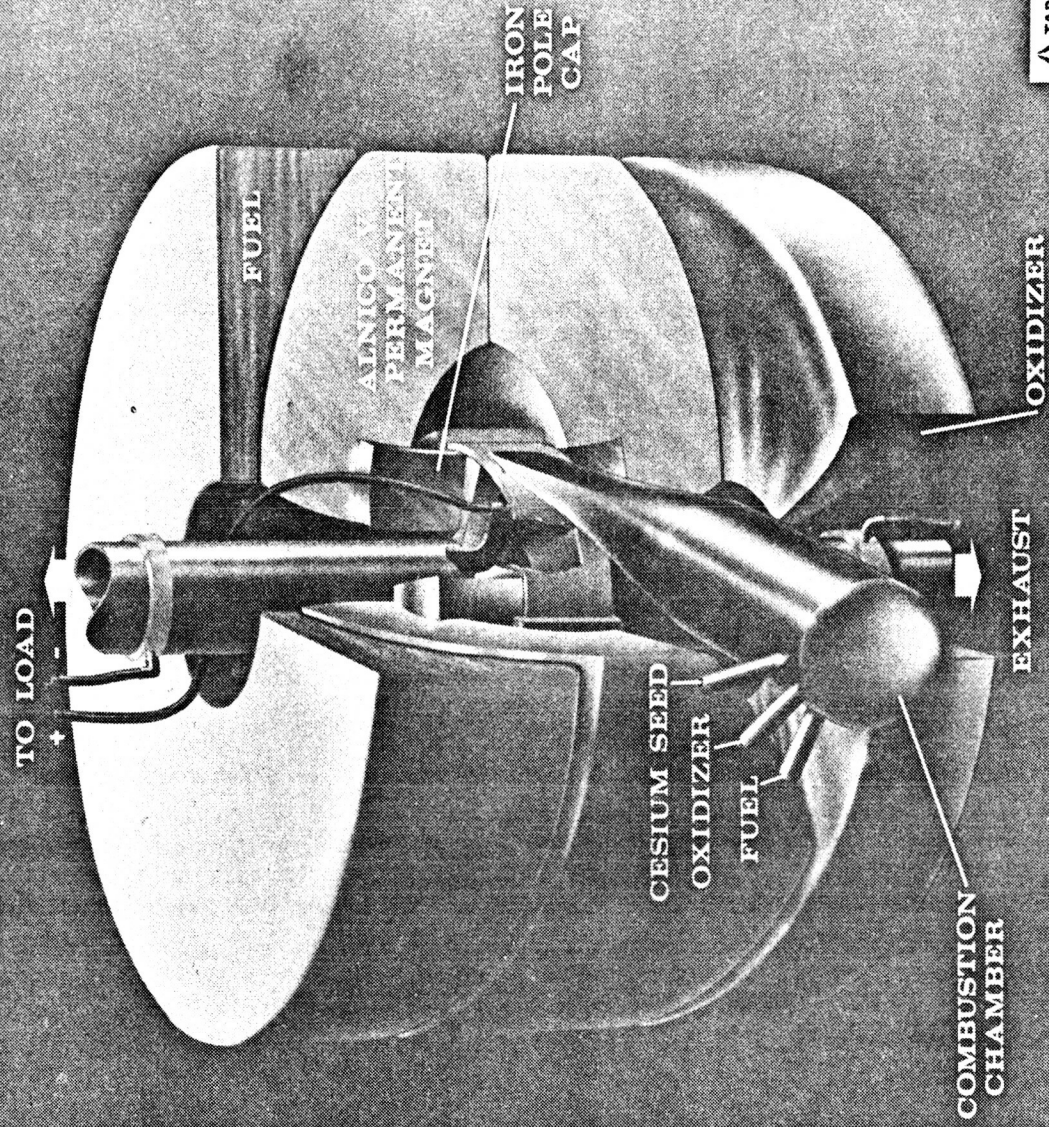
Relatively high electrical conductivity is obtained from these high temperature combustion products when they are seeded with a small percentage of an easily ionized substance such as cesium. The direct result is a high power density (per unit volume of magnetic field region) which minimizes both the heat transfer loss and the required magnet weight and volume.

The various considerations necessary to the determination of performance are delineated in the following example.

The example selected is a low power MHD generator suitable for space applications which may require long periods of dormancy before being required to deliver power, either in a single burst or intermittently. The descriptive phrase "low power MHD generator" is used here in the sense that the power level calculated for this example is at the extreme low end of the power range thought feasible

**10 KW
VORTEX
MHD
POWER
GENERATOR**

Figure 6-1



for MHD generators. The values of performance, efficiency and power density quoted for this example, therefore, represent lower limits to what can be expected from vortex MHD generators of greater output. The various assumptions employed in the calculation are described in Table 6-1.

TABLE 6-1
Example of Computed Generator Performance;
Assumption of Calculation

<u>Assumption</u>	<u>Remarks</u>
Fuel: cyanogen and oxygen in stoichiometric proportions	
Seed: liquid cesium	
$W = 10 \text{ gm sec}^{-1}$	Total propellant flow rate.
$P = 0.1$	Seed concentration. The results of a study (Ref. 1) of linear MHD generators utilizing the above fuel and seed indicate that $P = 0.1$ is about optimum.
$p_o^o = 1 \text{ atm}$	Stagnation inlet pressure. This value was selected to give a reasonable compromise between excessive heat transfer due to high pressure and excessive Hall effects due to low pressure.
$T_o^o = 4400 \text{ }^\circ\text{K}$	Stagnation inlet temperature. The analysis of Ref. 2 indicates that at $P = 0.1$ and $p_o^o = 1 \text{ atm}$, the resulting seeded combustion gases have the temperature indicated.
$r_o = 3.75 \text{ cm}$	Outer effective radius of chamber.
$r_i = 1.87 \text{ cm}$	Inner radius of chamber at exhaust outlet.
$z = 1.0 \text{ cm and constant}$	Depth of vortex chamber.

$$M_o = 0.75, 90, 1.20$$

Mach number (tangential component) of driving jets. These values were tested in a search for the optimum which maximizes power output when considering the opposite trends of velocity and conductivity in an expansion process.

$$B = 15,000 \text{ gauss and constant}$$

Magnetic field.

$$T_{iw} = 2500^\circ K$$

Temperature of inside surface of sidewall. This value is adequate with regard to material considerations (Section 4.2), heat loss, and maintenance of negligible sidewall electrical shorting.

$$Q_{es} = (1.3) 10^{-14} \text{ cm}^2$$

Electron - neutral seed particle elastic cross-section. Ref. 3.

$$Q_{en} = (0.883) 10^{-15} \text{ cm}^2$$

Electron - neutral combustion gas elastic cross-section. This is a concentration weighted value derived from $Q_{en}(\text{CO}) = 10^{-15} \text{ cm}^2$ and $Q_{en}(\text{N}_2) = (0.65) 10^{-15} \text{ cm}^2$ at a mean gas temperature = 4000 °K. Ref. 4.

Gas Model: Real gas effects are included except for the following assumptions. The plasma is assumed to consist of CO, N₂, and Cs with both dissociation and electronic excitation above ground state neglected for all species. It is also assumed that the CO and N₂ are fully excited in vibration and rotation.

Viscous Effects on Outer Cylindrical Wall (Electrode): The analysis of generator performance requires the determination of the tangential velocity, v_o , which is effective in maintaining the vortex flow. This velocity need not be identical to the nozzle discharge velocity because of the turbulent wall shear and internal fluid torque. The average skin friction coefficient (c_{fw}) for the shear on the outer wall, based on the following torque balance equation

$$\frac{W}{L} (v_n - v_o) r_o = c_{fw} \frac{\rho_o v_o^2}{2} 2\pi r_w^2 + E \left(\frac{dv}{dr} - \frac{v}{r} \right) 2\pi r_o^2 ,$$

(Driving torque = Wall shear torque + Internal fluid torque)

can be correlated by $c_{fw} = 0.35 \text{ Re}_v^{-0.27}$ for the series of vortex experiments described in Reference 5. This correlation unfortunately does not take into account the radial pressure gradient through which the jet traverses before the recovered jet velocity (v_o) is established. The ratio $v_o/v_n = 0.9$ when calculated on the above basis for the present example with $M_o = 0.9$ and assuming solid body rotation (i.e., zero internal fluid torque). This value is indicative of the increased overall nozzle expansion ratio required to overcome the viscous wall loss. The radial pressure gradient at the effective outer radius must be considered also as it effects that portion on the initial expansion which must exist within the nozzle itself. The influence of the viscous wall loss on overall generator performance is thus expected to be negligible in the present example; its primary effect will be a slight upward adjustment in the combustor pressure.

Internal Heat Transfer and Viscous Effects: These two effects are assumed to be negligible in this example for the reasons stated previously in Section 6.2.

Sidewall Boundary Layer Flow: The sidewall boundary layer radial flow was not a consideration in the present computer analysis. The magnitude of this radial flow can assume significant proportions, however, in a generator of low aspect ratio, such as in the present example. An analysis due to Mack⁶ can be employed to estimate the ratio of radial flow in the boundary layer to the total mass flow. For example, at the conditions of operation corresponding to the case where $M_o = 0.9$, $z/r_o = 0.266$, and $I = 287$ amp. we find that the tangential velocity distribution is nearly solid-body rotation, thus Figures 1 and 28 of Reference 6 indicate that 13% of the total mass flow exists as radial flow in each sidewall boundary layer. At a higher current density, $I = 430$ amp, the velocity distribution changes to one which can be described by the equation $v/v_o = (r/r_o)^{-4}$ and the radial flow in each boundary layer reduces to 4% of the total flow. These estimates may be considered also as upper limits in as much as the radial pressure gradients which produce the secondary flow are less strong

in a power generating vortex than in a purely hydrodynamic vortex for the same power-law tangential velocity distribution; and it was the latter case which was considered in Reference 6.

These results lead to the conclusion that the magnitude of the boundary layer flow can be held to an acceptable minimum by the proper selection of generator parameters, primarily the aspect ratio and the generator load coefficient (which affects the tangential velocity distribution).

Matching Condition at Fluid Exhaust Boundary: The calculation of fluid flow in the vortex power producing region assumes that the values of fluid velocity and pressure can be matched at the discharge radius (r_1) by the flow in the inner discharge region of the vortex. The velocity distribution within this inner flow, given by Equation 10 of Appendix C, and the pressure distribution based thereon may be used in the calculation of an exhaust restriction required for the matching condition. For present purposes it is sufficient to insure that flow choking does not occur at the discharge orifices.

Auxiliary Equations:

Electrical Conductivity:

$$\sigma = 0.85 \frac{e^2}{m_e} \sqrt{\frac{\pi m_e}{8k}} \frac{\epsilon}{\sqrt{T} \left((1-P) Q_{en} + (P-\epsilon) Q_{es} + \epsilon Q_{ei} \right)} \text{Ref.7}$$

$$\text{where } Q_{ei} = \frac{0.45}{T^2} \left(\frac{e^2}{k} \right)^2 \left\{ \ln \frac{1.125 k^4}{e^6 \pi} + \ln \frac{T^4}{P \epsilon} \right\} \text{Ref.7}$$

Hall Coefficient:

$$\omega (= \omega \tau) = \frac{e}{n_o m_e} \sqrt{\frac{\pi m_e}{8k}} \frac{B}{\sqrt{T} \left((1-P) Q_{en} + (P-\epsilon) Q_{es} + \epsilon Q_{ei} \right)}$$

Specific Heat:

$$c_p = R \left\{ \frac{9-4P}{2} + \frac{5\epsilon}{2} + \left(\frac{5}{2} T + \frac{I}{R} \right) \left[\frac{\epsilon}{T} \left(\frac{I}{RT} + \frac{5}{2} \right) \left\{ \frac{(\epsilon+1)(P-\epsilon)}{2P-\epsilon(1-P)} \right\} \right] \right\}$$

Molecular Viscosity:

$$\mu = (2.6693) 10^{-5} \frac{\sqrt{T M}}{\sigma^2} f\left(\frac{kT}{\epsilon}\right) \text{ gm cm}^{-1} \text{ sec}^{-1} \quad \text{Ref.8}$$

where σ and ϵ/k are the force constants in Å and °K respectively.

Thermal Conductivity:

$$k = \frac{\mu}{M} (c_p + \frac{5}{4} R), \text{ which is Eucken's relation.} \quad \text{Ref.8}$$

Sidewall Friction Coefficient:

$$C_f = \left[1 + 2.5(z/r_o) \right] \left\{ 0.1 \text{Re}_{zv}^{-0.3} + (1.4) 10^{-3} \right\} \quad \text{Ref.9}$$

for $\text{Re}_{zv} < 6 \times 10^5$

$$\text{where } \text{Re}_{zv} = \frac{2(zv\rho)_o}{\mu_o}$$

Sidewall Mean Heat Transfer Coefficient:

$$h = \frac{0.0157 \text{Pr} k (\omega/\nu)^{0.8} r_w^{0.6}}{1 + 2.035 (\nu/\omega)^{0.1} r_w^{-0.2} (\text{Pr} - 1)} , \quad \frac{\text{erg}}{\text{cm}^2 \text{sec } ^\circ\text{K}} \quad \text{Ref.10}$$

$$\text{where } \omega = v_o/r_o$$

$$\nu = \mu_o/\rho_o$$

A summary of computer results is given in Table 6-2 for several different values of driving-jet Mach numbers, total current flow, and for the two possible relative orientations of magnetic field and tangential velocity vectors. Radial inflow is assumed throughout.

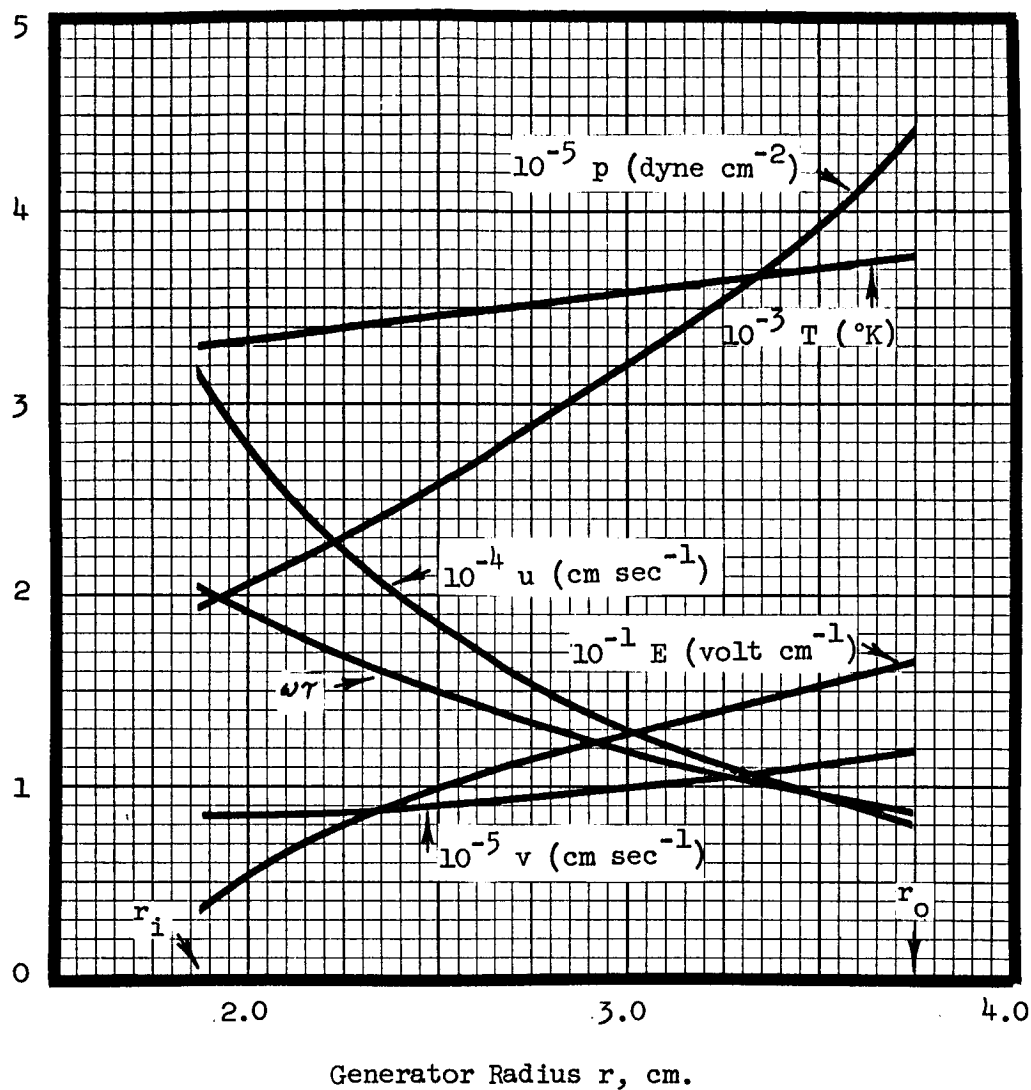
TABLE 6-2
Comparison of Calculated Power Output

	<u>$M_o = 0.70$</u>	<u>0.90</u>	<u>1.20</u>
High Current, I - 430 amp.			
Outer electrode cathode	2.58 KW	3.18 KW	---
Inner electrode cathode	---	3.92 KW	5.84 KW
Low Current, I = 287 amp.			
Outer electrode cathode	2.95 KW	3.40 KW	---
Inner electrode cathode	---	4.81 KW	6.03 KW

The advantage of orienting the magnetic field with respect to the tangential flow direction so as to provide for a radial inflow of current is clearly obvious from the comparison of results at $M_o = 0.90$. By this means the Hall effects are minimized as discussed in Section 3.3.7.

Although only two levels of current for each of three different Mach numbers were investigated, the selection apparently resulted in near optimum conditions, that is maximum power output for each value of assumed inlet Mach number. A trend of increasing power output with increasing Mach number was also obtained but it is not clear whether the optimum Mach number is contained within or without the range studied. An optimum can be anticipated as the increased Mach number results in a lower plasma temperature and hence conductivity which is not offset by the contributions of velocity to power density.

Of the several sets of generator operating conditions studied, that which indicated the best performance will be employed in the calculations to follow. The radial distribution of variables for this case are illustrated in Figure 6-2. The primary features of this case are a power output of 6.03 KW at a terminal voltage of 21.0 volts, an energy efficiency (elect. power out/chem. power in) of 14.7 per cent, and a propellant flow rate of 13.1 lb/kw-hr. It should be noted



$$M_o = 1.20, u_o/v_o = 0.0674, z = 1.0 \text{ cm}$$

$$W = 10 \text{ gm sec}^{-1}, P = 0.1, B = 15,000 \text{ gauss}$$

$$V = \int_{r_i}^{r_o} E \, dr = 21 \text{ volts}, I = 287 \text{ amp}, \text{Power} = 6.03 \text{ kw}$$

Radial Inflow; Cathode at Inner Electrode

Vortex MHD Generator, Radial Distribution of Variables

Figure 6-2

that one third of this propellant flow rate is due to the cesium seed; it is also quite probable that the seed concentration (10 molal per cent) could be reduced substantially without a significant decrease in power output for a net increase in system power density. Additional computer runs would be required to determine the extent of this trend.

The total heat transfer from both sidewalls for this particular example can be determined from the calculated sidewall mean heat transfer film coefficient ($h = (2.23) 10^5 \text{ erg cm}^{-2} \text{ sec}/^\circ\text{K}$), the wall inside surface temperature (2500°K), and the adiabatic wall temperature averaged over the sidewall between the outer and inner radii (r_o and r_i). The computer output indicated that T_{aw} varied in a nearly linear relationship with radius from $T_{aw} = 4264^\circ\text{K}$ at r_o to 3570°K at r_i . The average value was 3900°K . The corresponding heat loss from both sidewalls was thus 2.06 kw.

This magnitude of heat loss is at an acceptable level with respect to the regenerative cooling capacity of the fuel and oxidizer. The regenerative cooling capacity was calculated on the basis of the propellant supply rate and assuming that the latent heat of vaporization and sensible heating to 100°C for both fuel and oxidizer are available as a heat sink. This amounts to 1.2 kw for the oxidizer and 4.1 kw for the fuel for a total regenerative cooling ability of 5.3 kw.

To complete the analysis of generator performance the thicknesses of the ceramic sidewalls must be determined since they partially determine the minimum magnet gap and hence magnet weight. The heat loss mentioned above corresponds to a heat flux of $7.45 \text{ cal sec}^{-1} \text{ cm}^{-2}$. At this heat flux the thickness of a strontium zirconate electrical insulator, operating between surface temperatures of 2500°K and 2100°K , with a mean thermal conductivity over this range of $(5.5)10^{-3} \text{ cal sec}^{-1} \text{ cm}^{-1}/^\circ\text{K}$ (11), is $\ell_e = 0.295 \text{ cm}$. This value exceeds the one hour erosion calculated in Section 4.2 for the $\text{SrO} \cdot \text{ZrO}_2$ insulator. The inside surface temperature was limited to 2500°K in this example so as to prevent excessive erosion and to eliminate electrical shorting of the generator output by sidewall conduction. At 2500°K , the resistivity of $\text{SrO} \cdot \text{ZrO}_2$ is 10 ohm-cm (11) and insulator conduction at this resistivity level is negligible.

Thermal insulation was assumed to be provided by zirconium oxide, operated between surface temperatures of 2100°K and 1170°K. Over this temperature range the high density (350 lb/ft³), four per cent CaO stabilized ZrO₂ has a value of thermal conductivity of $(2.75)10^{-3}$ cal sec⁻¹cm⁻¹/°K (11). The thickness of ZrO₂ required for the heat flux mentioned above is $\ell_t = 0.343$ cm. The zirconia exterior surface temperature of 1170°K corresponds to a maximum permissible value with respect to the Curie point of the adjacent magnet Permendur pole piece.

A determination of the minimum magnet gap is now possible. It is equal to the sum of the generator depth (1.0 cm) plus the thicknesses of the electrical and thermal insulators on each side of the vortex cavity ($2\ell_e + 2\ell_t$). The resulting minimum magnet gap is thus 2.276 cm. Magnet system calculations, based on this gap dimension plus the inner and outer radius of the generator volume over which a 15,000 gauss field was assumed to exist, were presented in Section 5.

A summary of those results, as applied to the present example, is given in the following table.

Table 6-3

Summary of Power and Weight Characteristics of Vortex Generator Example

	<u>Permanent Magnet</u>	<u>Electromagnet</u>	<u>Superconducting Magnet (3 Month Dormancy)</u>
Gross Power, kw	6.03	6.03	6.03
Net Power, kw	6.03	3.63	6.03
Weight, lb	149	55	44

Scaling to the Examples of Section 7.2 The analysis of the present example can be scaled to determine the performance of the 10 kw-20 min. and 50 kw-60 min. vortex MHD generators discussed in Section 7.2. An extremely conservative estimate can be obtained by assuming no change in power density (per unit volume of vortex cavity) or conversion efficiency as the 6 kw generator is scaled upward. This assumes no improvement due to the surface area-volume relationship, whereas the heat transfer and sidewall drag should actually decrease in relative magnitude, nor any further attempt at determining optimum geometry such as radius ratio or axial depth variation and optimum operating conditions. The computer analysis of generator performance, summarized in Table 6-2, actually provides

little more than a single point in a performance map or parametric analysis of the generator that would be required to determine the optimum performance possible. The following conservative estimate will however reflect the improved magnet-generator relationship possible since, for constant sidewall insulation thickness, the vortex cavity occupies an increasing proportion of the magnet gap. The vortex cavity volume can be increased by the ratio of power levels if the outer radius and axial depth are each increased by the cube root of the power ratio, assuming that the generator radius ratio remains constant. The resulting permanent magnets weight estimates, with appropriate adjustments in the leakage coefficients (which decreased slightly), are 163 lb. and 723 lb. respectively for the 10 kw and 50 kw applications. The total system weights (i.e., permanent magnet plus fuel) are therefore 205 lb. and 1380 lbs. with the specific propellant consumption 13.1 lb/kw-hr assumed constant. Corresponding system weight estimates for the generators with superconducting field magnets are 60 lb. and 750 lbs. for an assumed dormancy period of three months.

These weight estimates must be considered, therefore, as upper limits; significant reductions can be expected by optimizing. On the basis of the limited results of the computer analysis, it appears that very substantial improvements in generator efficiency and power density can be achieved by optimizing. The following changes or considerations can be recommended.

- a) increase M_0 from 1.2 to 1.5 for an estimated gain in power density of 27 per cent.
- b) increase operating pressure level to reduce Hall effects.
- c) increase u/v ratio to reduce Hall effects.
- d) increase generator axial depth with decreasing radius to suppress Hall currents.
- e) utilize the fringing field of the magnet.
- f) increase magnetic flux density. This is most appropriate if a superconducting magnet is employed.
- g) alter the seed concentration to maximize total system power density.
- h) consider the improvements due to a better surface area-volume ratio at higher power output levels.

7.0 VORTEX MHD GENERATOR APPLICATIONS; COMPARISON WITH OTHER SYSTEMS

7.1 Applications The general areas of applicability of MHD methods of energy conversion depend, first of all, upon whether an open or closed-cycle system is selected. This choice is clearly dictated by the requirements of the particular mission in terms of power level and duration of output required.

Open-cycle MHD conversion systems in general will employ a combustion energy source which provides a high temperature, high velocity gas stream similar to a rocket exhaust. With such combustion sources, the exhaust products themselves become the working fluid in the MHD generator. Typically this gas stream has a static temperature of 3000°K and a velocity of 1000 meters/sec. In addition to the conventional combustion products, an alkali metal compound is added for seed purposes. The appropriate cycle is a direct one in which the combustion products flow through the generator section and then are exhausted overboard. The cycle performance is dependent directly upon the upper temperature in the combustion process and the lowest exit temperature at which acceptable conductivity can be obtained.

Open-cycle MHD conversion systems require a continuous consumption of the working fluid or propellant. Since for a given continuous power output level this propellant weight is a linear (increasing) function of the duration of power delivery, there will exist an operating time beyond which the weight becomes excessive and a closed-cycle approach becomes advantageous. It is believed that operating times which require excessive propellant weights will prove to be the ultimate limitation on open-cycle MHD systems. Combustion fired experimental MHD generators have been operated for times of thirty minutes; it is expected that these times can be increased by several orders of magnitude through use of additional cooling and by operation at lower temperature provided the gas conductivity can be maintained sufficiently high. By these methods sufficient lifetime is expected to be obtained up to the logical limits of open-cycle systems.

This fuel-weight limitation to applicability is by no means unique to open-cycle MHD conversion methods but confronts other methods as well. In order to make a realistic evaluation of open-cycle MHD power conversion, a reasonable operating time must be chosen; we arbitrarily will limit ourselves to operating times of an hour or less. This limitation may be the result of materials degradation, a

specific fuel consumption rate which dictates the choice of another type system after a particular operating time, or a combination of these and other factors. Whatever the reason for the limitation, the open-cycle MHD converters must have a mission for which their use is logical. Recognizing that in all probability the maximum running time for an efficient (high temperature) open-cycle MHD unit will be somewhat less than for fuel cell or turboalternator systems, the question then becomes a matter of finding missions for which "high" power is required for "brief" durations. The particular level of power and exact duration are, for the moment, undefined but of particular interest are powers in excess of 10 kw for times less than an hour, the probable range of feasibility for open-cycle MHD generators.

Power requirements of this nature are somewhat difficult to find documented, but the need becomes apparent after a little reflection upon possible space missions. The increasing level of ambition to be found in nearly all projected missions, including manned and unmanned, military and scientific, will necessitate ever-increasing on-board electrical power capability. This becomes particularly obvious in the case of deep space (planetary) probes where it may become desirable to have rapid vehicle control by earth commands; this in turn demands "real time" high-rate data transmission from vehicle to earth so that the transmitted information may be interpreted, judgments made, and earth commands sent in minimum time. Another similar area is near-earth missions involving several men. Here again future power demands will be dictated by a combination of vehicle size, crew size, scientific tasks, repair capability, backup emergency power, etc.

An attempt has been made to compile a more specific listing of needs for "high output, short term" electrical power. In most cases, however, these needs do not apply to authorized (funded) programs; consequently no quantitative requirements are available. This listing includes:

1. Manned Orbiting Space Stations, for
 - a) general emergency power
 - b) docking and rendezvous power (no reactor power available)
 - c) repair power
 - d) guidance and attitude control power
 - e) fuel transfer (pumping) power

2. Extra-terrestrial Base Power, for
 - a) emergency and repair
 - b) communications
 - c) collector and/or radiator deployment
3. General Vehicle Power, for
 - a) recoverable boosters
 - b) redundant (emergency) power (for communications, life support, etc.)
 - c) re-entry communications
 - d) startup power for closed cycle power systems (e.g., for control, or radiator pre-heat)
 - e) docking and rendezvous
 - f) deployment of "foldable" structures (radiators, collectors, antennas)
 - g) parawing deployment
4. Excursion Vehicle Power, for
 - a) ground support (rock drilling and sample gathering)
 - b) antenna or collector erection and/or deployment
5. Long Distance Communications Power, for
 - a) optical (laser) communications power
 - b) "real-time" data transmission (direct broadcast without information storage or re-transmission)
 - c) long distance, high resolution television transmission
 - d) margin for communications through natural and artificial radiation belts (unknown scattering effects)

This last area, long distance communications, is of particular interest for high output, short term power. In the case of a scientific probe to one of the planets, only small quantities of electrical power would be required during the several months or more of flight. Once in the immediate vicinity of the target, however, it might prove highly advantageous to have a large power capability available so that "direct" information could be obtained. This leads in turn to the requirement for a "dormant" power system which becomes activated upon the demand for data transmission. The MHD power generator should be ideally suited for missions of this type.

One may visualize a Mars mission, for example, where a soft-landing of a scientific payload containing a television camera is desired. After several months

of dormancy the power system becomes operative such that data is sent to earth during the penetration of the Martian atmosphere. It might happen, for example, that a retro-rocket failure makes a hard landing imminent, with doubtful survival of the payload, so that maximum data acquisition and transmission is desired in the shortest possible time. Under such circumstances an MHD generator system would serve to "salvage" the mission with the ability to return a wealth of data including direct television pictures of the Martian landscape prior to impact. It is axiomatic that the probability of mission success decreases with increasing mission time; a "burst" power capability would provide missions of this type with a highly worthwhile degree of flexibility and redundancy.

The level of power required for this type of effort depends upon a variety of factors including transmission distance, information quality (resolution), and data rate. An estimate of the required powers may be taken from a recent paper by Welles (1). Table 7-1 lists some of his data showing the required power for data transmission from several planets for three data rates. Welles "assumes an 8-ft. diameter steerable dish antenna on the probe" and "a transmitter efficiency of ten per cent, and the use of Deep Space Instrumentation Facilities for earth reception".

Table 7-1
Interplanetary Communication Power Requirements

From (Source)	at (Rate)	requires (Power, watts)
Moon	1000 Bits/sec.	10^{-3}
	1 TV frame/sec.	10^{-1}
Mars or Venus	10 Bits/sec.	5
	1000 Bits/sec.	2×10^2
	1 TV frame/sec.	5×10^4
Jupiter	10 Bits/sec.	20
	1000 Bits/sec.	2×10^3
	1 TV frame/sec.	5×10^5
Pluto	10 Bits/sec.	10^3
	1000 Bits/sec.	10^5
	1 TV frame/sec.	2×10^7

These power levels are only approximations based on Welles' graph (e.g., Mars and Venus are "equidistant" from earth) but should serve to indicate the scope of the problem. The exact number of TV frames/sec. which constitute "direct" broadcasting of acceptable resolution, or the number of simultaneous channels of data transmission desired must yet be defined. The point, however, is that real time planetary transmission will require considerably more power than for earth-orbiting or lunar communications.

The applications for space electric power systems will eventually include those of propulsion and extra-terrestrial power stations. The primary requirements for these applications are that the power system be lightweight and reliable, and be capable of generating a large amount of power for a long period of time. These requirements dictate nuclear closed-cycle systems with heat rejection by radiation. The realization of practical closed-cycle systems employing MHD generators must therefore depend on the development of nonequilibrium plasma concepts to the extent that reasonable levels of conductivity are obtained at gas temperatures commensurate with anticipated reactor technology. Because of the rather inclusive nature of the current state of knowledge concerning the feasibility of applying nonequilibrium MHD concepts, the closed-cycle MHD power system will not be discussed further in this section.

7.2 Comparison of Power Systems In the power range from 1 to 100 kw and for durations to about an hour, open-cycle MHD power systems are in direct competition with primary batteries, chemical dynamic APU's, and non-regenerative fuel cells. A realistic appraisal of MHD conversion consequently must be made relative to these competing techniques. It is appropriate, therefore, to compare these power systems beginning with a review of their general characteristics and concluding with an estimate of their performance for a specific mission.

Primary Batteries Batteries enjoy a strong competitive position because of their current wide usage and background of actual in-service experience. They are "modular" and "off-the-shelf" units and can be built up for a wide range of voltage and current requirements. Currently, battery systems are used for powers up to 2 kw and 5-30 minutes of operating time in space applications. Emergency escape capsules and ICBM auxiliary power (medium power, short time) are typical of this use. Battery systems also find application for powers up to 500 watts

at 1-5 hours of operating time (low power, medium time). Primary batteries are reliable, can be discharged at reasonably high rates, have good power/weight (up to 80 watt-hours per pound), and good power/volume ratios, and are not Carnot limited in conversion efficiency. Primary batteries, however, are expensive, have poor charged shelf-life and poor low temperature performance. The latter two objections may be minimized at the cost of increased system complexity.

Non-Regenerative Fuel Cells For operating times less than two weeks, the non-regenerative fuel cell is of interest. Fuel cells should be stable under steady loads, allow 100 per cent depth of discharge, but problem areas include electrodes (materials and design), electrolytes, removal of reaction products, and zero-g operation. Fuel cells, however, show promise of more stable operation under varying conditions of temperature than is obtainable with batteries.

Chemical Dynamic APU's Chemical auxiliary power units are especially well suited to the range of power and duration under consideration here. Solid-fueled APU's are used for short term power levels higher than can be conveniently derived from primary batteries, typically times less than 15 minutes and power levels up to about 10 kw. Solid fueled APU's do not suffer from zero-g problems, can be used to provide electrical or hydraulic power, and enjoy the advantages of solid fuel storage and handling. Their specific propellant consumption is higher than that of liquid fueled APU's and leads to excessive weight for longer, higher power operation; furthermore, since solid propellants burn at a fixed rate, the propellant grain must be sized for the peak power demand.

For high power, short time operation (to 50 kw, 2-3 hours) liquid propellant chemical APU's are well suited. These afford power control, longer duration of operation, stop/restart capability, and easier ground checkout. For longer times (to about three days) cryogenic fuel storage becomes practical; liquid hydrogen, for example, is only 1/16 as dense as hydrazine but is a factor of three better in fuel consumption per unit of energy. Liquid propellant APU's, on the other hand, are more complex than the solid fueled, encounter problems in zero-g operation and in fuel delivery to the combustion chamber.

Open-Cycle MHD Generators An open-cycle MHD generator can be run with either solid or liquid fuels; consequently, it shares the design flexibility of chemical APU's in terms of fuel selection for short or long term operation. MHD

converters, furthermore, enjoy an advantage in that no rotating hardware components are required. As will be seen, estimates indicate the MHD generators are reasonably competitive with chemical APU's, non-regenerative fuel cells, and primary batteries for powers in the range of 10-50 kw and times to about an hour.

Comparison of Power Systems A more specific comparison is in order at this point. Two cases will be considered: 1) 50 kw for one hour, and 2) 10 kw for twenty minutes. These are typical requirements of the applications previously mentioned. The weights of the power systems for these two requirements will be estimated for a non-regenerative fuel cell, a primary battery, a chemical dynamic APU, and a vortex-type MHD generator. Some discussion of the assumptions made with respect to specific power, fuel consumption, etc., is necessary and follows below. The results are summarized in Table 7-2.

The weight of a hydrogen-oxygen non-regenerative fuel cell for the two cases above will be estimated first. Based upon current TAPCO laboratory experience, it would appear that fixed weights ranging from 9 to 21 lbs/kw will be obtainable after an intensive development program of several years' duration. It will be assumed that fuel efficiency (non-critical for short durations) may be sacrificed to yield a specific fixed weight of 10 lbs/kw. An additional 150 lbs. and 50 lbs. for cases 1 and 2 respectively will be added to account for fuel, tankage, controls and some heat rejection by hydrogen purge. This results in fuel cell system weights of 650 and 150 pounds for the two cases of interest.

The primary battery is assumed to be silver-zinc, operating at 70°F. A 100 per cent depth of discharge will be assumed (total expenditure of the chemical energy stored in the battery). The available energy per unit weight varies considerably with the discharge rate; the following table lists what are considered to be conservative estimates (including case weights) of these discharge characteristics, based upon data published by battery manufacturers.

<u>Discharge Time</u> <u>(minutes)</u>	<u>Energy Release per Unit Weight</u> <u>(watt hours/lb)</u>
60	40
20	33
10	28

Battery power for the two cases defined previously would require 1250 and 100 lbs. respectively, without provisions for activation or heat rejection.

The weights of the chemical dynamic APU's are based on the assumption that the fuel will be hydrazine, thus permitting longer periods of dormancy than for cryogenic fuels. System dry weights, including tankage and controls, are estimated to be 350 lbs. and 106 lbs. for cases 1 and 2 respectively. These estimates were derived from the TAPCO developed hydrazine APU's² TU-112700 (37 kw, 260 lbs) and TU-145000 (16 kw, 170 lbs.). Fuel consumption rates³, based on expected developments in the next several years, are 5.0 and 5.1 lb/kw-hr for cases 1 and 2. Thus the total system weight estimates of these two examples are 600 lbs and 123 lbs.

The MHD system used in this comparison is assumed to be the open-cycle vortex MHD generator, the performance of which was described in Section 6.3. Two major factors contribute to the weight of such a unit, the magnet and the fuel. The former increases with power output, and the latter with both power output and time of operation. The general problem of arriving at an optimum generator design for any given set of requirements is exceedingly involved because of the large number of parameters needed to describe the machine.

The performance calculations described previously have fully accounted for significant losses and thus realistically describe generator performance under the stated conditions of operation. Since a parametric analysis was not completed, the results must be considered as conservative; an optimum design was not determined. Hence the potential system weights will be less than 1380 lb and 205 lb respectively for cases 1 and 2 above, assuming permanent magnets, and less than 750 lb and 60 lb respectively, assuming superconducting magnets and a three month dormancy.

These results, must not be regarded as the best representative values since the design flexibility of the vortex generator permits control and variation of such a large number of parameters that the surpassing of these performance figures should be possible. The purpose of the comparison was, in essence, to give some idea of the relative status of open-cycle MHD power conversion.

The two missions selected resulted in a situation in which both the generator magnet and the fuel substantially contributed to the total weight. This need not be true in general; there are missions such that one or the other will predominate and the other may be "neglected". For very long durations of power, for example, the fuel weight might predominate and the generator weight could be neglected; in such a case the conversion efficiency would be all-important since it would determine the efficiency of fuel utilization and the total fuel weight required. In this case high efficiency of generator operation would be preferable to a light-weight converter operating at an efficiency penalty. For shorter times (fuel weight negligible), operation at reduced efficiency in favor of increased generator power output per unit (system) weight would be preferred.

A comparison of the results obtained is indicated in Table 7-2.

Table 7-2
Estimated Total Weight of Various Power Systems

	<u>Case 1</u> 50 kw for 60 min.	<u>Case 2</u> 10 kw for 20 min.
Fuel Cell (Non-Regenerative)	650 lbs	150 lbs
Primary Battery (Silver-Zinc)	1250	100
Chemical Dynamic APU (Liquid Fueled)	600	123
Vortex MHD Generator (Liquid Fueled)		
a) Permanent Magnet	< 1380	< 205
b) Superconducting Magnet (3 Mo. Dormancy)	< 750	< 60

8.0 CONCLUSIONS AND RECOMMENDATIONS

Conclusions The objective of the present experimental and theoretical research has been to determine the performance characteristics of the vortex MHD power generator and the applicability of this device in the field of electric power generation for space application.

Emphasis was given to advancing the concepts of turbulent vortex flows, to determining the operating characteristics of an experimental vortex MHD generator, and to improving the analytical methods for predicting generator performance.

The investigation of turbulent vortex flow was conducted both analytically and experimentally. Analytical models, based on a pseudo-laminar analysis and in analogy with turbulent layers, were developed for the hydrodynamics of turbulent jet-driven vortex flows with and without centerbodies. The mixing length theory which was developed for this application under a preceding contract was found to be more complicated and unnecessary. Measurements of the flow distributions within a vortex chamber generally confirmed the validity of the analytical one-dimensional flow models for the vortex cover region; they also revealed the presence of relatively strong radial flows in the sidewall boundary layers of the low aspect ratio vortex chamber employed. It would appear that this boundary layer flow will be the dominant factor in establishing the lower limit of practical power production by the vortex MHD generator. This lower limit is judged to be approximately 10 KW.

A vortex type MHD generator was operated in the laboratory on seeded arc-heated argon plasmas. Both single and dual driving jets were employed; the seed material consisted of either an aqueous solution of cesium hydroxide or liquid cesium metal. Of the several test attempts, two were aborted because of commercial equipment failures and two were unsuccessful in producing substantial power because of rapid graphite exhaust tube erosion and subsequent generator shorting. The materials problem otherwise was reduced to an acceptable level. Heat transfer and thermal control were established consistent with original estimates.

A computer numerical simulation of the vortex MHD generator was developed for parametric analysis and performance determinations. Real gas effects, including

external heat transfer and viscous drag on the vortex sidewalls were thereby included in the calculation of overall generator performance.

Finally, the computer analysis was applied to the example of a high temperature combustion-plasma-operated vortex MHD generator; the generator performance was shown to be very attractive when compared with other types of prominent open-cycle power conversion systems. Furthermore, an analysis of reliability and materials wear out time indicated that this generator would be entirely satisfactory for operating times of at least one hour, which an applications survey suggested would encompass most of the space requirements for open-cycle power.

In summary, a survey of space power requirements has shown that a definite need exists for short term power at moderate to high power levels. This power generation must be accomplished at high power density and at very high reliability. The results of the present study have established that the combustion driven vortex MHD generator is uniquely suited for such application. The direction of this investigation has emphasized the technology of open-cycle power systems rather than closed-cycle systems because of the belief that the former will be brought to fruition at a much earlier date. There is no intention of minimizing the possibility for the potential application of the vortex concept to closed-cycle MHD power systems. In conclusion, the recommendations for a proposed program which logically will advance still further the vortex generator concept are elucidated below.

Recommendations The computer program developed under the present program should be employed in a more extensive parametric analysis to determine optimum generator operating conditions and geometrical configurations.

The analytical and experimental study of turbulent vortex motion should be continued, with emphasis on the sidewall boundary layer development and interaction with the main vortex core flow.

Additional tests of the experimental vortex MHD generator, designed and constructed during the present program for operation with cesium seeded argon plasmas, are warranted in order to: confirm the empirical coefficients employed in the computer program; prove the high temperature performance of new ceramic materials which are being developed continually; and demonstrate the adequacy of certain generator construction techniques.

9.0 APPENDIX A

The Differential Equations of Vortex Flow

Laminar Flow In cylindrical coordinates the Navier-Stokes equations are, assuming steady, symmetric incompressible, constant viscosity flow (with $\mu' = 0$ and $\lambda = -2/3\mu$),

$$u \frac{\partial u}{\partial r} + \frac{v}{r} \frac{\partial u}{\partial \theta} + w \frac{\partial u}{\partial z} - \frac{v^2}{r} = -\frac{1}{\rho} \frac{\partial p}{\partial r} + \nu \left[\nabla^2 u - \frac{u}{r^2} - \frac{2}{r^2} \frac{\partial v}{\partial \theta} \right] \quad (1)$$

$$u \frac{\partial v}{\partial r} + \frac{v}{r} \frac{\partial v}{\partial \theta} + w \frac{\partial v}{\partial z} + \frac{uv}{r} = -\frac{1}{\rho r} \frac{\partial p}{\partial \theta} + \nu \left[\nabla^2 v - \frac{v}{r^2} + \frac{2}{r^2} \frac{\partial u}{\partial \theta} \right] \quad (2)$$

$$u \frac{\partial w}{\partial r} + \frac{v}{r} \frac{\partial w}{\partial \theta} + w \frac{\partial w}{\partial z} = -\frac{1}{\rho} \frac{\partial p}{\partial z} + \nu \nabla^2 w \quad (3)$$

where

$$\nabla^2 = \frac{\partial^2}{\partial r^2} + \frac{1}{r} \frac{\partial}{\partial r} + \frac{1}{2} \frac{\partial^2}{\partial \theta^2} + \frac{\partial^2}{\partial z^2}$$

and

(u, v, w) = velocity components in the (r, θ , z) right handed cylindrical coordinate system

p = pressure

ρ = density

ν = kinematic viscosity

The equation expressing conservation of flow is

$$u_r + u/r + 1/r v_\theta + w_z = 0 \quad (4)$$

Now for a vortex chamber having a large number of driving jets $\partial/\partial\theta \approx 0$ except near a driving jet nozzle. Furthermore, for a chamber with an inner porous cylinder $w \approx 0$ and $\partial/\partial z \approx 0$. (This holds also for the regions which are not too close to the exit tube of a chamber having no inner cylinder.) If these terms in the basic equations are neglected, there results

$$u \frac{du}{dr} - \frac{v^2}{r} = -\frac{1}{\rho} \frac{dp}{dr} + \nu \left(\frac{d^2 u}{dr^2} + \frac{1}{r} \frac{du}{dr} - \frac{u}{r^2} \right) \quad (5)$$

$$u \frac{dv}{dr} + \frac{uv}{r} = \gamma \left(\frac{d^2v}{dr^2} + \frac{1}{r} \frac{dv}{dr} - \frac{v}{r^2} \right) \quad (6)$$

$$\frac{du}{dr} + \frac{u}{r} = 0 \quad (7)$$

This system, which is integrable, should represent the "core" region of a vortex chamber. From (7) there follows

$$\frac{du}{u} = - \frac{dr}{r} \Rightarrow ur = u_o r_o = \text{const.} \quad (8)$$

where the subscript refers to the outermost part of the core region. It will be assumed that the recovered driving jet velocity, v_o , is obtained at $r = r_o$.

Using (8) in (5) and (6) there is obtained

$$\frac{u^2 + v^2}{r} = \frac{1}{\rho} \frac{dp}{dr} \quad (9)$$

and

$$\frac{u_o r_o}{r} \left(\frac{dv}{dr} + \frac{v}{r} \right) = \gamma \frac{d}{dr} \left(\frac{dv}{dr} + \frac{v}{r} \right) \quad (10)$$

The general solution of (10) is

$$v = Ar^{-1} + Br^{1 + Re_u} \quad (11)$$

where

$$Re_u = \frac{u_o r_o}{\gamma}$$

is the negative of a radial Reynolds number (recall that we are considering a central exit tube with $u < 0$).

The solution (11) holds for laminar flow and the coefficients A and B are to be determined by the boundary conditions

$$v = v_o \text{ at } r = r_o$$

$$v = v_i \text{ at } r = r_i$$

For the case with an inner porous cylinder r_i is the radius of the cylinder and $v_i = 0$. When there is no porous cylinder r_i is the radius at which (11) must be matched to an inner solution which represents the flow in the exit tube region.

Turbulent Flow The equations governing the mean flow quantities of a turbulent flow are obtained from the basic equations for non-steady flow by assuming that each flow quantity is the sum of a time independent mean and a time dependent turbulent quantity. Thus

$$u = \bar{u}(R) + u'(r,t), \quad v = \bar{v}(r) + v'(r,t)$$

and

$$p = \bar{p}(r) + p'(r,t)$$

Using these in (5)-(7) and averaging, there is obtained

$$\bar{u} \frac{d\bar{u}}{dr} - \frac{\bar{v}^2}{r} = -\frac{1}{\rho} \frac{d\bar{p}}{dr} - \overline{u' \frac{du'}{dr}} + \frac{\overline{v'^2}}{r} \quad (12)$$

$$\bar{u} \left(\frac{d\bar{v}}{dr} + \frac{\bar{v}}{r} \right) = \nu \frac{d}{dr} \left(\frac{d\bar{v}}{dr} + \frac{\bar{v}}{r} \right) - \overline{u' \frac{dv'}{dr} + \frac{v'}{r}} \quad (13)$$

$$\frac{d\bar{u}}{dr} + \frac{\bar{u}}{r} = 0 \quad (14)$$

According to (14), the solution (8) for the radial velocity component also holds for the mean value \bar{u} of a turbulent vortex flow. Equation (12) can be written in a form analogous to (9) by noting that

$$\overline{\frac{du'}{dr} + \frac{u'}{r}} = \frac{d\bar{u}}{dr} + \frac{\bar{u}}{r} = 0$$

Using this and (14) in (12) gives

$$\frac{1}{\rho} \frac{d\bar{p}}{dr} = \frac{1}{r} (\bar{u}^2 + \bar{v}^2 + \overline{u'^2} + \overline{v'^2}) \quad (15)$$

as the equation which determines the mean pressure distribution for turbulent, axi-symmetrical vortex flow. Now the equation for the tangential velocity \bar{v} can be written in the form of (10) if the turbulence stress terms

$$-\overline{\rho u' \left(\frac{dv'}{dr} + \frac{v'}{r} \right)} = \frac{d\sigma'_{r\theta}}{dr} + \frac{2}{r} \sigma'_{r\theta}$$

are interpreted in terms of an eddy viscosity and the mean flow as

$$\sigma'_{r\theta} = E \left(\frac{d\bar{v}}{dr} - \frac{\bar{v}}{r} \right) \quad (16)$$

Then, for constant E,

$$\frac{d\sigma'_{r\theta}}{dr} + \frac{2}{r} \sigma'_{r\theta} = E \frac{d}{dr} \left(\frac{d\bar{v}}{dr} + \frac{\bar{v}}{r} \right) \quad (16A)$$

Using this in (13) results in

$$\frac{\bar{u}_o r_o}{r} \left(\frac{d\bar{v}}{dr} + \frac{\bar{v}}{r} \right) = (\nu' + E/\rho) \frac{d}{dr} \left(\frac{d\bar{v}}{dr} + \frac{\bar{v}}{r} \right) \quad (17)$$

The case $E = \text{constant}$ has the solution (11) if ν' is replaced by $\nu' + E/\rho$; this assumption will be made as a starting point in the analysis of turbulent vortex chamber data. There is a justification of the constant eddy viscosity assumption since a fully turbulent flow ($E \gg \mu$) has a nearly constant eddy size. The region of a vortex chamber where fully turbulent flow is obtained can be expected to be the core region between the driving jets and the inner cylinder (or the inner viscous region for the case of a vortex chamber with no inner cylinder). This core region of a vortex chamber is analogous to the outer region of a turbulent boundary layer and to the mixing region in the turbulent mixing of parallel jets. Both of these phenomena have been shown to be governed by the equations of free turbulence with a constant eddy viscosity (References 3 and 8).

APPENDIX B

Integration of the Torque Balance Relation for the Wall Region

Conservation of angular momentum dictates that (see Equation (24) of Section 2.1.4)

$$\frac{dV}{dR} - \frac{V}{A + R} - \frac{Re_u}{1 + E/\mu} \frac{V}{A + R} = \frac{C}{(1 + E/\mu)(A + R)} \quad (1)$$

where

$$C = \frac{R_i^2 C_{f_i} Re_v}{2(1 - R_i)} \quad (2)$$

Equation (1) can be rewritten as

$$(A + \underline{R}) \frac{d}{d\underline{R}} \left(\frac{v}{A + \underline{R}} \right) - \frac{Re_u}{1 + E/\mu} \frac{v}{A + \underline{R}} = \frac{C}{(1 + E/\mu)(A + \underline{R})} \quad (3)$$

For a linear variation of E/μ this equation can be integrated. Letting $1 + E/\mu = a + b\underline{R}$, it can be written as

$$\frac{d}{d\underline{R}} \left\{ \frac{(A + \underline{R})^{N-1}}{(a + b\underline{R})^N} v \right\} = C (a + b\underline{R})^{-(1+N)} (A + \underline{R})^{-(3-N)} \quad (4)$$

where

$$N = \frac{Re_u}{Ab - a} < 0 \quad (5)$$

It follows that

$$(A + \underline{R})^{N-1} (a + b\underline{R})^{-N} v = C I_N(\underline{R}) + B \quad (6)$$

where B is an integration constant and

$$I_N(\underline{R}) = \int^{\underline{R}} (a + bx)^{-(1+N)} (A + x)^{-(3-N)} dx \quad (7)$$

The integration required to evaluate $I_N(\underline{R})$ can be performed for any value of N. Let

$$A + x = \frac{a - Ab}{\eta - b}$$

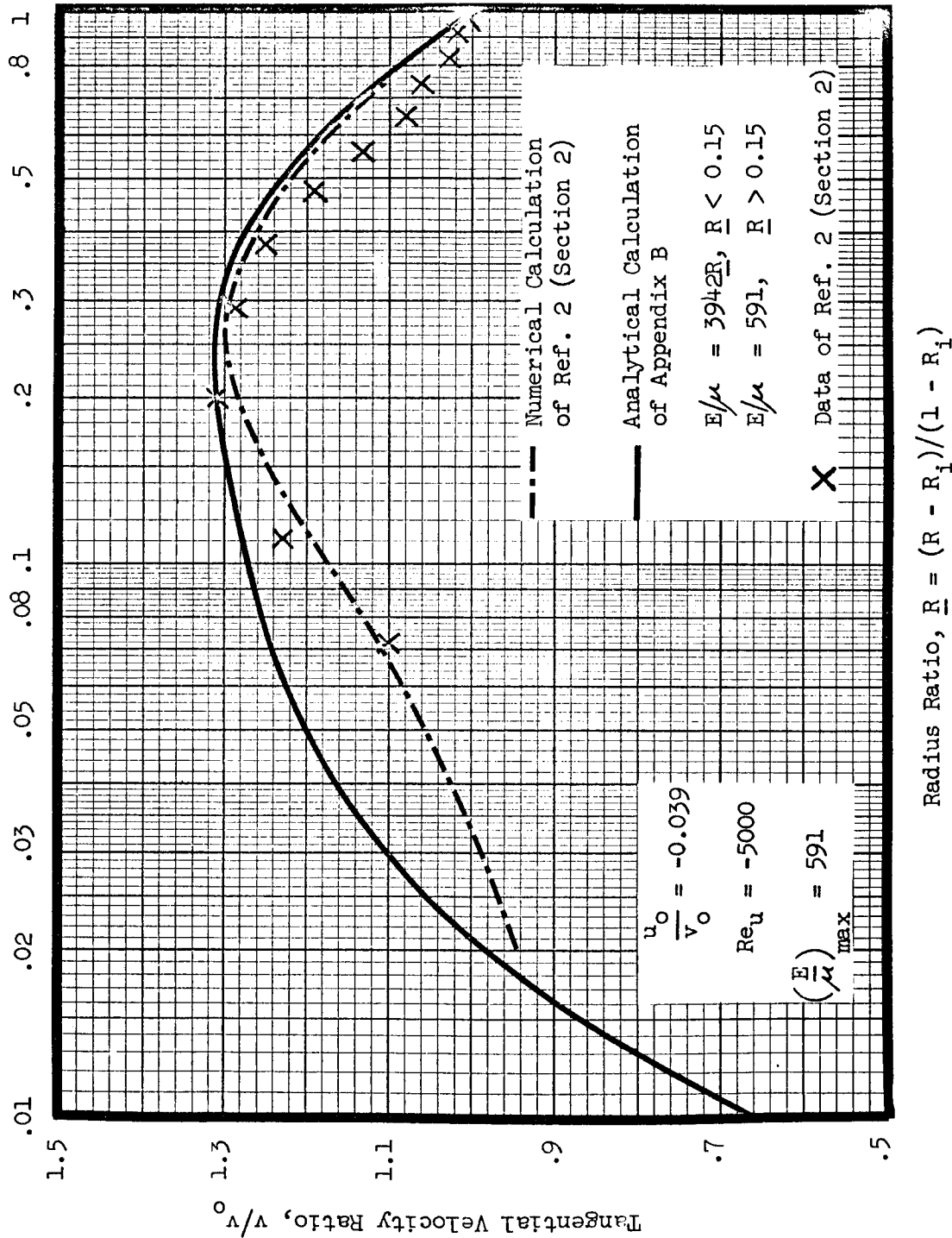
There results

$$I_N(\underline{R}) = (Ab - a)^{-3} \int^{\frac{a + b\underline{R}}{A + \underline{R}}} \eta^{-(1+N)} (\eta - b)^2 d\eta \quad (8)$$

or

$$I_N(\underline{R}) = (Ab - a)^{-3} \left\{ \eta^{-N} \left[\frac{\eta^2}{2 - N} - \frac{2b\eta}{1 - N} - \frac{b^2}{N} \right] \right\}_{\eta = \frac{a + b\underline{R}}{A + \underline{R}}} \quad (9)$$

An example of the solution for the wall region as obtained in this Appendix is given in Figure B-1. It has been matched to the outer profile at $\underline{R}_m = 0.15$ and it is compared with a profile which was obtained by numerical integration in Reference 2 of Section 2.



Calculated Wall Velocity Region Profiles Figure B-1

It should be noted that the solution given by (6) and (9) can be employed in the immediate neighborhood of the inner cylinder; if it is, and if the constant B is evaluated so that $V = 0$ at $\underline{R} = 0$, then the solution given by Equation (28) of Section 2.1.4 is the result. But the solution of Section 2.1.4 is expected to be valid only for $\underline{R} = O(10^{-4})$ or less. For larger values of \underline{R} the solution given in this Appendix should be used.

APPENDIX C

Equations for Flow in a Vortex without Porous Inner Cylinder (Centerbody)

Steady, Symmetric, Incompressible, Constant Viscosity Flow in Annular Region

The assumptions are:

$$\begin{aligned}\mu &= \text{constant} & \frac{\partial}{\partial t} &= 0 \\ \mu' &= 0 & \frac{\partial}{\partial \theta} &= 0 \\ \lambda &= -2/3 & \frac{\partial}{\partial z} &= 0 \\ \rho &= \text{constant} & w &= 0\end{aligned}$$

The general solution of the tangential momentum equation, derived from the Navier-Stokes equations, is

$$v = Ar^{-1} + Br^1 + Re_v \quad (1)$$

as indicated by Equation (11) of Appendix A. Nondimensionalizing and changing constants,

$$V = v/v_o \quad r = r/r_o$$

Equation (1) becomes

$$V = AR^{-1} + BR^1 + Re_v \quad (2)$$

The boundary conditions are:

$$r = r_o : R = 1; v = v_o; V = 1$$

$$r = r_i : R_i = r_i/r_o; v = v_i; V_i = v_i/v_o$$

Thus

$$B = \frac{R_1 V_1 - 1}{R_1^{2+Re_v} - 1}$$

$$A = \frac{R_1^{2+Re_u} - R_1 V_1}{R_1^{2+Re_u} - 1}$$

and the solution (2) becomes

$$V = \left[\frac{R_1 V_1 - R_1^{2+Re_u}}{1 - R_1^{2+Re_u}} \right] \left[\frac{1 - R^{2+Re_u}}{R} \right] + \frac{R^{2+Re_u}}{R} \quad (3)$$

which agrees with the solution of Einstein and Li (Reference 9 of Section 2). For purposes of eventually matching the solutions for the annular region and the inner region, the radial derivation of V at the inner radius is required. It is

$$\left. \frac{dV}{dR} \right|_{R=R_1} = \left[\frac{1 - R_1 V_1}{1 - R_1^{2+Re_u}} \right] (1 + Re_u) R_1^{Re_u} - \left[\frac{R_1 V_1 - R_1^{2+Re_u}}{1 - R_1^{2+Re_u}} \right] \frac{1}{R_1^2} \quad (4)$$

Steady, Symmetric, Incompressible, Constant Viscosity Flow in Inner Region

The assumptions are the same as for the annular region except that $\partial w / \partial z =$ constant over the exit tube area. This latter assumption was successfully employed by Einstein and Li and later by Deissler and Perlmutter. (References 9 and 10 respectively of Section 2). For this case the Navier-Stokes equations reduce to

$$v = Cr^{-1} + Dr^{-1} e^{(Re_u/2)(r/r_1)^2} \quad (5)$$

or in the nondimensional form

$$V = CR^{-1} + DR^{-1} e^{(Re_u/2)(R/R_1)^2} \quad (6)$$

where

$$-C = D = \frac{R_1 V_1}{e^{Re_u/2} - 1}$$

when the following boundary conditions are imposed

$$r = r_1: R_1 = r_1/r_0; v = v_1; V_1 = v_1/v_0$$

$$r = 0: R = 0; v = 0; V = 0$$

Thus the solution (6) can be expressed as

$$V = \frac{R_1 V_1}{R} \frac{1 - e^{-(Re_u/2)(R/R_1)^2}}{1 - e^{-Re_u/2}} \quad (7)$$

and thus its derivative at R_1 is

$$\left. \frac{dV}{dR} \right|_{R=R_1} = -\frac{V_1}{R_1} + \frac{V_1}{R_1} Re_u \frac{e^{-Re_u/2}}{e^{-Re_u/2} - 1} \quad (8)$$

Matched Solutions for the Inner and Annular Vortex Regions Setting

$\left. \frac{dV}{dR} \right|_{R=R_1}$ from the two regions equal, and solving for V_1 ,

$$V_1 = \frac{(2 + Re_u)(e^{Re_u/2} - 1)}{Re_u \left\{ (R_1)^{-2-Re_u} e^{Re_u/2} - 1 \right\} + 2(e^{Re_u/2} - 1)} \quad (9)$$

Thus in the inner region, where $R_1 > R$

$$VR = \frac{(2 + Re_u)(e^{(Re_u/2)(R/R_1)^2} - 1)}{Re_u \left\{ (R_1)^{-2-Re_u} e^{Re_u/2} - 1 \right\} + 2(e^{Re_u/2} - 1)} \quad (10)$$

and in the annular region, where $1 > R > R_1$

$$VR = \frac{Re_u + 2(1 - e^{Re_u/2}) R^{2+Re_u} - 1}{Re_u (R_1^{-2-Re_u} e^{Re_u/2} - 1) + 2(e^{Re_u/2} - 1)} + R^{2+Re_u} \quad (11)$$

Steady, Symmetric, Compressible, Constant Viscosity Flow in Annular Region
 With the assumption of constant density relaxed, but all other restrictions maintained as for the incompressible case, the tangential momentum equation is decoupled and identical to that for the incompressible case

$$\frac{\rho_o^r u_o}{r} \left(\frac{dv}{dr} + \frac{v}{r} \right) = \mu \frac{d}{dr} \left(\frac{dv}{dr} + \frac{v}{r} \right) \quad (12)$$

Steady, Symmetric, Compressible, Constant Viscosity Flow in Inner Region
 If the assumptions for compressible flow in the inner region remain the same as for incompressible flow except that now $d\rho w/dz = \text{constant}$ over the exit tube area (this latter assumption was first suggested by Deissler and Perlmutter, Reference 10, Section 2) the tangential momentum equation becomes

$$r^2 \frac{d^2 v}{dr^2} + r \left(1 - Re_u \frac{r^2}{r_1^2} \right) \frac{dv}{dr} - \left(1 + Re_u \frac{r^2}{r_1^2} \right) v = 0 \quad (13)$$

Thus in this case also the tangential momentum equations are identical for both compressible and incompressible flow.

10.0 REFERENCES

Section 2

1. Rosenzweig, M. L., "Velocity Recovery and Shear Reduction in Jet Driven Vortex Tubes", Aerospace Corp. Report No. TDR-594(1203-01)TN-1, March 1962.
2. Williamson, G. G. and McCune, J. E., "A Preliminary Study of the Structure of Turbulent Vortices", ARAP Report No. 32, July 1961.
3. Clauser, F. H., "The Turbulent Boundary Layer", Advances in Applied Mechanics, Ed. by H. L. Dryden and T. H. von Karman, Academic Press, 1956, p. 2.
4. Ragsdale, R. C., "Applicability of Mixing Length Theory to a Turbulent Vortex System", NASA TN D-1051, August 1961.
5. Keyes, J. J., "An Experimental Study of Gas Dynamics in High Velocity Vortex Flow", Proc. 1960 Heat Transfer and Fluid Mechanics Institute, Stanford University, p. 31.
6. Davis, W. C., et al, "Research on the Vortex MHD Power Generator, Second Quarterly Progress Report", TRW No. ER-5084, October 1962.
7. Davis, W. C., et al, "Research on the Vortex MHD Power Generator, First Quarterly Progress Report", TRW No. ER-4949, July 1962.
8. Schlichting, H., Boundary Layer Theory, McGraw-Hill, New York, Fourth Ed. 1960, p. 598.
9. Einstein, H. A. and Li. H., "Steady Vortex Flow in a Real Fluid", Proc. Heat Trans. and Fluid Mech. Institute, 1951.
10. Deissler, R. G. and Perlmutter, M., "Analysis of the Flow and Energy Separation in a Turbulent Vortex", Int. J. Heat Mass Transfer, Vol. 1, pp. 173-191, 1960.
11. Kendall, J. M., Jr., "Experimental Study of a Compressible Viscous Vortex", JPL Tech. Report No. 32-290, June 1962.
12. Knoernschild, E. M., et al, "Vortex Magnetohydrodynamic Generator Design Study", ASD Tech. Report No. 61-380, November 1961, p. 62.
13. Pfleiderer, C., Die Kreiselpumpen, Springer Verlag, Berlin, Germany, 1932.
14. Mack, L. M., "The Laminar Boundary Layer on a Disk of Finite Radius in a Rotating Flow. Part I", JPL Tech. Report No. 32-224, May 1962.
15. Gregory, N., et al, "On the Stability of Three-Dimensional Boundary Layers with Application to the Flow Due to a Rotating Disk", Phil. Trans. Roy. Soc., A 248, 1955, p. 155-199.

Section 3

1. Shure, L. I., "Heat Transfer Test Capsule Design Report", TRW No. ER-4559, September 1961.
2. Hermans, J. J., Flow Properties of Disperse Systems, Interscience Publishers, New York, New York, 1953.
3. Emmons, H. W., (editor), Fundamentals of Gas Dynamics, Princeton University Press, 1958, p. 256.
4. Rosenzweig, M. L., "Velocity Recovery and Shear Reduction in Jet Driven Vortex Tubes", Aerospace Corp. Report No. TDR-594(1203-01)TN-1, March 1961.
5. Ostrach, S., "Estimate of Vortex Generator End-Plate Heat Transfer and Boundary-Layer Blockage Effects, TRW No. ER-4426, May 1961.
6. Harned, B. W., et al, "XM-731 Plasma Engine", WADD Tech. Report No. 60-895, Appendix I, January 1961.
7. Williamson, G. G. and McCune, J. E., "A Preliminary Study of the Structure of Turbulent Vortices", ARAP Report No. 32, July 1961.
8. Kerrebrock, J. L., "Conduction of Gases with Elevated Electron Temperatures", Engineering Aspects of Magnetohydrodynamics, Columbia University Press, New York, 1962, pp. 327-346.
9. Foëx, M., "Electrical Conductivity of BeO and MgO at Elevated Temperatures", Compt. Rendu 214, 1942, p. 665.
10. Campbell, I. E., (editor), High Temperature Technology, John Wiley and Sons, New York, 1957, pp. 467-475.
11. Timoshenko, S. and Goodier, J. N., Theory of Elasticity, Second Ed. McGraw-Hill, 1951, p. 407.
12. Zirconium Corp. of America, "Technical Data Sheet No. 10", October 1960.
13. "Research and Development on a Vortex MHD Power Generator", Final Report NASA Contract NAS5-703, TRW No. ER-4737, December 1961, p. 27.
14. Taylor, J. B. and Langmuir, I., "The Evaporation of Atoms, Ions, and Electrons from Cesium Films on Tungsten", Phys. Rev., 44, 1933.
15. Hurwitz, H., et al, "Electron Heating in Magnetohydrodynamic Power Generators", ARS J., Vol. 32, No. 6, August 1962, p. 1237.
16. Rosa, R. J., "Nonequilibrium Ionization in MHD Generators", Proc. of IEEE, May 1963, p. 774.

Section 4

1. Earles, D. R., "Reliability Application and Analysis Guide", The Martin Co., MI-60-54 (Rev. 1), July 1961.
2. Romaine, O., "Why Explosive Devices?", Space/Aeronautics, 39, No. 3, March 1963, p. 96.
3. TRW Internal Data (Dynasoar APU Combustor).
4. Davis, W. C., "Research on the Vortex MHD Power Generator", Third Quarterly Progress Report, TRW No. ER-5212, January 1963.
5. Barth, V. C., "Physical and Mechanical Properties of Tungsten and Tungsten-Base Alloys", Battelle Memorial Institute, DMIC Report No. 127, OTS PB 151084, March 16, 1960.
6. Eckert, E. R. G., "Introduction to the Transfer of Heat and Mass", McGraw-Hill Book Co., New York, 1950, pp. 249-257.
7. Hord, Richard A. and Pennington, J. Byron, "Temperature and Composition of a Plasma Obtained by Seeding a Cyanogen-Oxygen Flame with Cesium", NASA TN D-380, May 1960.
8. Kohl, Walter H., "Materials and Techniques for Electron Tubes", Reinhold Publishing Corporation, New York, N. Y., 1960, p. 263.
9. Hepworth, M. A. and Arthur, G., "Ceramic Materials for MPD Power Generation", presented at Symposium on Magnetoplasmadynamic Electrical Power Generation, King's College, University of Durham, Newcastle Upon Tyne, September 1962.
10. Sutton, George O., "Rocket Propulsion Elements", John Wiley and Sons, Inc., New York, 1956, Chapter 4.
11. Batchelor, James D., et al, "Gas-Metal Reactions in Rocket Nozzles", Atlantic Research Corp., ASD-TDR-62-327 Pt. I, June 1962.
12. Fassel, W. M., Jr., et al, "Behavior of Rocket Nozzle Materials at High Temperatures and Pressures of Combustion Product Gas Mixtures", Second Quarterly Technical Report, Ford Motor Co., U-1945, ASTIA AD 292096, 15 December 1962, p. 25.
13. Kubaschewski, O. and Hopkins, B. E., "Oxidation of Metals and Alloys", Academic Press Inc., New York, 1953, pp. 16-19.
14. "Research and Development on a Vortex MHD Power Generator", Final Report, TRW No. ER-4737, December 1961, pp. 108-110.

Section 5

1. Rosa, R. J., "Magnetohydrodynamic Generators and Nuclear Propulsion", ARS J., August 1962, p. 1221.
2. Indiana Steel Products Division, Indiana General Corp., "Design and Application of Permanent Magnets", Permanent Magnet Manual, No. 6A.
3. Roters, H. C., Electromagnetic Devices, John Wiley and Sons, Inc., New York, 1941, pp. 130-134.
4. Callaghan, E. E. and Maslen, S. H., "The Magnetic Field of a Finite Solenoid", NASA TN D-465, October 1960.
5. Kunzler, J. E. and Tanenbaum, M., "Superconducting Magnets", Sci. Amer., June 1962, p. 60.

Section 6

1. Sherman, A., et al, "Study of Electrical Energy Conversion Systems", ASD-TR-61-704, February 1962, p. 96.
2. Hord, R. A. and Pennington, J. B., "Temperature and Composition of a Plasma Obtained by Seeding a Cyanogen-Oxygen Flame with Cesium", NASA TN D-380, May 1960.
3. Dibelius, N. R. and Luebke, E. A., "Electrical Conductivity of Flame Gases Seeded with Alkali Metals and Application to MHD Power Plant Design", Second Symposium on MHD, Univ. of Penna., March 1961.
4. Brode, R. B., Rev. Mod. Phys. 5, 1933.
5. Keyes, J. J., Jr., "Experimental Study of Flow and Separation in Vortex Tubes with Application to Gaseous Fission Heating", ARS J., Vol. 31, No. 9, September 1961, p. 1207.
6. Mack, L. M., "The Laminar Boundary Layer on a Disk of Finite Radius in a Rotating Flow - Part I", JPL Tech. Report No. 32-224, May 1962.
7. Sherman, A., "Calculation of Electrical Conductivity of Ionized Gases", ARS J., June 1960, p. 559.
8. Barriere, M., et al, Rocket Propulsion, Elsevier Pub. Co., 1960, p. 424.
9. Knoernschild, E. M., "Vortex Magnetohydrodynamic Generator Design Study", ASD Tech. Report No. 61-380, November 1961, p. 54.
10. Ostrach, S., "Estimate of Vortex Generator End-Plate Heat Transfer and Boundary-Layer Blockage Effects", TRW No. ER-4426, May 1961.
11. Zirconium Corp. of America, data.

Section 7

1. Welles, O. W., "Space Probe Limitations on Nuclear-Electric Power Supplies", ARS preprint 2527-62, 1962.
2. Aerospace Management Magazine, "Trends in Auxiliary Power", August 1961, p. 50.
3. Orsini, A., "Spacecraft Power from Open-Cycle Chemical Turbines", Astronautics Magazine, December 1959.